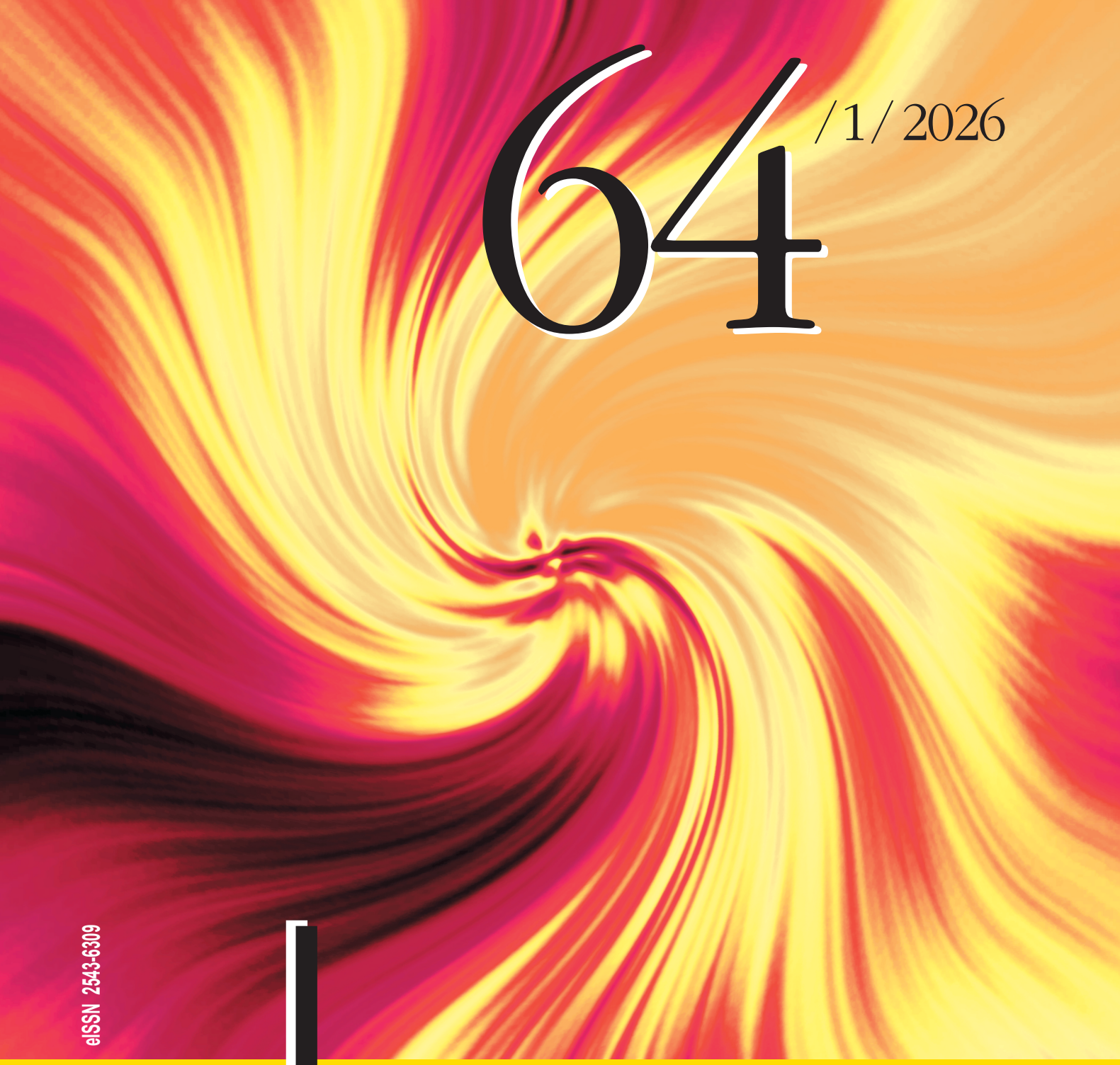

64 /1/ 2026

JOURNAL OF THEORETICAL AND APPLIED MECHANICS

WARSAW 2026, QUARTERLY, VOLUME 64, ISSN 1429-2955 eISSN 2543-6309

POLISH SOCIETY OF THEORETICAL AND APPLIED MECHANICS ptmts

POLISH SOCIETY OF THEORETICAL AND APPLIED MECHANICS

JOURNAL OF THEORETICAL AND APPLIED MECHANICS

Vol. 64 • No. 1

Quarterly

WARSAW 2026

JOURNAL OF THEORETICAL AND APPLIED MECHANICS
(until 1997 Mechanika Teoretyczna i Stosowana, ISSN 0079-3701)

Beginning with Vol. 45, No. 1, 2007, *Journal of Theoretical and Applied Mechanics* (JTAM) has been selected for coverage in Thomson Reuters products and custom information services. Now it is indexed and abstracted in the following:

- **Science Citation Index Expanded** (also known as SciSearch®)
- **Journal Citation Reports/Science Edition**

Advisory Board

Michał Kleiber – Chairman
Jorge A.C. Ambrosió, Romesh C. Batra,
Alain Combescure, Jüri Engelbrecht, Józef Kubik,
Włodzimierz Kurnik, Zenon Mróz, Wiesław Nagórko,
Ryszard Parkitny, Ekkehard Ramm, Meir Shillor,
Andrzej Styczek, Eugeniusz Świtoński, Hisaaki Tobushi,
Andrzej Tylikowski, Dieter Weichert, Jose E. Wesfreid,
Joseph Zarka, Vladimir Zeman

Editorial Board

Piotr Kowalczyk – Editor-in-Chief
Section Editors: Krzysztof Dems, Grzegorz Dziatkiewicz,
Witold Elsner, Eric Florentin, Elżbieta Jarzębowska,
Oleksandr Jewtuszenko, Zbigniew Kowalewski, Tomasz Krzyżyński,
Sławomir Kubacki, Anna Kucaba-Piętal, Tomasz Łodygowski,
Kinga Nalepka, Michał Nowak, Jacek Szumbarski,
Krzysztof Tajduś, Agnieszka Tomaszewska, Utz von Wagner,
Jerzy Warmiński

Language Editors – Waldemar Korczyk, Daria Wieliczko
Technical Editor – Katarzyna Jezierska
Managing Editor – Urszula Kowalczyk

Editorial Office

Al. Armii Ludowej 16, room 650; 00-637 Warsaw, Poland
e-mail: jtam@ptmts.org.pl
www.jtam.pl

Articles in JTAM are published under Creative Commons Attribution 4.0 International. Unported License https://creativecommons.org/licenses/by/4.0/deed.en. By submitting an article for publication, the authors consent to the grant of the said license.

The journal content is indexed in Similarity Check, the Crossref initiative to prevent plagiarism.

Ministry of Science and Higher Education
Republic of Poland

This issue has been published with financial support from the Polish Ministry of Science and Higher Education under the Excellent Science II programme "Support for scientific conferences".

JOURNAL OF THEORETICAL
AND APPLIED MECHANICS
64, 1, pp. 3–13, Warsaw 2026
https://doi.org/10.15632/jtam-pl/214041

INFLUENCE OF AIR VENT GEOMETRY IN BRAKE ROTORS ON THE PERFORMANCE OF A CAR BRAKING SYSTEM

Mateusz KITA*, Jarosław KACZMARCZYK, Sławomir DUDA

Department of Theoretical and Applied Mechanics, Silesian University of Technology, Gliwice, Poland
*corresponding author, *Mkita@polsl.pl*

The growing mass of modern vehicles increases kinetic energy and thermal stress on braking systems, elevating rotor temperatures and the risk of brake fade. In ventilated disc brakes, heat dissipation depends strongly on the geometry of internal vents. This study uses finite element method (FEM) simulations to examine the thermal behaviour of passenger-car ventilated rotors with different vent designs, including motorsport-inspired configurations, under high thermal loading. While previous studies have examined heat generation and dissipation in disc brakes, direct comparative FE analyses of vent geometries remain limited. The results demonstrate that vent shape significantly affects cooling performance during and following intense braking.

Keywords: finite element method; heat dissipation; brakes; friction coefficient.

Articles in JTAM are published under Creative Commons Attribution 4.0 International.
Unported License https://creativecommons.org/licenses/by/4.0/deed.en.
By submitting an article for publication, the authors consent to the grant of the said license.

1. Introduction

Brakes are essential vehicle components, enabling safe deceleration and speed control. Increasing vehicle mass and performance have driven continuous development of braking technology. Braking systems are commonly classified as stopping, holding, or retarding brakes, reflecting their functions. Early progress included the drum brake, introduced by Renault in 1902, and the disc brake concept proposed by Frederick William Lanchester in the same year; subsequent advances led to assistive technologies such as anti-lock braking systems (ABS), electronic brake-force distribution (EBD), and ultra-high-performance (UHP) tyres. The proliferation of electric vehicles has introduced regenerative braking; however, conventional friction-based systems remain critical for emergency braking, particularly in heavy vehicles (Nadig *et al.*, 2017; Cristescu & Ilie, 2023). Consequently, brake discs must combine high thermal capacity with efficient heat dissipation (Stefanelli *et al.*, 2024; Zhang & Zheng, 2024).

The primary objective of this study is to assess the influence of internal vent geometry on heat transfer and structural performance in ventilated rotors subjected to high-energy braking. Previous studies have developed theoretical models of disc temperature evolution (Talati & Jalalifar, 2008), applied FE methods to transient rotor heating (Gao & Lin, 2002), and demonstrated the predictive capability of FE-based thermal analyses (Belhocine & Bouchetara, 2013). However, systematic comparative investigations of internal vent geometries remain limited, thus motivating the present work.

Ministry of Science and Higher Education
Republic of Poland

This publication has been funded by the Polish Ministry of Science and Higher Education under the Excellent Science II programme "Support for scientific conferences".
The content of this article was presented during the 61st Symposium "Modelowanie w mechanice" (Modelling in Mechanics), Szczyrk, Poland, March 2–5, 2025.

2. Object of research

The analysed braking system is based on that of a Porsche Cayenne S Diesel (2013–2016). The front ventilated brake rotor has a diameter of 360 mm, which is typical for heavy sport utility vehicles (SUVs) and comparable to many electric vehicles in terms of thermal loading. The calliper is a six-piston design with pistons of 36 mm diameter each. In the numerical model, both pad-disc interfaces are accounted for through the normal force applied to the disc, calculated using Eq. (2.1), where A denotes the total effective area of all pistons acting on both sides of the rotor:

$$F = p \cdot A, \tag{2.1}$$

where F is the normal force acting on the brake pistons [N], p is the hydraulic pressure at the calliper inlet [Pa], A is the total effective area of all pistons acting on both sides of the rotor [m^2].

This axial force is transmitted to the brake disc, generating tangential friction force which depends on the coefficient of friction between the brake pad material and the disc:

$$F_f = F \cdot \mu, \tag{2.2}$$

where F_f is the friction force [N], μ is the coefficient of friction [–].

Since the brake pad contacts the disc at a finite radial distance from the disc axis, a braking torque is generated that enables the deceleration. This can be calculated as

$$M = F_f \cdot R', \tag{2.3}$$

where M is the braking torque [Nm], R' is the effective (nominal) braking radius [m].

Using the above formulas, the following input data are presented in Table 1 (Kalamegam *et al.*, 2025).

Table 1. Input parameters for braking torque estimation.

Total contact area of six brake pistons [mm^2]	6104.16
Hydraulic pressure at the brake calliper inlet [bar]	120
Normal force acting on brake pistons [N]	75 081
Coefficient of friction (assumed)	0.45
Average effective radius of friction force [mm]	150
Braking torque [Nm]	5000

2.1. Dynamometer tests of the friction coefficient

The experimental tests were conducted on a dynamometer stand designed to reproduce emergency braking conditions. The stand enables the simulation of braking torque, normal pressure, and disc rotational speed representative of real road conditions (Fig. 1). Pressure and torque were continuously monitored using high-precision sensors, while disc temperature was measured using thermocouples embedded in the disc body.

The hydraulic pressure measured at the outlet of the brake hose was approximately 12.6 MPa. This value corresponds to the actual pressure recorded on the vehicle under maximum braking conditions using a manometer. On the dynamometer stand, pressure was measured at an equivalent location corresponding to the brake hose connection; therefore, the same measurement approach was applied in both the experimental and numerical investigations.

Figure 2 presents the hydraulic pressure recorded during consecutive emergency braking events. The braking pressure remains within comparable limits; however, during the second emergency braking, the pressure increases to the maximum value achievable by the test stand,

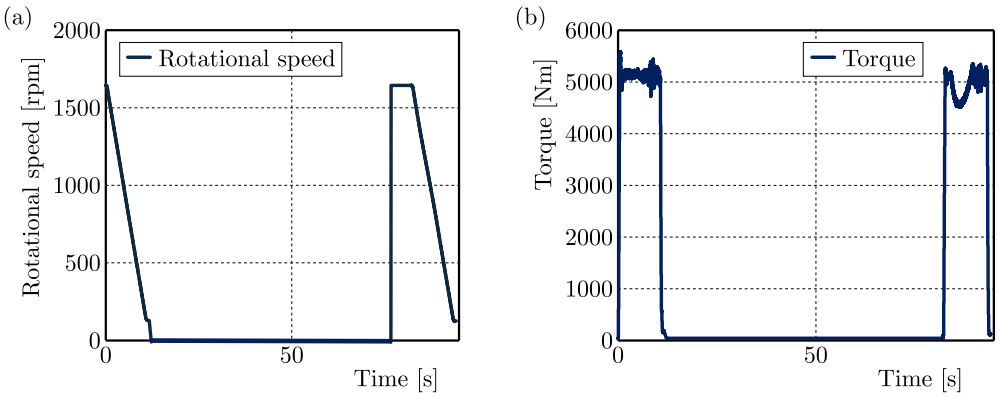

Fig. 1. (a) Rotational speed of the disc as a function of time; (b) braking torque as a function of time.

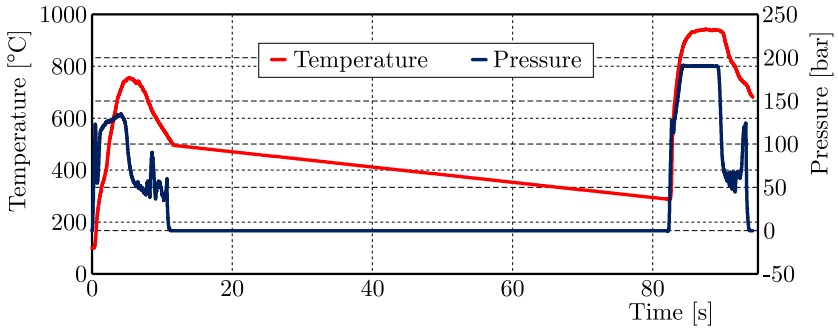

Fig. 2. Measured maximum temperature and pressure as functions of time during the test.

approximately 18 MPa. This increase can be attributed to phenomena such as partial degradation of the pad material, the onset of local fade and increased frictional instability. Although higher pressure is recorded, the effective contact stress at the pad–disc interface is reduced due to the distribution of forces over the piston area.

The friction coefficient was determined based on the measured braking torque, rotational speed, and hydraulic pressure using the following general relationship:

$$\mu(t) = \frac{M(t)}{p(t) \cdot A \cdot R'}, \tag{2.4}$$

where $\mu(t)$ is the friction coefficient, $p(t)$ is the hydraulic inlet pressure [Pa].

This equation reflects the actual test conditions, as both braking torque and hydraulic pressure were directly recorded during the experiments. The relationship between the torque and pressure signals was used to compute the temperature-dependent friction coefficient, providing a realistic $\mu(T)$ characteristic for simulation purposes.

The results indicate that the brake pad can maintain effective performance across a relatively wide temperature range. However, a noticeable drop in the friction coefficient occurs when temperatures exceed approximately 800 °C, as shown in (Fig. 2). During the second emergency braking event the dynamometer attempted to maintain constant braking torque and system inertia by automatically compensating for the falling friction coefficient through an increase in hydraulic pressure. Consequently, the pressure curve reached a maximum value of about 18 MPa, while the disc surface temperature exceeded 1000 °C. This phenomenon corresponds to brake fade, effectively concluding the simulation, since subsequent data no longer reflect realistic operating conditions.

The obtained data highlight the ineffectiveness of the tested braking system under high-temperature operating conditions. The primary issue lies in the insufficient cooling rate of the

brake disc. As a result, the disc temperature before the second braking event remained at approximately 300 °C, in contrast to 100 °C at the beginning of the first braking.

2.2. Determination of the friction coefficient using experimental data

To improve the performance of the investigated braking system, the friction coefficient was determined as a function of temperature. Experimental data from Table 1, together with recorded time-dependent pressure and braking torque, were used to calculate the temperature-dependent friction coefficient employing the Coulomb–Moreau model. Subsequently, the LuGre friction model was implemented, utilising the friction coefficient obtained from the Coulomb-Moreau formulation. The LuGre friction coefficient was calculated according to Eq. (2.4), following Andrzejewski (2005):

$$\mu_L(t) = \mu_C(t) + (\mu_{\max} - \mu_C(t)) + \exp\left(\left(\frac{v_s}{v}\right)^2\right), \tag{2.5}$$

where $\mu_L(t)$ is the LuGre friction coefficient as a function of time [–], $\mu_C(t)$ is the Coulomb–Moreau friction coefficient as a function of time [–], $\mu_{\max}$ is the maximum calculated Coulomb–Moreau friction coefficient [–], v_s is the theoretical initial vehicle velocity, determined from the effective tyre radius at the road contact point [m/s], and v is the actual initial vehicle velocity [m/s]. The parameters used in the calculations are summarized in Table 2.

Table 2. Parameters utilised in the friction coefficient calculations.

Tyre size	295/35/R21
Nominal tyre radius [mm]	369.95
Tyre deflection during braking [mm]	1
Effective tyre radius at contact [mm]	359.95
Actual initial vehicle speed [km/h]	230
Theoretical vehicle speed v_s [km/h]	226.89

Using the parameters listed above, friction coefficient-temperature characteristics were obtained and are presented in Fig. 3.

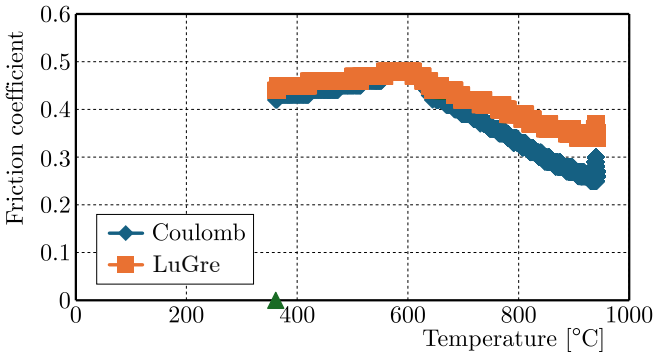

Fig. 3. Friction coefficient as a function of temperature calculated using Eqs. (2.4) and (2.5).

3. Numerical simulation of the original brake disc

The braking system was modelled using ANSYS Workbench. The geometry of the brake disc was developed and a finite element model was subsequently generated. The discretisation consisted of 441 440 tetrahedral elements and 739 304 nodes. The resulting geometry and finite element mesh are shown in Fig. 4.

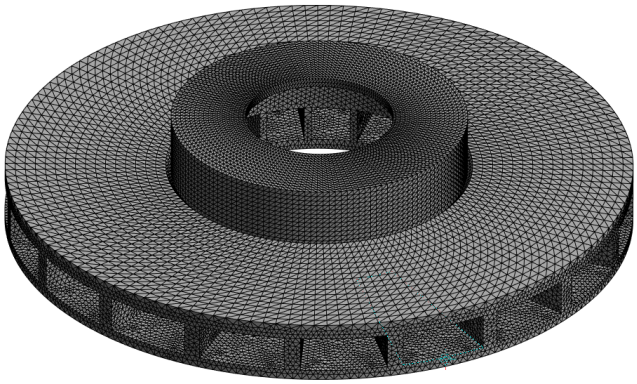

Fig. 4. Finite element mesh of the braking system.

Boundary conditions were applied to the model in the form of heat fluxes representing the thermal load generated by the brake pads during braking. These heat fluxes were imposed on the friction surfaces of the brake disc, where heat generation occurred. In addition, convective heat transfer was applied to the disc surfaces to account for cooling by the surrounding air.

Based on the experimental data, convective heat transfer was divided into two distinct mechanisms:

- localised convective heat transfer acting in regions characterised by intensified air turbulence, such as the ventilation channels and friction tracks of the disc,
- temperature-dependent surface convection applied exclusively to the inner and outer faces of the disc, with the heat transfer coefficient defined as a function of surface temperature.

The time-dependent convection coefficients used in the numerical simulations are summarised in Table 3.

Table 3. Convective heat transfer coefficients [W/(m$^2 \cdot$°C)] as a function of time [s] for a temperature of $T = 22$ °C.

Places where turbulent fluid flow is suspected		Places where laminar fluid flow is suspected	
Time [s]	Convection coefficient [W/(m$^2 \cdot$°C)]	Time [s]	Convection coefficient [W/(m$^2 \cdot$°C)]
0	90	0	70
1	90	1	70
2	92	2	72.5
3	94	3	75
4	97	4	77.5
5	106	5	80
6	120	6	87
6.67	110	6.67	88
7	95	7	85
20	76	20	76
40	72	40	72
83	70	83	70

Subsequently, the remaining material properties were introduced into the model, including temperature-dependent Young's modulus, Poisson's ratio, and specific heat capacity (Agrawal *et al.*, 2024). These properties are essential for accurately capturing the coupled thermal and

structural response of the brake disc under elevated-temperature conditions (De Freitas *et al.*, 2023; Kalamegam *et al.*, 2025). The applied material data are presented in Fig. 5 and Table 4.

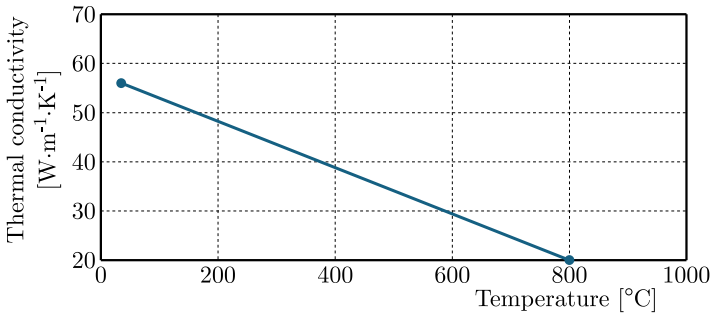

Fig. 5. Thermal conductivity as a function of temperature (Bentz & Prasad, 2007).

Table 4. Specific heat as a function of temperature (Kim *et al.*, 2012).

	Temperature [°C]	Specific heat $[\mathrm{J \cdot kg^{-1} \cdot K^{-1}}]$
1	0	447
2	100	470
3	200	505
4	300	555
5	400	610
6	500	670
7	600	740
8	700	850

To determine the heat flux applied to the brake disc surface during braking, the following procedure was adopted. The total kinetic energy of the vehicle was first calculated as

$$KE = \frac{m\Delta v^2}{2} = \frac{2700 \cdot 63.5^2}{2} = 5\,645\,150\,[\mathrm{J}], \tag{3.1}$$

where KE is the total kinetic energy of the moving vehicle [J], m is the vehicle mass with a full fuel tank and full load [kg], and v is the vehicle velocity [m/s].

The calculations were based on experimental data and standard assumptions. It was assumed that 3 % of the generated heat was absorbed by the brake pad material, while 5 % of the total kinetic energy was dissipated due to aerodynamic drag. After accounting for these losses, 80 % of the remaining energy was assigned to the front axle, in accordance with the ECE R90 regulation. This approach ensures that the energy distribution corresponds to standardised vehicle homologation conditions. Although the exact energy distribution may vary for a specific vehicle, the use of ECE R90 assumptions ensures comparability and reproducibility of the results. Consequently, the portion of kinetic energy dissipated by a single front brake disc was calculated as

$$E = KE \cdot \gamma \cdot k = 5\,645\,150 \cdot (1 - 0.03) \cdot (1 - 0.05) \cdot 0.8 \cdot 0.5 = 2\,080\,802\,[\mathrm{J}], \tag{3.2}$$

where E is the kinetic energy dissipated by one brake disc [J], k is the coefficient accounting for additional energy losses (e.g., aerodynamic drag), and γ is the fraction of energy assigned to the disc under consideration.

The average braking power was then obtained by dividing the dissipated energy by the braking time:

$$P_b = \frac{E}{t} = \frac{2\,080\,802}{5.85} = 356\,117.8\,[\mathrm{W}], \tag{3.3}$$

where t is the braking time [s].

The heat flux q [W/mm^2] applied to the disc friction surfaces was calculated by dividing the braking power by the effective friction surface area A_p [m^2] of the two brake pads in contact with the disc:

$$q = \frac{P_b}{A_p} = \frac{356\,117.8}{0.19} = 1\,874\,304\,[\mathrm{W/m^2}] \sim 2\,[\mathrm{W/mm^2}], \tag{3.4}$$

where A_p is the effective contact area of the pads on both sides of the rotor [m^2], q is the heat flux [W/mm^2].

Finally, the stopping distance s [m] was calculated as

$$s = \frac{v^2}{2 \cdot a} = \frac{63.5^2}{2 \cdot 10.87} = 185.51\,[\mathrm{m}], \tag{3.5}$$

where a is the vehicle deceleration achieved with OE Yokohama Advan Sport V105 tyres [m/s^2].

Based on these results, the input parameters listed in Table 5 were defined for the transient thermal simulation conducted in ANSYS.

Table 5. Input parameters used in the transient thermal and structural simulations conducted in ANSYS.

Number of steps	12
Time step	Program controlled
Heat flux [W/m^2]	2 000 000
Number of nodes	739 304
Number of elements	481 440
Initial temperature [°C]	100

After configuring the aforementioned parameters (López-Flores *et al.*, 2024; Piasecka-Belkhayat & Kowalski, 2018; Najmi *et al.*, 2021; Sainath *et al.*, 2021), the numerical simulation was performed. The finite element analysis yielded the temperature distribution at the instant of maximum thermal loading, as shown in Fig. 6.

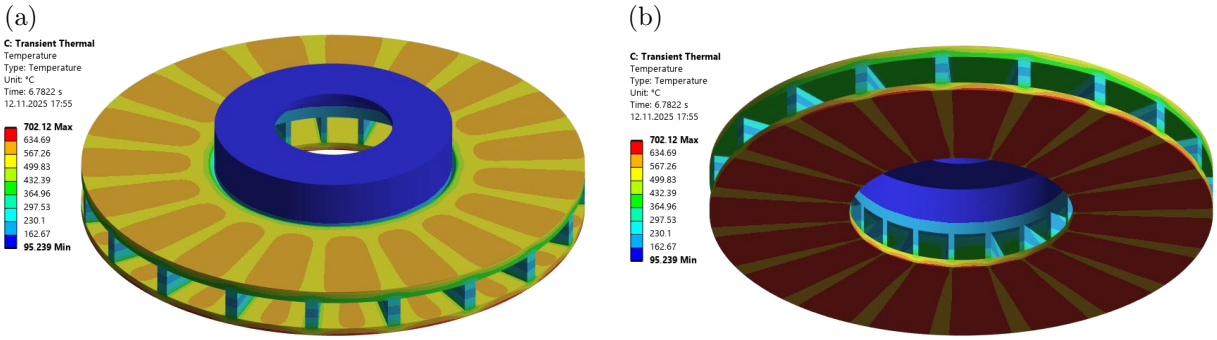

Fig. 6. Temperature distribution in the brake disc: (a) top view; (b) bottom view.

Subsequently, a transient structural analysis was conducted using the temperature field obtained from the thermal simulation as input. This analysis was performed to evaluate the stress and deformation response of the brake disc under thermo-mechanical loading conditions representative of emergency braking. The resulting stress and deformation fields are presented in Fig. 7.

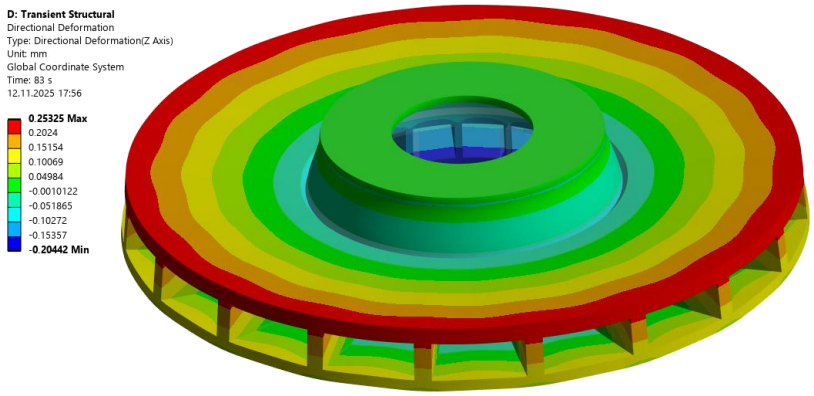

Fig. 7. Contour plots of deformation along the z-axis obtained from the transient structural analysis.

4. Upgrade of the brake disc ventilation

The original brake disc model was upgraded, based on design principles observed in ceramic brake discs commonly used in high-performance applications, including Formula 1 vehicles (Dinesh Kumar & Darius Gnanaraj, 2023). The use of small 13-inch rims constrained the maximum allowable rotor diameter. Consequently, a compact disc rotor with an increased number of smaller ventilation channels was developed. The primary design objectives were to accelerate the cooling process during dynamic driving and to minimise thermally induced deformation of the disc (Al Riyami *et al.*, 2023; Skonieczna & Ptaszny, 2017).

Figure 8 presents the geometry of the upgraded brake disc, together with the corresponding temperature and deformation distributions. To reduce computational cost, only a four-degree sector of the full disc geometry was modelled in the numerical simulations.

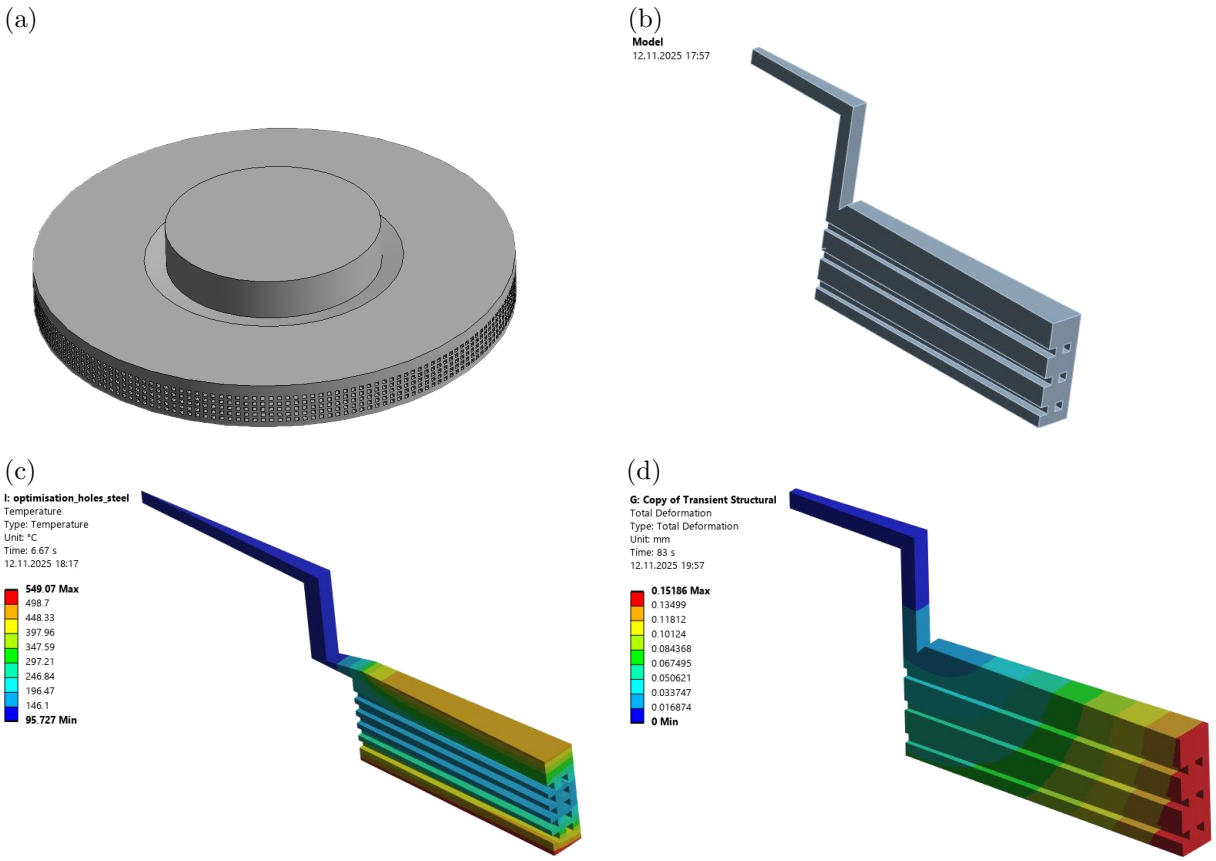

Fig. 8. Braking system: (a) upgraded disc rotor; (b) three-degree part of the rotor; (c) contour plots of temperature during braking; (d) contour plots of deformation during braking.

5. Comparison of temperature variation between the original and upgraded discs

Figure 9 illustrates the temperature distributions obtained for both the original and upgraded brake discs designs under high-load braking conditions. Both variants reached their maximum temperature after approximately 4 s of braking. However, the upgraded disc exhibited a significantly lower peak temperature and a faster cooling rate compared to the original design. This improvement is attributed to enhanced airflow through the redesigned internal ventilation channels, which increased the effective convective heat transfer surface area of the rotor. As a result, the upgraded disc experienced lower average temperatures leading to reduced thermal stress and deformation.

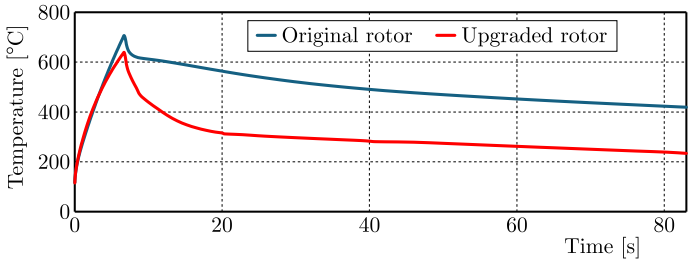

Fig. 9. Relationship between maximum temperature and time for the original rotor, and the upgraded rotor.

Subsequently, the size and number of ventilation holes in the brake disc were optimised to minimise both temperature and stress, while simultaneously reducing the mass of the brake disc (Dinesh Kumar & Darius Gnanaraj, 2023). Disc thickness was also included in the optimisation process. To reduce computational effort, the thermal optimisation objective was restricted to minimising the maximum temperature at the end of the disc cooling simulation. This approach was justified by earlier results, which had already demonstrated the improved thermal performance of the modified disc design.

The optimisation was conducted using the multi-objective genetic algorithm (MOGA) implemented in the ANSYS software. The following parameters were applied:

- an initial population of 42 samples,
- 42 samples per iteration,
- identification of the 3 best candidate solutions,
- a maximum number of 7 iterations.

This methodology enabled an efficient exploration of the design space while balancing competing objectives, including thermal performance, structural integrity, and mass reduction.

Three candidate design configurations were identified (Table 6).

Table 6. Three best candidate configurations found during optimisation.

	Parameter	Candidate point 1	Candidate point 2	Candidate point 3
1	P1-Holes_H [mm]	3.3	3.2246	2.7389
2	P2-Holes_Number	180	179	166
3	P3-Holes_H2 [mm]	3.3093	2.7261	3.0257
4	P4-Holes_Distance-V [mm]	9.5198	9.3847	9.4606
5	P5-Thick_Rotor [mm]	38.168	41.34	40.876
6	P6-Temperature_Maximum [°C]	184.94	260.91	260.45
7	P7-Solid Mass [kg]	0.17938	0.21588	0.2164
8	P8-Equivalent Stress Maximum [MPa]	446.13	526.91	525.77
9	P9-Total Deformation Maximum [mm]	0.24265	0.34941	0.35174

Among these, candidate one exhibited the lowest maximum temperature and stress levels among all analysed configurations. Its parameters were as follows: hole height of 3.3 mm, axial spacing of 3.3 mm, disc thickness of 38.1 mm, distance from the first hole of 9.5 mm, total number of holes of 180, and rotor mass of 15.5 kg.

At the time of the initial study, the mass of the upgraded disc was slightly higher than that of the original model due to the thicker central web required to accommodate the revised duct geometry. Further design development led to the introduction of a honeycomb-style ventilation system, which significantly improved both thermal and structural performance. The honeycomb pattern provided an optimal balance between rigidity and cooling surface area, resulting in a measurable reduction in rotor mass while maintaining lower peak operating temperatures compared to the original design.

6. Conclusions

This study presented a coupled thermal and structural analysis of a ventilated brake disc from the Porsche Cayenne S Diesel braking system. Dynamometer testing demonstrated that the original disc design provided insufficient cooling during repeated emergency braking events, whereas the modified vented design, inspired by motorsport ceramic brake concepts, achieved lower peak temperatures and faster cooling rates, thereby reducing the risk of brake fade.

The LuGre friction model, calibrated using dynamometer data, successfully captured the temperature-dependent behaviour of the pad–disc interface and improved the accuracy of numerical simulations. Optimisation using genetic algorithms identified an optimal disc configuration that effectively balanced thermal efficiency, structural durability, and mass reduction.

Overall, the results emphasise the importance of integrated thermal–structural analysis and optimisation in contemporary brake system design. The proposed methodology offers practical guidance for improving braking systems in heavy SUVs and electric vehicles, where extreme thermal loads are increasingly common.

References

1. Agrawal, V.K., Patil, L.N., Chavan, K.V., & Nimbalkar, U.D. (2024). A computational analysis of heat transfer in solid and vented disc brakes: CFD simulation and thermal performance assessment. *Multiscale and Multidisciplinary Modeling, Experiments and Design*, *7*(5), 4735–4749. https://doi.org/10.1007/s41939-024-00400-y
2. Al Riyami, S.S., Chala, G.T., Bernard, A., & Al Maawali, K. (2023). A case study on thermal analysis of the disc brake used for heavy-duty cars. *PLATFORM – A Journal of Engineering*, *7*(2), 21–32. https://files01.core.ac.uk/download/579834390.pdf
3. Andrzejewski, R. (2005). Models of drive wheel traction. Friction models (in Polish). *Archiwum Motoryzacji*, *1*, 59–76.
4. Belhocine, A., & Bouchetara, M. (2013). Investigation of temperature and thermal stress in ventilated disc brake based on 3D thermomechanical coupling model. *Ain Shams Engineering Journal*, *4*(3), 475–483. https://doi.org/10.1016/j.asej.2012.08.005
5. Bellini, C., Di Cocco, V., Iacoviello, D., & Iacoviello, F. (2024). Temperature influence on brake pad friction coefficient modelisation. *Materials*, *17*(1), Article 189. https://doi.org/10.3390/ma17010189
6. Bentz, D.P., & Prasad, K.R. (2007). *Thermal performance of fire resistive materials. I. Characterization with respect to thermal performance models*. National Institute of Standards and Technology. https://www.researchgate.net/publication/241211063
7. Cristescu, A.C., & Ilie, F. (2023). Influence of travel speed, time, and distance of braking on the efficiency of a car's braking system. *Preprints*, https://doi.org/10.20944/preprints202310.1358.v1
8. De Freitas, T.V.A., Rodrigues, R.N., Costa, C.A.S., Bezerra, R.A., Gonçalves, V.V., Maciel, M.H.C., & Queiroz, D.M. (2023). Influence of design parameters in the brake squeal in electric cars. *Revista Brasileira de Física Tecnológica Aplicada*, *10*(2), 39–53. https://revistas.utfpr.edu.br/rbfta/article/viewFile/17352/9940

9. Dinesh Kumar, P.K., & Darius Gnanaraj, S. (2023). Aluminium-silicon based metal matrix composites for brake rotor applications: a review. *Engineering Research Express*, *5*(2), Article 022002. https://doi.org/10.1088/2631-8695/accdb6
10. Gao, C.H., & Lin, X.Z. (2002). Transient temperature field analysis of a brake in a non-axisymmetric three-dimensional model. *Journal of Materials Processing Technology*, *129*(1–3), 513–517. https://doi.org/10.1016/S0924-0136(02)00622-2
11. Kalamegam, P., Chong, P.L., Faraji, F., Moey, L.K., Manan, M.S.A., & Roy, S. (2025). A comparative study of thermo-mechanical performance of brake rotor discs using finite element analysis. *International Journal on Interactive Design and Manufacturing*, 19(7), 5383–5395. https://doi.org/10.1007/s12008-024-02139-9
12. Kim, B.G., Rempe, J.L., Knudson, D.L., Condie, K.G., & Sencer, B.H. (2012). In-situ creep testing capability for the advanced test reactor. *Nuclear Technology*, *179*(3), 417–428. https://doi.org/10.13182/NT12-A14173
13. López-Flores, J.-G., Cordero-Guridi, J. de J., Ovando-Cuevas, E.R., & Yescas-Ávila, E.A. (2024). Thermal-structural numerical analysis of the brake and disc system of a Formula SAE 2024 type vehicle. *Journal-Mathematical and Quantitative Methods*, *8*(14), Article e30814113. https://doi.org/10.35429/JMQM.2024.8.14.3.13
14. Nadig, D.S., Shivakumar, P., Anoop, S., Chinmay, K., Divine, P.V., & Harsha, H.P. (2017). Effects of cryogenic treatment on the wear properties of brake discs. *IOP Conference Series: Materials Science and Engineering*, *171*, Article 012152. https://doi.org/10.1088/1757-899X/171/1/012152
15. Najmi, H., Kumar, N., Himanshu, Singh, A., Singh, R., & Kumar, S. (2021). Thermal analysis of brake disc of an automobile. *IOP Conference Series: Materials Science and Engineering*, *1116*, Article 012146. https://doi.org/10.1088/1757-899X/1116/1/012146
16. Piasecka-Belkhayat, A., & Kowalski, P. (2018). Numerical modeling of heat transfer in biological tissue domain using the fuzzy finite difference method. In R. Owen, R. de Borst, J. Reese, & C. Pearce (Eds.), P*roceedings of the 6th. European Conference on Computational Mechanics (Solids, Structures and Coupled Problems): ECCM 6; 7th. European Conference on Computational Fluid Dynamics: ECFD 7* (pp. 1475–1484). International Center for Numerical Methods in Engineering (CIMNE). http://congress.cimne.com/eccm_ecfd2018/frontal/docs/Ebook-Glasgow-2018-ECCM-VI-ECFD-VII.pdf
17. Sainath, A., Dehadray, P.M., Bharath, P., & Rao, L.B. (2021). The thermal and stress analysis of disc brake. *IOP Conference Series: Materials Science and Engineering*, *1128*, Article 012015. https://doi.org/10.1088/1757-899X/1128/1/012015
18. Skonieczna, D., & Ptaszny, J. (2017). Strengh analysis of the stabilizer bar link (in Polish). In G. Dziatkiewicz, J. Ptaszny, & M. Dziewoński (Eds.), *Metody komputerowe – 2017: Studencka konferencja naukowa, Gliwice, maj 2017* (pp. 65–68). Silesian University of Technology.
19. Stefanelli, A., Aprea, M., Carbone, F., Romagnuolo, F., Caresia, P., & Suero, R. (2024). Integrated thermomechanical analysis of tires and brakes for vehicle dynamics and safety. *Vehicles*, *6*(3), 1637–1647. https://doi.org/10.3390/vehicles6030077
20. Szymczak, T., Kowalewski, Z.L., & Brodecki, A. (2025). Durability tests for the automotive industry. *Journal of Theoretical and Applied Mechanics*, *63*(3), 461–469. https://doi.org/10.15632/jtam-pl/200388
21. Talati, F., & Jalalifar, S. (2009). Analysis of heat conduction in a disk brake system. *Heat and Mass Transfer*, *45*(8), 1047–1059. https://doi.org/10.1007/s00231-009-0476-y
22. Zhang, Z., & Zheng, S. (2024). Characterization of temperature rise of carbon ceramic brake disc. *Journal of Physics: Conference Series*, *2827*, Article 012011. https://doi.org/10.1088/1742-6596/2827/1/012011

Manuscript received June 24, 2025; accepted for publication November 6, 2025; published online January 20, 2026.

JOURNAL OF THEORETICAL
AND APPLIED MECHANICS
64, 1, pp. 15–27, Warsaw 2026
https://doi.org/10.15632/jtam-pl/213898

VIBRATION FATIGUE BEHAVIOUR ANALYSIS OF THE CRACKED PLATE UNDER A UNIFORM TEMPERATURE FIELD

Yijiang MA*, Zijie ZOU, Jinfeng CHEN, Renjie SHEN

School of Naval Architecture and Ocean Engineering, Jiangsu University of Science and Technology, China
*corresponding author, *yima@nuaa.edu.cn*

For the thermal fatigue problem of the hypersonic aircraft's plate, a loose coupling analysis method is proposed to conduct vibration fatigue behaviour analysis of the cracked plate under a uniform temperature field. The temperature field is converted into additional loads, and the interaction mechanism between thermal coupling and crack propagation is explored. The modal, dynamic response and fatigue life analyses are conducted synchronously. The numerical simulation method is applied to verify this theoretical method. The results indicate that the analytical method proposed has sufficient computational accuracy, and the influence of the temperature field on vibration fatigue behaviour cannot be ignored.

Keywords: crack; temperature field; vibration fatigue behaviour; loose coupling analysis method.

Articles in JTAM are published under Creative Commons Attribution 4.0 International.
Unported License https://creativecommons.org/licenses/by/4.0/deed.en.
By submitting an article for publication, the authors consent to the grant of the said license.

1. Introduction

Hypersonic aircraft refers to the aircraft that travel at speeds exceeding 5 Mach. These types of aircraft have revolutionary potential in military, aerospace, and civilian fields due to extremely high speed, but also face technological problems. During prolonged hypersonic flights, aircraft fuselage plates generate extremely high temperatures due to air friction, posing significant challenges to the dynamic design and thermal protection. In a high-temperature and high-frequency vibration environment, there is an interaction between thermal coupling and crack propagation. Therefore, conducting the vibration fatigue behaviour analysis of the plate under a uniform temperature field has high engineering value.

Vibration fatigue behaviour analysis includes three parts: modal analysis, dynamic response analysis, and fatigue life analysis. In modal analysis, scholars have conducted extensive research work. Based on Kirchhoff's thin plate theory, Huang *et al.* (2018) derived the displacement tolerance function of a thin plate with elastic boundary conditions, and conducted modal analysis of the cracked rectangular plate using the Rayleigh-Ritz method. Xue and Wang (2019) used the Kirchhoff plate theory to describe the singularity of the stress field at the crack tip through a special allowable function, and the Ritz method was applied to investigate the influence of cracks on modal behaviour. Moradi *et al.* (2019) derived the vibration differential equation of a cracked plate based on the Mindlin plate theory, and analysed the influence of load and crack on a model of the plate by the differential quadrature element method. Heo *et al.* (2020) validated the boundary dynamics Mindlin plate equation through numerical methods, and conducted the free vibration analysis of the cracked plate. Song *et al.* (2022) derived the allowable function within the Kirchhoff plate theory framework based on Jacobi orthogonal polynomials, and applied the Ritz method to analyse the free vibration of a cracked polygonal thin plate. Dynamic response analysis mainly investigates the vibration response of the plate under external excitation. Useche (2020) established a numerical model of cracks by the double boundary ele-

ment equation, and proposed a method to investigate the bending vibration response of cracked plates based on the double reciprocity boundary element method. Based on the Kirchhoff plate theory, Jalili and Daneshmehr (2018) established a non-linear model of cracked plates and investigated the time-domain response of cracked plates characterized. Motaharifar *et al.* (2020) applied an improved line spring model to simulate through cracks, and conducted non-linear vibration response analysis of cracked von Kármán plates. Based on the Mindlin plate theory, Xue *et al.* (2020) simulated the stress field at the crack tip by angle displacement tolerance functions, and studied the non-linear vibration response of the cracked plate using Hamilton's principle. In fatigue life analysis, scholars have proposed various analytical methods. Jameel and Harmain (2019) applied the meshless Galerkin method to discretize the crack area, and proposed a fatigue crack propagation and life prediction method for a cracked plate. Ilie and Ince (2022) established the numerical model of a cracked plate using the ANSYS reduced order model and embedded the Paris equation into the fatigue crack growth module to conduct vibration fatigue life analysis. Tazoe *et al.* (2020) simplified cracks into a set of particle voids and proposed a crack propagation algorithm based on smooth particle fluid mechanics to analyse the crack propagation behaviour. Yadzhak *et al.* (2022) established a deformation parameter model for

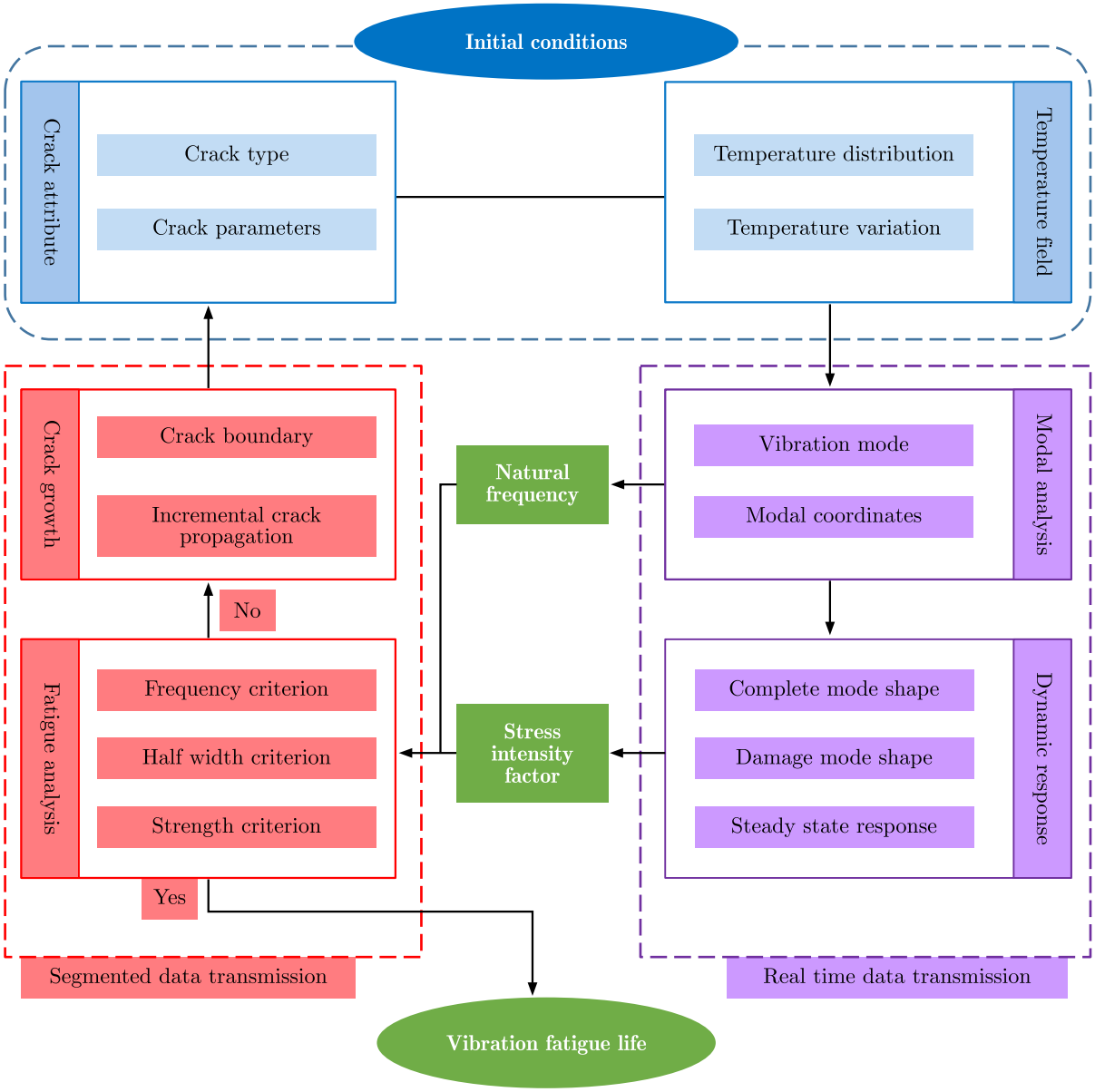

Fig. 1. Research process on vibration fatigue behaviour of the cracked plate.

crack tip opening displacement based on the energy method, and studied the crack propagation law under type II and III mixed loads to determine the fatigue life. The aforementioned research proposes multiple methods for vibration fatigue behaviour analysis of the cracked plate at room temperature, but does not consider the influence of temperature field distribution. The vibration fatigue behaviour analysis method in a normal temperature environment is not applicable to a variable temperature field environment.

In this paper, a loose coupling analysis method is proposed to investigate the vibration fatigue behaviour of the cracked plate. Based on the plate constitutive equation, the temperature field and stress field distribution can be investigated. Considering the interaction between thermal coupling and crack propagation, the additional thermal stress matrix and thermal deformation stiffness matrix can be derived. According to the Paris equation, the influence of the temperature field on the plate's fatigue life can be analysed. Based on the thermal stress and thermal modal analysis, the influence of temperature on vibration fatigue life is investigated, and the possibility of health monitoring of plates in service is provided. The research process of the loose coupling analysis method is shown in Fig. 1.

2. Vibration fatigue behaviour analysis

2.1. Vibration differential equation

Assumptions of the thin plate are as follows: the material is fully elastic, homogeneous, and isotropic; the thickness of the thin plate is uniform and much smaller than the other sizes; all strain components are small enough and satisfy Hooke's law; all transverse normal stress components and shear deformations, and the cross-sections satisfy the plane assumption; the moment of inertia and shearing forces of the plate are neglected. Based on the Kirchhoff plate theory (Israr, 2008), the vibration differential equation of the cracked plate can be expressed as follows:

$$\rho h\frac{\partial^2 w}{\partial t^2}+D_T\left(\frac{\partial^4 w}{\partial x^4}+2\frac{\partial^4 w}{\partial x^2\partial y^2}+\frac{\partial^4 w}{\partial y^4}\right)=n_x\frac{\partial^2 w}{\partial x^2}+2n_{xy}\frac{\partial^2 w}{\partial x\partial y}+n_y\frac{\partial^2 w}{\partial y^2}+\frac{\partial^2\overline{M_x}}{\partial x^2}+\frac{\partial^2\overline{M_y}}{\partial y^2}+\overline{n_x}\frac{\partial^2 w}{\partial x^2}+\overline{n_y}\frac{\partial^2 w}{\partial y^2}+P_z, \tag{2.1}$$

where $D_T=E_T h^3/12\left(1-v^2\right)$ is the flexural rigidity, w is the displacement in the z-direction of the mid-surface, ρ is the density, h is the thickness, E_T is the elastic modulus at different temperatures, v is Poisson's ratio and t is time, $\overline{n_x}$ and $\overline{n_y}$ are unit length additional surface forces in x- and y-axis directions caused by cracks, n_x and n_y are unit length additional surface forces in x- and y-axis directions caused by temperature changes, $\overline{M_x}$ and $\overline{M_y}$ are the unit length additional bending moments in the x- and y-axis directions caused by cracks, P_z is the external load on the plate.

Let us assume that $P_z=0$, and Eq. (2.1) becomes the free vibration differential equation. The crack is parallel to the x-axis and only the additional surface load n_x acts, affected by temperature. Therefore, Eq. (2.1) can be simplified:

$$\rho h\frac{\partial^2 w}{\partial t^2}+D_T\left(\frac{\partial^4 w}{\partial x^4}+2\frac{\partial^4 w}{\partial x^2\partial y^2}+\frac{\partial^4 w}{\partial y^4}\right)=n_x\frac{\partial^2 w}{\partial x^2}+\frac{\partial^2\overline{M_y}}{\partial y^2}+\overline{n_y}\frac{\partial^2 w}{\partial y^2}+P_z. \tag{2.2}$$

According to the singularity of the stress field at the crack tip, relationships between the nominal tensile stress and bending stress at the crack location and the nominal tensile stress and bending stress away from the crack location are as follows (Rice & Levy, 1972):

$$\sigma=[(1+\gamma\alpha_{bb})\sigma_\infty-\eta\alpha_{tb}\sigma_{b\infty}]/Q, \tag{2.3}$$

$$\sigma_{bb}=[-\gamma\alpha_{tb}\sigma_\infty+(1+\eta\alpha_{tt})\sigma_{b\infty}]/Q, \tag{2.4}$$

$$\begin{cases} \alpha_{tt} = 290.18\xi^{10} - 460.87\xi^{9} + 437.12\xi^{8} - 211.98\xi^{7} \\ \qquad + 99.19\xi^{6} - 33.64\xi^{5} + 18.6\xi^{4} - 0.54\xi^{3} + 1.97\xi^{2}, \\ \alpha_{bb} = 61.58\xi^{10} - 127.86\xi^{9} + 147.8\xi^{8} - 103.66\xi^{7} \\ \qquad + 63.77\xi^{6} - 31.34\xi^{5} + 14.46\xi^{4} - 3.29\xi^{3} + 1.98\xi^{2}, \\ \alpha_{tb} = 133.68\xi^{10} - 244.67\xi^{9} + 257.08\xi^{8} - 153.95\xi^{7} \\ \qquad + 84.07\xi^{6} - 34.87\xi^{5} + 16.0\xi^{4} - 1.91\xi^{3} + 1.97\xi^{2}, \end{cases} \tag{2.5}$$

where σ, σ_{bb} are the nominal tensile stress and bending stress at the crack location, σ_{∞}, $\sigma_{b\infty}$ are the nominal tensile stress and bending stress away from crack location, $\eta = \left(1-\nu^2\right)h/(2a)$, $\gamma = 3\,(3+\nu)\,(1-\nu)h/(2a)$, $Q = (1+\eta\alpha_{tt})\,(1+\gamma\alpha_{bb}) - \eta\gamma(\alpha_{tb})^2$, α_{bb}, α_{tt}, and α_{tb} are the local flexibility caused by cracks, a is the half width of the crack, ξ is the relative depth of the crack.

In fact, σ_{∞}, $\sigma_{b\infty}$, and the nominal stress magnitude are consistent with the absence of cracks at the crack location, and are expressed as follows:

$$\sigma_{\infty} = N_{\infty}/h = \int_{-h/2}^{h/2} (\tau_{ij}(x,0,z)/h)\,\mathrm{d}z, \tag{2.6}$$

$$\sigma_{b\infty} = 6M_{\infty}/h^2 = \int_{-h/2}^{h/2} (6z\tau_{ij}(x,0,z)/h^2)\,\mathrm{d}z, \tag{2.7}$$

where N_{∞} and M_{∞} are the tension and bending moment per unit length in the y-axis direction, respectively, when $y=0$, $\tau_{ij}(x,0,z)$ is the stress on the cross-section when $y=0$.

By replacing nominal tensile stress and nominal bending stress with tension and the bending moment, the additional tension and bending moment caused by cracks can be obtained as follows:

$$\overline{n_y} = [-(1+\gamma\alpha_{bb})N_{\infty} + 6\eta\alpha_{tb}M_{\infty}/h]/Q, \tag{2.8}$$

$$\overline{M_y} = [\gamma\alpha_{tb}hN_{\infty}/6 - (1+\eta\alpha_{tt})M_{\infty}]/Q. \tag{2.9}$$

Let us substitute Eqs. (2.8) and (2.9) into Eq. (2.2), and Eq. (2.2) can be simplified as follows:

$$\begin{aligned} D_T\left(\frac{\partial^4 w}{\partial x^4} + 2\frac{\partial^4 w}{\partial x^2\partial y^2} + \frac{\partial^4 w}{\partial y^4}\right) = & -\rho h\frac{\partial^2 w}{\partial t^2} + n_x\frac{\partial^2 w}{\partial x^2} - \phi N_{\infty}\frac{\partial^2 w}{\partial y^2} \\ & - \varphi\frac{\partial^2 M_{\infty}}{\partial y^2} + \lambda M_{\infty}\frac{\partial^2 w}{\partial y^2}, \end{aligned} \tag{2.10}$$

where N_{∞} is determined by the middle surface strain, M_{∞} is determined by internal force conditions of the Kirchhoff plate, other parameters are as follows: $M_{\infty} = -D_T(\partial^2 w/\partial y^2 + \nu\partial^2 w/\partial x^2)$, $\phi = (1+\gamma\alpha_{bb})/Q$, $\varphi = (1+\eta\alpha_{tt})/Q$, $\lambda = 6\eta\alpha_{tb}/(hQ)$.

2.2. Modal and dynamic response analysis

In order to simplify the analysis process, the influence of high-order modes is ignored, and the cracked plate is simplified into a single degree of freedom system by the Galerkin method. The general solution of the vibration differential equation for the cracked plate is as follows:

$$w(x,y,t) = \sum_{q=1}^{\infty}\sum_{p=1}^{\infty} A_{pq}X_pY_q\psi_{pq}(t), \tag{2.11}$$

where X_p and Y_q are vibration mode functions of the cracked plate, A_{pq} is the first-order amplitude, $\psi_{pq}(t)$ is the modal coordinate function of the cracked plate.

Convert the horizontally concentrated load into a uniformly distributed load by a δ function:

$$\overline{P_z} = P_0(t)\delta(x - x_0)\delta(y - y_0). \tag{2.12}$$

Let us substitute Eqs. (2.11) and (2.12) into Eq. (2.10), and Eq. (2.10) can be simplified as follows:

$$\begin{aligned}\frac{\rho h\ddot{\psi}_{pq}A_{pq}X_pY_q}{D_T} + [(Y_qX_p^{(4)} + 2X_p''Y_q'' + X_pY_q^{(4)}) - \varphi(X_pY_q^{(4)} + \nu X_p''Y_q'')]A_{pq}\psi_{pq} \\ + \lambda[X_p^2(Y_q'')^2 + \nu X_pY_qX_p''Y_q'']A_{pq}^2\psi_{pq}^2 + \frac{(-n_xX_p''Y_q + \phi N_\infty X_pY_q'')A_{pq}\psi_{pq}}{D_T} \\ = \frac{P_0(t)\delta(x - x_0)\delta(y - y_0)}{D_T}.\end{aligned} \tag{2.13}$$

Based on the strain energy caused by the second invariant of the applied surface strain, Berger (1955) determined the deformation of the same magnitude, and the surface load n_x and N_∞ can be obtained in the following way:

$$\begin{cases} n_x = D_TF_{1pq}A_{pq}^2\psi_{pq}^2, \\ N_\infty = D_TF_{2pq}A_{pq}^2\psi_{pq}^2, \end{cases} \tag{2.14}$$

$$\begin{cases} F_{1pq} = \dfrac{6}{h^2l_1l_2}\displaystyle\sum_{q=1}^{\infty}\sum_{p=1}^{\infty}\int_0^{l_1}\int_0^{l_2}\left[(X_p')^2Y_q^2 + \nu(Y_q')^2X_p^2\right]\mathrm{d}x\,\mathrm{d}y, \\ F_{2pq} = \dfrac{6}{h^2l_1l_2}\displaystyle\sum_{q=1}^{\infty}\sum_{p=1}^{\infty}\int_0^{l_1}\int_0^{l_2}\left[(Y_q')^2X_p^2 + \nu(X_p')^2Y_q^2\right]\mathrm{d}x\,\mathrm{d}y. \end{cases} \tag{2.15}$$

Let us substitute Eq. (2.14) into Eq. (2.13), and integrate Eq. (2.13) within the plate area:

$$M_{pq}\ddot{\psi}_{pq} + K_{pq}\psi_{pq} + H_{pq}\psi_{pq}^2 + G_{pq}\psi_{pq}^3 = P_{pq}, \tag{2.16}$$

$$\begin{cases} M_{pq} = \dfrac{\rho h}{D_T}\displaystyle\sum_{q=1}^{\infty}\sum_{p=1}^{\infty}A_{pq}\int_0^{l_1}\int_0^{l_2}X_p^2Y_q^2\,\mathrm{d}x\,\mathrm{d}y, \\ K_{pq} = \displaystyle\sum_{q=1}^{\infty}\sum_{p=1}^{\infty}A_{pq}\int_0^{l_1}\int_0^{l_2}\left[-\varphi(X_pY_q'''' + \nu X_p''Y_q'') + Y_qX_p'''' \right. \\ \qquad \left. + 2X_p''Y_q'' + X_pY_q''''\right]X_pY_q\,\mathrm{d}x\,\mathrm{d}y, \\ H_{pq} = \displaystyle\sum_{q=1}^{\infty}\sum_{p=1}^{\infty}\lambda A_{pq}^2\int_0^{l_1}\int_0^{l_2}X_pY_q\left[(X_pY_q'')^2 + \nu X_p''Y_qX_pY_q''\right]\mathrm{d}x\,\mathrm{d}y, \\ G_{pq} = \displaystyle\sum_{q=1}^{\infty}\sum_{p=1}^{\infty}A_{pq}^3\int_0^{l_1}\int_0^{l_2}X_pY_q\left(-F_{1pq}X_p''Y_q + \phi F_{2pq}X_pY_q''\right)\mathrm{d}x\,\mathrm{d}y, \\ P_{pq} = P_0(t)Q_{pq}/D_T, \\ Q_{pq} = X_p(x_0)Y_q(y_0), \end{cases} \tag{2.17}$$

where M_{pq} is the generalized mass, K_{pq} is the generalized stiffness, H_{pq} is the quadratic non-linear term, G_{pq} is the cubic non-linear term, P_{pq} is the generalized external load.

The vibration differential equation of the cracked plate under sinusoidal excitation $P_0(t) = p\cos(\Omega_{pq}t)$ is transformed into:

$$\ddot{\psi}_{pq} + \omega_{pq}^2\psi_{pq} + \alpha_{pq}\psi_{pq}^2 + \beta_{pq}\psi_{pq}^3 = \chi_{pq}p\cos(\Omega_{pq}t)/D_T, \tag{2.18}$$

where $\omega_{pq} = \sqrt{K_{pq}/M_{pq}}$ is the generalized natural frequency, $\alpha_{pq} = H_{pq}/M_{pq}$, $\beta_{pq} = G_{pq}/M_{pq}$, $\chi_{pq} = Q_{pq}/M_{pq}$.

2.3. Fatigue life analysis

Based on the coupling degree between thermal coupling and fatigue crack propagation, this paper makes the following assumptions: assuming that the time domain is discretized according to the external excitation period, the geometric sizes of the fatigue crack remain unchanged at each time step, and the fatigue crack pattern expands at the moment when each time step ends. Based on this assumption, the temperature field and stress field are in real-time data transmission form, while the analysis of fatigue crack propagation is in segmented data transmission form (data transmission occurs once at the end of each time step). Therefore, a loose coupling analysis method is proposed to carry out modal, dynamic response, and vibration fatigue life analysis of the cracked plate at each time step simultaneously, while achieving decoupling of stress and temperature fields in thin plate structures.

Under normal circumstances, the relationship between the dynamic stress intensity factor at the crack tip and the crack depth can be expressed as

$$\Delta K = F(\xi)\Delta\sigma_d\sqrt{\pi a}, \tag{2.19}$$

where a is the half width of the crack, $F(\xi)$ is the crack correction factor, $\Delta\sigma_d$ is the amplitude of the dynamic stress.

In states of low to medium stress, the Paris equation can simulate crack propagation well:

$$\frac{\mathrm{d}a}{\mathrm{d}N} = C(\Delta K)^m, \tag{2.20}$$

where N is the number of the vibration cycles, C and m are the material constants.

Under cyclic loading, the half width length of the crack after i cycles is as follows:

$$a_i = a_0 + \sum_{j=1}^{i}\Delta a_j, \tag{2.21}$$

where a_0 is the initial half width of the crack.

When estimating vibration fatigue life of thin plate structures with cracks, three failure criteria are used: frequency, half width, and strength (Ostiguy & Evan-Iwanowski, 1982; Shih & Wu, 2002):

1) when the first natural frequency of a cracked thin plate decreases by 5 %, the plate fails,
2) when the relative half width of the crack reaches 5 %, fatigue failure occurs in the plate,
3) when the stress intensity factor reaches material fracture toughness, fatigue failure occurs in the plate.

3. Numerical simulation analysis

The numerical simulation analysis is applied to verify the correctness and feasibility of the theoretical method proposed in this paper. The geometric model and mesh model of the plate

with a transverse crack are established by ANSYS. The crack is simulated by the discontinuity of meshes, and the crack will be always in an open state. In order to objectively describe breathing behaviour of the alternating open-closed crack in a vibration environment, the contact elements are established on both surfaces of the crack. The presence of contact elements prevents the intersection of the crack grids when crack surfaces come into contact, which effectively simulates breathing behaviour of the crack alternating open-closed.

The cracked plate is simply supported on all edges, and the dimensional drawing and finite element model are as shown in Fig. 2 and Fig. 3. Geometric sizes of the cracked plate are as follows: $l_1 = 1\,\mathrm{m}$, $l_2 = 0.5\,\mathrm{m}$, $h = 0.01\,\mathrm{m}$, $a_0 = 0.01\,\mathrm{m}$, $\rho = 2770\,\mathrm{kg/m^3}$, Young's modulus (20°) is $E_{20\,^\circ\mathrm{C}} = 69\,\mathrm{GPa}$. Young's modulus at different temperatures can be obtained:

$$E_T = \alpha E_{20\,^\circ\mathrm{C}}, \tag{3.1}$$

where α is a scale factor, $\alpha = -17.2\times10^{-12}T^4 + 11.8\times10^{-9}T^3 - 34.5\times10^{-7}T^2 + 15.9\times10^{-5}T + 1$.

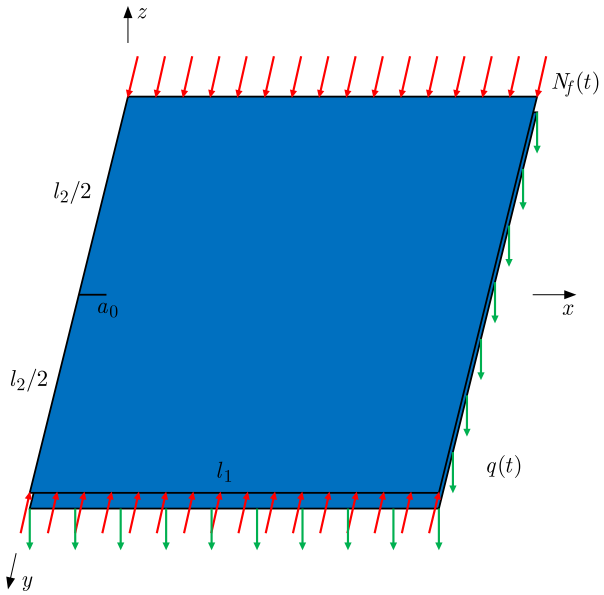

Fig. 2. Geometric dimensions of cracked plate .

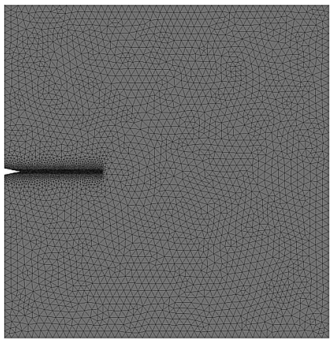

Fig. 3. Finite element model of cracked plate.

4. Results and discussion

4.1. Validation

Assuming that the cracked plate is actuated by two period excitations, one excitation is the in-plane force $N_f(t) = N_0 + N_t \cos\omega_1 t$, and the other is a uniformly distributed load $q(t) = q_t \cos\omega_2 t$ in the z-direction. The natural frequency of the first mode lateral vibration (Ostiguy & Evan-Iwanowski, 1982) is as follows:

$$\omega_L = \omega_T \left(1 - \frac{N_0}{N_{cr}}\right)^{1/2}, \tag{4.1}$$

where ω_T is the natural frequency of the plate, $N_{cr} = \frac{\pi^2 D}{l_1^2(2l_2/l_1 + l_1/2l_2)^2}$ is the static critical load.

The dimensionless natural frequencies can be derived as follows:

$$\Omega = \omega_L a^2 \sqrt{\rho h/D}, \tag{4.2}$$

where ω_L is the linear natural frequency of the cracked plate.

As shown in Table 1, for the non-destructive plate, the maximum error of the first order natural frequencies is less than 0.51 %, compared with the results in (Ostiguy & Evan-Iwanowski, 1982), and the first natural frequency error obtained by the numerical simulation method is lower. Therefore, for modal analysis of the plate, the theoretical method proposed in this paper has really high computational accuracy.

Table 1. Dimensionless natural frequencies of the plate without cracks.

Aspect ratios	a/l_1	N_0/N_{cr}	Ostiguy and Evan-Iwanowski (1982)	Theoretical	Numerical	Error rate [%]
$l_1/l_2 = 1$	0	0.2	17.66	17.572	17.60	0.49
		0.4	15.29	15.218	15.24	0.47
		0.6	12.48	12.425	12.45	0.44
$l_1/l_2 = 2$	0	0.2	44.14	43.914	43.97	0.51
		0.4	38.22	38.031	38.12	0.49
		0.6	31.21	31.052	31.15	0.51

As shown in Table 2, for the plate with different depth of cracks, the maximum error of the first order natural frequencies is less than 1.88 %, compared with the results in (Shih & Wu, 2002), and the first natural frequency error obtained by the numerical simulation method is lower. Therefore, for modal analysis of the cracked plate, the theoretical method proposed in this paper has sufficiently high computational accuracy.

Table 2. Dimensionless natural frequencies of the cracked plate.

Aspect ratios	a/l_1	N_0/N_{cr}	Shih and Wu (2002)	Theoretical	Numerical	Error rate [%]
$l_1/l_2 = 1$	0.01	0.2	17.62	17.579	17.59	0.23
		0.4	15.15	15.223	15.21	0.48
		0.6	12.20	12.430	12.30	1.88
$l_1/l_2 = 2$	0.01	0.2	44.25	43.959	44.12	0.66
		0.4	38.13	38.070	38.82	0.16
		0.6	30.95	31.084	31.02	0.43

4.2. Temperature field

Let us assume that the cracked plate is actuated by the temperature field, and the temperatures are as follows: $-20°$, $20°$, $50°$, $100°$. First order natural frequencies and dimensionless natural frequencies obtained by the theoretical method proposed in this paper are as shown in Table 3.

As shown in Table 3, the influence of the temperature field on the first order natural frequencies and dimensionless natural frequencies is significant and cannot be ignored. The natural frequency of the plate varies considerably when the temperature is within the two ranges $[-20°, 20°]$ and $[50°, 100°]$. Under the same temperature field, as the in-plane load ratio increases, the first order natural frequency of the cracked plate gradually decreases.

Table 3. Dimensionless natural frequencies of the cracked plate at different temperatures.

Aspect ratios	a/l_1	Temperature [°C]	ω_T [rad/s]	N_0/N_{cr}	$\Omega = \omega_L a^2\sqrt{\rho h/D}$
$l_1/l_2 = 1$	0.05	−20	300.0158	0.2	17.8085
				0.4	15.4226
				0.6	12.5925
		20	297.1507	0.2	17.5974
				0.4	15.2398
				0.6	12.4432
		50	297.2512	0.2	17.5972
				0.4	15.2396
				0.6	12.4431
		100	296.2710	0.2	17.6205
				0.4	15.2598
				0.6	12.4596

4.3. Dynamic response analysis

Let us assume that the cracked plate is under a uniformly distributed load $q(t) = q_t \cos\omega_2 t$, where $q_t = 0.8\,\mathrm{kN/m^2}$, and excitation frequencies are $\omega_{-20\,^\circ\mathrm{C}} = 300.0158\,\mathrm{rad/s}$, $\omega_{20\,^\circ\mathrm{C}} = 297.1507\,\mathrm{rad/s}$, $\omega_{50\,^\circ\mathrm{C}} = 297.2512\,\mathrm{rad/s}$, $\omega_{100\,^\circ\mathrm{C}} = 296.2710\,\mathrm{rad/s}$. When the temperature field is −20°, 20°, 50°, 100°, the vibration responses of the cracked plate are shown in Fig. 4 to Fig. 6.

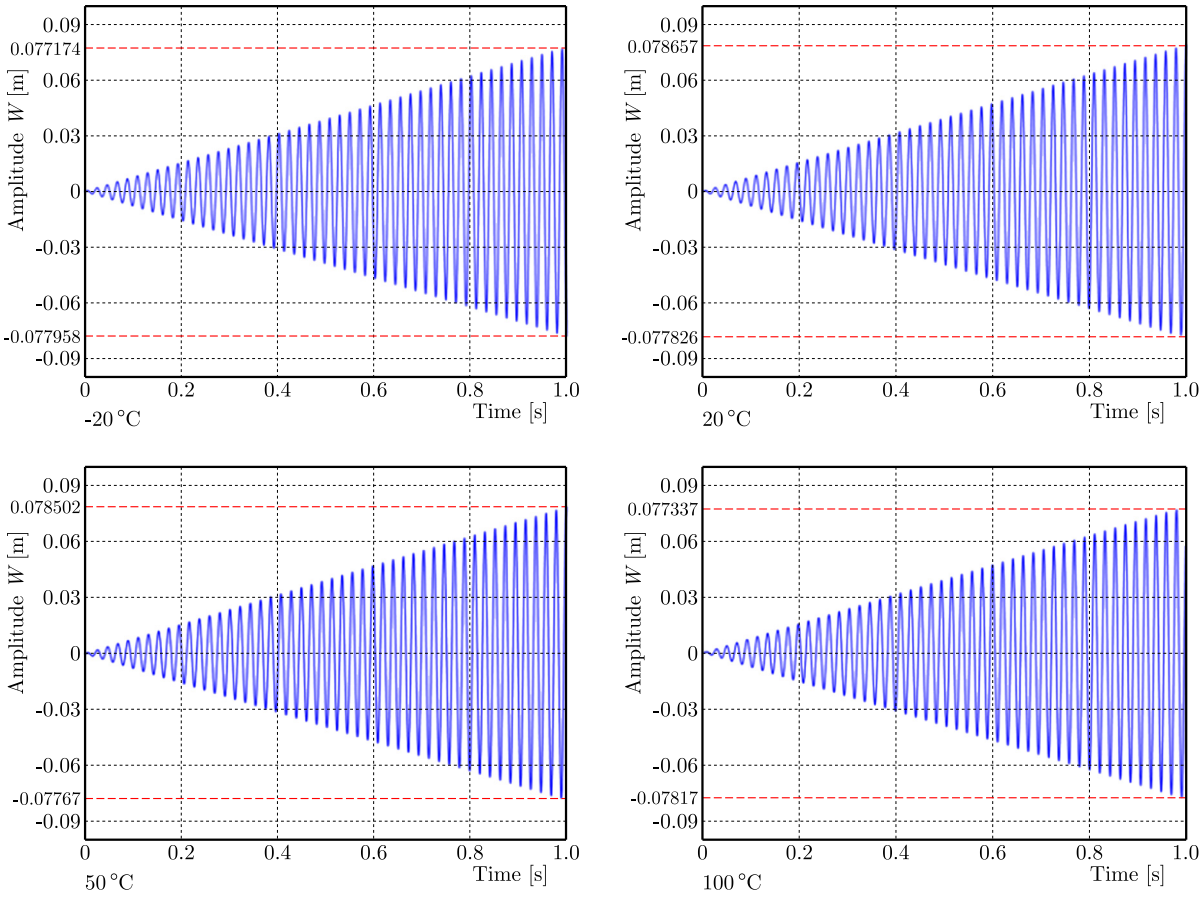

Fig. 4. Vibration response of the cracked plate when $\omega_2 = 300\,\mathrm{rad/s}$, $297\,\mathrm{rad/s}$, $297\,\mathrm{rad/s}$, $296\,\mathrm{rad/s}$.

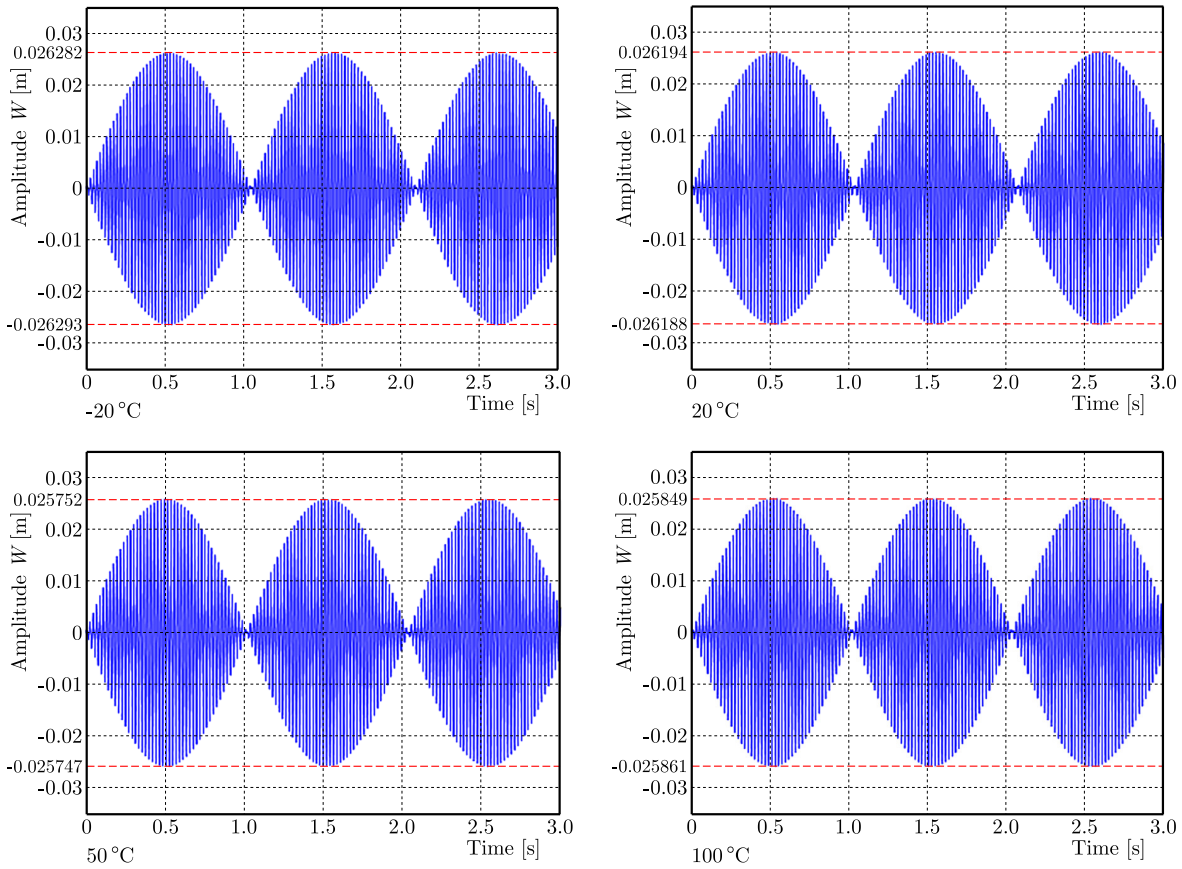

Fig. 5. Vibration response of the cracked plate when ω_2 is 0.98 times the natural frequency.

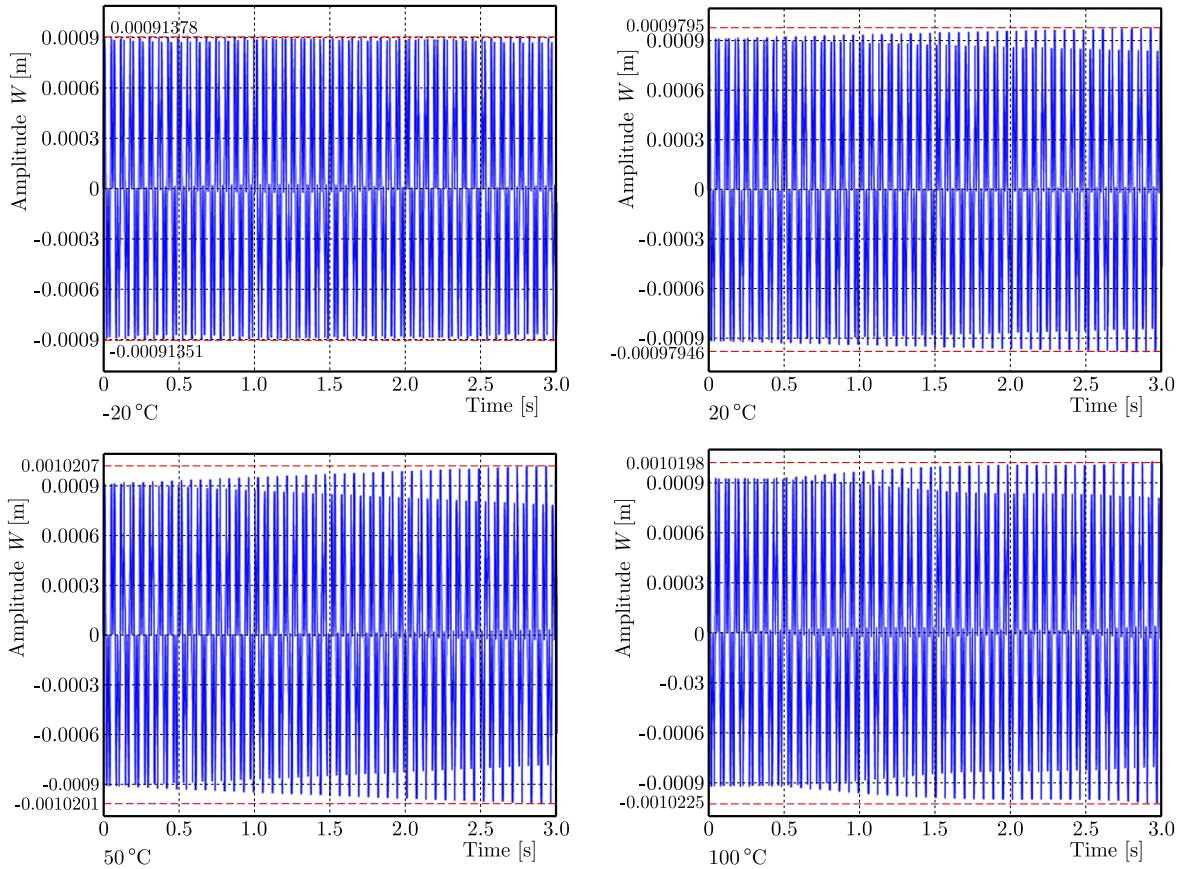

Fig. 6. Vibration response of the cracked plate when ω_2 is 1/3 times the resonant frequency.

As shown in Fig. 4 to Fig. 6, the influence of the external excitation frequency and temperature field on the vibration response of the cracked plate is significant. In Fig. 4, external excitation frequencies ω_2 are replaced by first order natural frequencies 300 rad/s, 297 rad/s, 297 rad/s, 296 rad/s, and the cracked plate will experience resonance phenomena, which causes the vibration amplitude to increase exponentially. In Fig. 5, the external excitation frequency ω_2 is 0.98 times the first order natural frequency, and the vibration response of the cracked plate exhibits a beat phenomenon. As the temperature increases, the beat period gradually shortens. In Fig. 6, the external excitation frequency ω_2 is 1/3 of the first order natural frequency, and the vibration response of the cracked plate exhibits a general response phenomenon.

4.4. Fatigue life analysis

Let us assume that the cracks' initial half widths are 0.03 m, 0.05 m, and 0.07 m, and temperature fields are $-20°$, $20°$, $50°$, $100°$. The external excitation is $q(t) = q_t \cos \omega_2 t$, and $q_t = 10\,\mathrm{N/m^2}$. The material constants are as follows: $C = 1.17 \times 10^{-12}$, $m = 3.447$ (Shih & Wu, 2002). Vibration fatigue life curves of the cracked plate derived by the theoretical method proposed are shown in Fig. 7. The crack propagation process of the plate obtained by the numerical method is shown in Fig. 8, and fatigue life comparison obtained by theoretical and numerical methods is shown in Table 4.

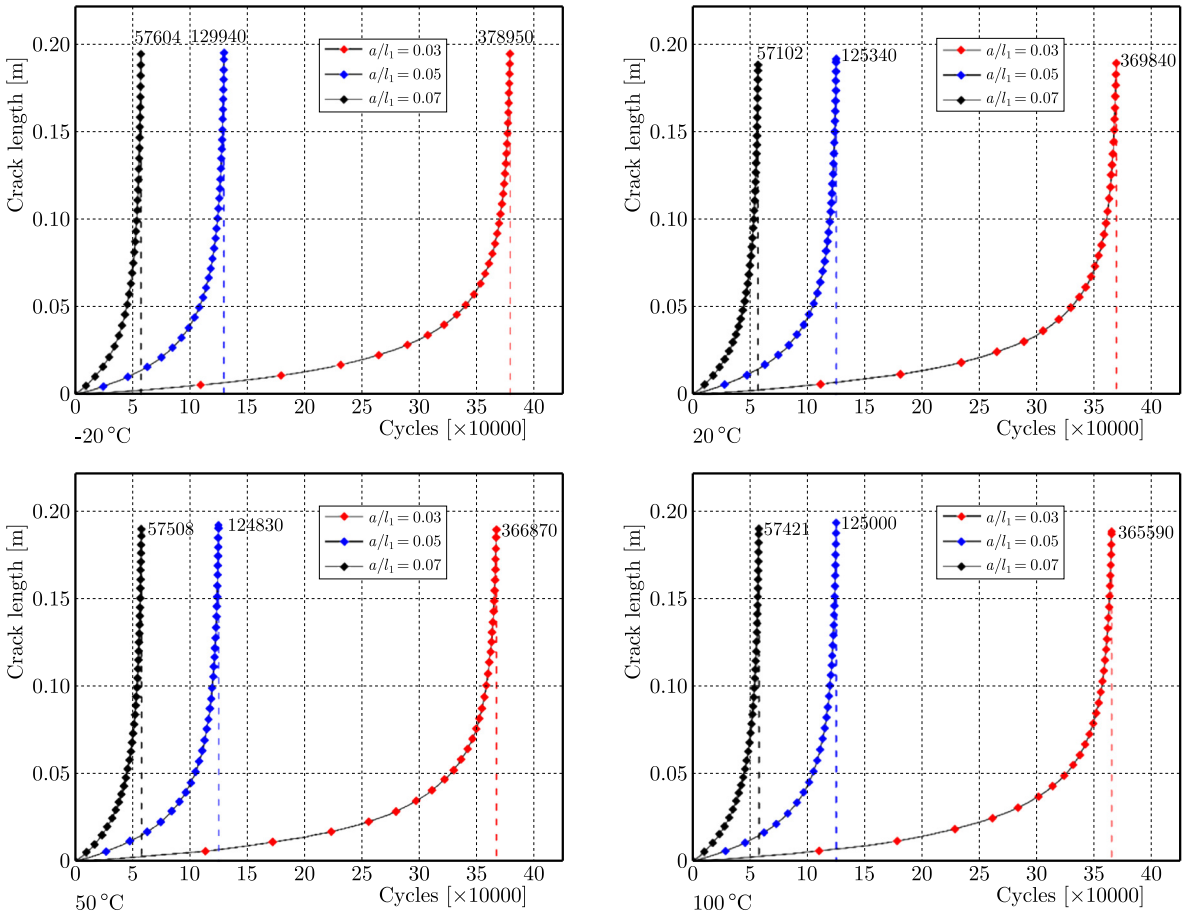

Fig. 7. Fatigue crack growth diagram of a cracked plate with different initial crack length.

As shown in Figs. 7 and 8, the temperature field has a certain influence on the vibration fatigue life of the cracked plate, but the initial mid width of the crack has a significant impact. As the initial half width of the crack increases, the vibration fatigue life rapidly decreases.

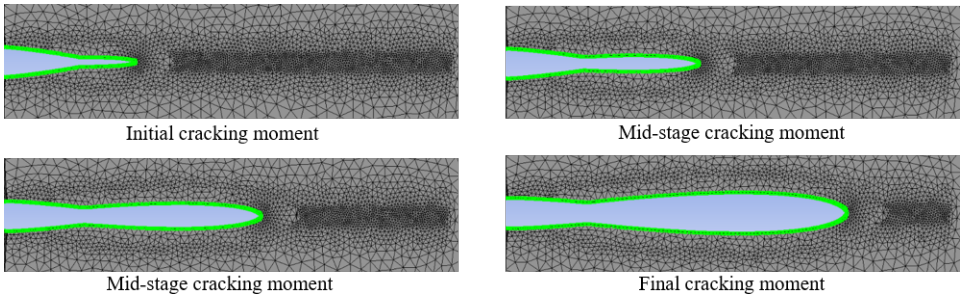

Fig. 8. Cracking process of the fatigue crack.

Table 4. Number of load cycles with a crack length of 0.2 m (×10 000).

a/l_1	−20°		20°		50°		100°		Max error [%]
	Numerical	Theoret.	Numerical	Theoret.	Numerical	Theoret.	Numerical	Theoret.	
0.03	45.07	37.90	44.01	36.98	43.59	36.69	43.65	36.55	19.1
0.05	15.39	12.99	14.83	12.53	14.81	12.48	14.84	12.50	18.7
0.07	6.81	5.76	6.75	5.71	6.81	5.75	6.81	5.74	18.6

According to the data comparison in Table 4, there is a certain error between the fatigue life of the plate obtained by the theoretical method proposed and the numerical results, with the maximum error being 19.1 %. There are probably three reasons for the large error:

1) the crack theory model proposed in this paper differs from the numerical model, resulting in significant errors in the lifespan of thin plates,
2) the loose coupling analysis method assumes that the stress at the crack tip remains constant during each cycle, but in numerical analysis, the stress at the crack tip varies periodically, resulting in errors in the incremental expansion of the crack during each vibration cycle,
3) in numerical analysis, cracks exhibit alternating breathing behaviour of opening and closing, and meshes on both crack surfaces interfere, which affects the accuracy of fatigue life calculation.

5. Conclusions

In this paper, the loose coupling analysis method is proposed to conduct the vibration fatigue behaviour analysis of the cracked plate, and investigate the influence of the temperature field on the modal, dynamic response, and vibration fatigue life behaviour. The change in the temperature field alters the elastic modulus of the plate and causes additional temperature stress in the plate. Therefore, the influence of the temperature field on the vibration fatigue behaviour of thin plate structures cannot be ignored. Considering the interaction between thermal coupling and crack propagation, the loose coupling analysis method can effectively investigate the vibration fatigue behaviour of the cracked plate. The theoretical method proposed in this article provides a solution for the life estimation of thin plate structures in service, and also provides theoretical possibilities for the health monitoring of thin plate structures in service.

Acknowledgments

This work is supported by the Natural Key R&D Program of China (no. 2022YFC2806605) and the National Natural Science Foundation of China (no. 12402063).

References

1. Berger, H.M. (1955). A new approach to the analysis of large deflections of plates. *Journal of Applied Mechanics*, *22*(4), 465–472. https://doi.org/10.1115/1.4011138

2. Heo, J., Yang, Z., Xia, W., Oterkus, S., & Oterkus, E. (2020). Free vibration analysis of cracked plates using peridynamics. *Ships and Offshore Structures*, *15*(sup1), S220–S229. https://doi.org/10.1080/17445302.2020.1834266
3. Huang, T., Lu, H., McFarland, D.M., Li, W.L., Tan, C.A., Bergman, L.A., & Gong, J. (2018). Natural frequency veering and mode localization caused by straight through–cracks in rectangular plates with elastic boundary conditions. *Acta Mechanica*, *229*(10), 4017-4031. https://doi.org/10.1007/s00707-018-2195-2
4. Ilie, P., & Ince, A. (2022). Three-dimensional fatigue crack growth simulation and fatigue life assessment based on finite element analysis. *Fatigue & Fracture of Engineering Materials & Structures*, *45*(11), 3251–3266. https://doi.org/10.1111/ffe.13815
5. Israr, A. (2008). *Vibration analysis of cracked aluminium plates* (Publication No. glathesis:2008-261) [Doctoral dissertation, University of Glasgow]. Enlighten: Theses. https://theses.gla.ac.uk/261/
6. Jalili, S., & Daneshmehr, A.R. (2018). Statistical analysis of nonlinear response of rectangular cracked plate subjected to chaotic interrogation. *International Journal of Applied Mechanics*, *10*(03), Article 1850033. https://doi.org/10.1142/S1758825118500333
7. Jameel, A., & Harmain, G.A. (2019). Fatigue crack growth analysis of cracked specimens by the coupled finite element-element free Galerkin method. *Mechanics of Advanced Materials and Structures*, *26*(16), 1343–1356. https://doi.org/10.1080/15376494.2018.1432800
8. Moradi, S., Makvandi, H., Poorveis, D., & Shirazi, K.H. (2019). Free vibration analysis of cracked postbuckled plate. *Applied Mathematical Modelling*, *66*, 611–627. https://doi.org/10.1016/j.apm.2018.10.004
9. Motaharifar, F., Ghassabi, M., & Talebitooti, R. (2021). A variational iteration method (VIM) for nonlinear dynamic response of a cracked plate interacting with a fluid media. *Engineering with Computers*, *37*(4), 3299–3318. https://doi.org/10.1007/s00366-020-00998-w
10. Ostiguy, G.L., & Evan-Iwanowski, R.M. (1982). Influence of the aspect ratio on the dynamic stability and nonlinear response of rectangular plates. *Journal of Mechanical Design*, *104*(2), 417–425. https://doi.org/10.1115/1.3256362
11. Rice, J.R., & Levy, N. (1972). The part-through surface crack in an elastic plate. *Journal of Applied Mechanics*, *39*(1), 185–194. https://doi.org/10.1115/1.3422609
12. Shih, Y.-S., & Wu, G.-Y. (2002). Effect of vibration on fatigue crack growth of an edge crack for a rectangular plate. *International Journal of Fatigue*, *24*(5), 557–566. https://doi.org/10.1016/S0142-1123(01)00110-4
13. Song, Y., Xue, K., & Li, Q. (2022). A solution method for free vibration of intact and cracked polygonal thin plates using the Ritz method and Jacobi polynomials. *Journal of Sound and Vibration*, *519*, Article 116578. https://doi.org/10.1016/j.jsv.2021.116578
14. Tazoe, K., Tanaka, H., Oka, M., & Yagawa, G. (2020). Analyses of fatigue crack propagation with smoothed particle hydrodynamics method. *Engineering Fracture Mechanics*, *228*, Article 106819. https://doi.org/10.1016/j.engfracmech.2019.106819
15. Useche, J. (2020). Fracture dynamic analysis of cracked Reissner plates using the boundary element method. *International Journal of Solids and Structures*, *191–192*, 315–332. https://doi.org/10.1016/j.ijsolstr.2020.01.017
16. Xue, J., & Wang, Y. (2019). Free vibration analysis of a flat stiffened plate with side crack through the Ritz method. *Archive of Applied Mechanics*, *89*(10), 2089–2102. https://doi.org/10.1007/s00419-019-01565-6
17. Xue, J., Wang, Y., & Chen, L. (2020). Nonlinear vibration of cracked rectangular Mindlin plate with in-plane preload. *Journal of Sound and Vibration*, *481*, Article 115437. https://doi.org/10.1016/j.jsv.2020.115437
18. Yadzhak, N., Andreykiv, O., & Lapusta, Y. (2022). Modelling small fatigue crack propagation under mixed mode II+III loading. *Procedia Structural Integrity*, *36*, 401–407. https://doi.org/10.1016/j.prostr.2022.01.052

Manuscript received June 20, 2025; accepted for publication November 3, 2025; published online February 10, 2026.

JOURNAL OF THEORETICAL
AND APPLIED MECHANICS
64, 1, pp. 29–44, Warsaw 2026
https://doi.org/10.15632/jtam-pl/214265

RESEARCH ON ADAPTIVE FUZZY SLIDING MODE CONTROL WITH SWITCHING STRATEGY FOR TRAJECTORY TRACKING OF DIGITAL HYDRAULIC CYLINDER

Shouling JIANG[1*], Qi CHEN[2]

[1] *School of Computer, Heze University, Shandong, China*
[2] *Heze University Library, Heze University, Shandong, China*
[*]corresponding author, *jiangshouling@hezeu.edu.cn*

Aiming at the position control system of digital hydraulic cylinders with multiple nonlinear factors and coupled forces, this study proposes a switched fuzzy sliding mode adaptive control strategy (TDAFSMC). This study proposes a TDAFSMC strategy that employs fuzzy logic to approximate switching terms for chattering suppression, while utilizing a tracking differentiator to enhance dynamic response characteristics. Lyapunov theory ensures stability through adaptive weight adjustment. Simulations show 41.7 % faster response and 2.0 % lower error versus PID. With response speed error maintained below 8.0 % and tracking error under 1.0 %, they confirm the feasibility, effectiveness, and superior performance of the proposed control strategy.

Keywords: tracking differentiator; fuzzy control; sliding mode variable structure control; adaptive control; digital hydraulic cylinder.

Articles in JTAM are published under Creative Commons Attribution 4.0 International.
Unported License https://creativecommons.org/licenses/by/4.0/deed.en.
By submitting an article for publication, the authors consent to the grant of the said license.

1. Introduction

Compared with traditional hydraulic transmission systems and electro-hydraulic servo control systems, digital hydraulic cylinders have gained widespread industrial applications due to their structural simplicity, precise control capability, and relatively low cost. However, the inherent nonlinearity, time-varying characteristics, and strong coupling effects of digital hydraulic cylinders have made their precise and stable control a key focus in both academic research and industrial practice (Qi *et al.*, 2024; Zhang *et al.*, 2025; Wang *et al.*, 2019). While conventional PID or single-loop control strategies offer simplicity in implementation, they often fail to meet the requirements for high precision and rapid response when dealing with complex nonlinear systems. Consequently, the development of advanced control strategies to enhance the positioning accuracy and operational stability of digital hydraulic cylinders has emerged as a critical challenge demanding immediate solutions.

Significant research efforts have been made by scholars worldwide to enhance the performance of electro-hydraulic servo position control systems. Gao *et al.* (2023) applied digital hydraulic cylinders to semi-active suspension systems, designing a fuzzy control-based multimode switching control strategy for suspension damping. This control strategy demonstrates enhanced vibration attenuation performance and contributes to improved ride comfort in vehicles. Yu *et al.* (2024) introduced a novel integrated robust control strategy that simultaneously improved system response speed, effectively suppressed system uncertainties, and enhanced high-frequency tracking performance. In addressing the nonlinearities and uncertainties inherent in hydraulic systems, He *et al.* (2023) proposed a hybrid SAC-PID control strategy. This approach employs the soft-actor critic (SAC) algorithm to dynamically adapt control parameters based on real-time system states, thereby enhancing the system's robustness. However, the reinforcement

learning framework necessitates substantial computational resources, while the initial phase of parameter tuning and optimization presents significant complexity. Liu *et al.* (2022a) proposed a self-tuning fuzzy PID positioning controller based on particle swarm optimization (PSO), which optimizes control parameters through real-time adjustment of quantization and scaling factors, thereby significantly improving the system's tracking accuracy. However, the iterative optimization process of the PSO algorithm requires considerable computational effort, which may compromise the real-time control performance. Zhang *et al.* (2024) presented an enhanced beetle antennae search (BAS) algorithm-optimized fuzzy PID controller for improving electromechanical actuator performance. The proposed control scheme demonstrates superior stability across various signal response tests, achieving significant performance enhancement. Guo *et al.* (2022) developed a Kalman-GA-optimized PID controller to improve response time, accuracy, and anti-interference in position control. Results show enhanced performance versus traditional methods, though it requires accurate modeling and lacks online self-tuning. Liu *et al.* (2022b) investigated a variable-domain fuzzy PID static compensation algorithm to address nonlinearities induced by valve dead-zone and friction in electro-hydraulic proportional servo systems. Simulation results demonstrate significant improvement in system response speed, though with relatively modest enhancement in control accuracy.

While the aforementioned control methods have improved system performance to varying degrees, the enhancement in system responsiveness remains relatively limited. To address this challenge, sliding mode variable structure control (SMC) has emerged as a prominent approach for response improvement. Đào *et al.* (2023) proposed a sliding mode controller incorporating PID direct parameter adjustment (SMCPID) for hydraulic cylinder systems. While this control strategy effectively mitigates chattering, the inherent high-frequency switching characteristics of sliding mode control may still induce actuator wear, potentially compromising long-term reliability. Sun *et al.* (2022) addressed the issues of prolonged reaching time to sliding surfaces and high-frequency chattering by proposing an adaptive reaching law-based control method with an auxiliary sub-reaching law. Simulation results on electro-hydraulic position servo systems demonstrate improved robustness, though minor chattering persists. Yang *et al.* (2019) presented an enhanced adaptive sliding mode control scheme for electro-hydraulic position servo systems exhibiting parameter uncertainties and bounded disturbances. The proposed approach employs a saturation function to replace the adjustable signum gain coefficient, effectively mitigating control chattering. Comparative experimental results conclusively demonstrate the scheme's efficacy. Ji *et al.* (2021) proposed a backstepping-based adaptive sliding mode controller for electro-hydraulic systems with parametric uncertainties and random disturbances. While improving system performance, the backstepping approach requires iterative virtual control design and Lyapunov functions, potentially causing "complexity explosion" in high-order systems. Ghani *et al.* (2022) proposed a fuzzy sliding mode method for trajectory tracking in electro-hydrostatic actuators (EHA). Experimental results demonstrate superior effectiveness, though simultaneous tuning of fuzzy membership functions, sliding surface parameters, and switching gains increases implementation complexity. Zhang *et al.* (2022) presented a variable-approaching-law fuzzy sliding mode control (FSMC) strategy to enhance the trajectory tracking performance of omni-directional wheeled robotic mobile platforms. Simulation experiments validate the method's effectiveness in achieving robust dynamic stability. Dang *et al.* (2021) addressed tracking accuracy degradation in hydraulic servo systems caused by nonlinear friction and unstructured uncertainties. An improved adaptive backstepping integral sliding mode control with incomplete differentiation (ID-BIABISMC) is proposed, demonstrating superior tracking precision in comparative experiments.

Li and Cao (2021) proposed a tracking differentiator combined with adaptive nonlinear PID (TD-NPID) to address low synchronization accuracy in multi-cylinder cooperative propulsion control of shield hydraulic systems under heavy load variations, demonstrating effective improvement in system synchronization performance. To achieve precise tracking control of the voice

coil actuator fast steering mirror (VCA-FSM) with large measurement noise, a nonsingular terminal sliding mode (NTSMC) method based on a differentiator (TD) is proposed. Experimental results from the hardware-in-the-loop (HIL) test bench validate the method's effectiveness in meeting both dynamic response and steady-state accuracy requirements (Li *et al.*, 2023).

The aforementioned studies have systematically investigated the performance of electro-hydraulic servo systems through numerical simulations and experimental validations, establishing a solid theoretical foundation. These research efforts reveal that while sliding mode variable structure control effectively enhances system rapidity, increasing switching gains inevitably induces chattering phenomena. To address this limitation, fuzzy control is employed to approximate the switching term, thereby achieving term continuity and significantly mitigating chattering effects. Furthermore, the incorporation of a TD provides comprehensive dynamic characteristics for the controller. Building upon these insights, this paper proposes a novel TD-based switched fuzzy sliding mode adaptive control (TDAFSMC) strategy that synergistically integrates these three control methodologies. The fuzzy adaptive law is rigorously derived through Lyapunov stability theory, with adaptive weight adjustments ensuring both stability and convergence of the entire closed-loop system. For a comprehensive evaluation, MATLAB simulation software is utilized to model and analyze the performance of digital hydraulic cylinder positioning systems under the proposed TDAFSMC strategy. Additionally, an experimental testbed is constructed to empirically validate the control strategy's effectiveness under practical operating conditions.

2. Double-loop digital hydraulic cylinder state space model

The double-loop digital hydraulic cylinder system primarily consists of five key components: a servo motor, coupling mechanism, four-way spool valve, internal indirect feedback mechanism, and a conventional hydraulic cylinder. The internal indirect feedback mechanism comprises a ball screw assembly and spool feedback linkage. The thrust bearing tightly presses the ball screw against the cylinder cover, allowing the screw only one rotational degree of freedom. Both the piston and the screw nut are fixed in position. A threaded piston pair is formed between the screw and piston, while the other end of the screw is threadedly connected to the right end of the spool, forming a threaded spool pair. The right end of the servo motor is connected to the left end of the spool through the coupling. The spool has only one axial degree of freedom relative to the output shaft of the servo motor, forming a sliding spool pair. The schematic diagram of this structural principle is shown in Fig. 1.

The operational principle of the system is as follows: When the command signal is zero, the zero-opening four-way spool valve remains stationary, keeping the hydraulic cylinder piston rod at rest. With a positive command signal, a potential difference is generated to drive the servo motor, causing the spool to move leftward and open the valve port. Under the high-pressure oil, the piston moves leftward while the ball screw rotates circumferentially in the opposite direction to the servo motor. This screw rotation drives the spool rightward to close the valve port until the deviation reaches zero. A negative command signal triggers the reverse process. Thus, the position of the digital hydraulic cylinder changes according to the command signal variations. The structural diagram of this double-loop digital hydraulic cylinder position control system is shown in Fig. 2.

Jiang *et al.* (2022) provided a comprehensive theoretical analysis of the digital hydraulic cylinder's working principle and established an enhanced mathematical model that incorporates the dynamics of both the digital spool valve and feedback mechanism. This advanced model integrates critical nonlinear factors including transmission backlash, spool valve radial leakage, and LuGre friction characteristics, thereby achieving more accurate representation of actual system behavior. Building upon this established theoretical foundation, the present study directly presents the consolidated nonlinear state-space model without redundant elaboration.

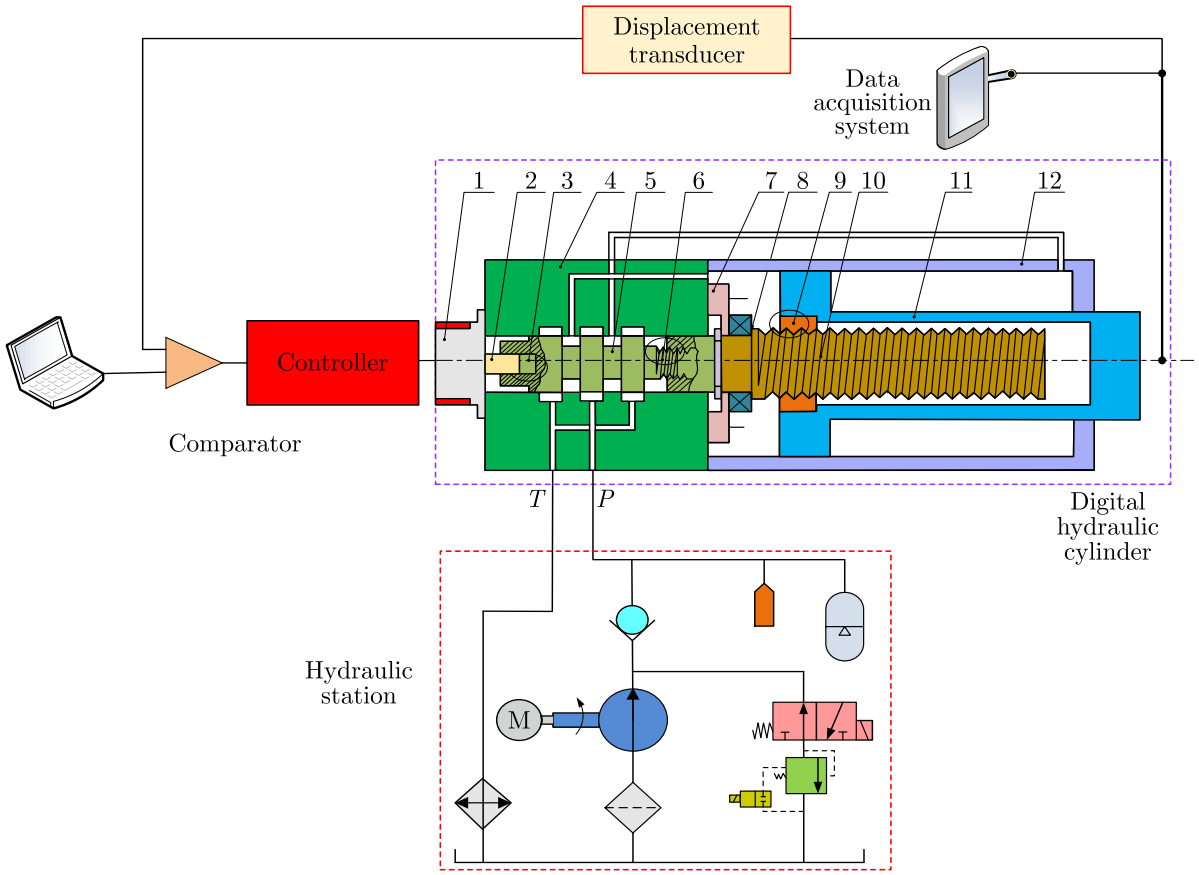

Fig. 1. Working principle diagram of digital hydraulic cylinder: 1 – servo motor; 2 – coupler, 3 – valve spool sliding pair; 4 – valve body; 5 – spool; 6 – spool thread pair; 7 – fixed sleeve; 8 – thrust bearing; 9 – piston thread pair; 10 – ball screw; 11 – piston rod; 12 – cylinder body.

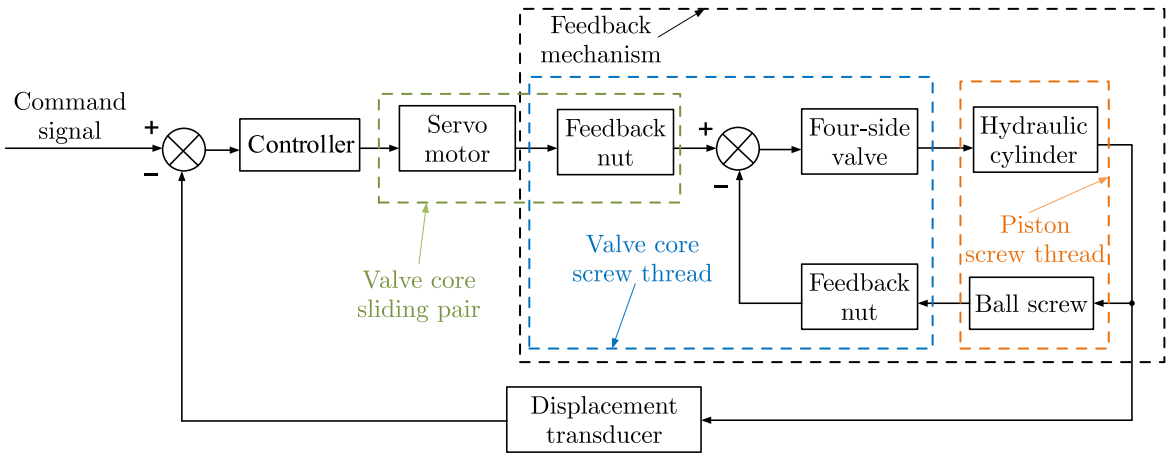

Fig. 2. Double closed-loop digital hydraulic cylinder position control system structure diagram.

The system control input is u_q, the output piston rod displacement is $y = x_1 = x_p$, the system state variable is x:

$$x = [x_1,\ x_2,\ x_3,\ x_4,\ x_5,\ x_6,\ x_7,\ x_8,\ x_9,\ x_{10},\ x_{11},\ x_{12},\ x_{13},\ x_{14}]^{\mathrm{T}}$$
$$= \left[x_p,\ \dot{x}_p,\ P_1,\ P_2,\ x_v,\ \dot{x}_v,\ \theta_s,\ \dot{\theta}_s,\ \theta_v,\ \dot{\theta}_v,\ \theta_\tau,\ \dot{\theta}_\tau,\ z, i_q\right]^{\mathrm{T}}. \tag{2.1}$$

Therefore, the state equation of the system can be expressed as

$$\begin{cases} \dot{x}_1 = x_2, \\ \dot{x}_2 = \left[\begin{array}{c} A_1 \left(x_3 - m x_4\right) - F_{np} \cos \alpha_p - F_{tp} \sin \alpha_p - \left(k_1 x_1 + k_3 x_1^3\right) \\ - \sigma_0 x_{13} + \sigma_1 \dfrac{\left|x_2\right|}{g\left(x_2\right)} x_{14} + \left(\sigma_2 - \sigma_1\right) x_2 \end{array} \right] \Big/ M_t + w_1, \\ \dot{x}_3 = \left[Q_1 - A_1 x_2\right] \beta_e / \left(V_{01} + A_1 x_1\right) + w_2, \\ \dot{x}_4 = \left[-Q_2 - A_2 x_2\right] \beta_e / \left(V_{02} - A_2 x_1\right) + w_3, \\ \dot{x}_5 = x_6, \\ \dot{x}_6 = \left[F_{nv} \cos \alpha_v - F_{tv} \sin \alpha_v - F_{yd} - B_{vp} x_6 - F_{tg} - F_{fv}\right] / m_v, \\ \dot{x}_7 = x_8, \\ \dot{x}_8 = \left[r_{vs} F_{nv} \sin \alpha_v + r_{vs} F_{tv} \cos \alpha_v + r_{ps} F_{np} \sin \alpha_p - r_{ps} F_{tp} \cos \alpha_p - T_{fs} - B_s x_8\right] / J_s, \\ \dot{x}_9 = x_{10}, \\ \dot{x}_{10} = \left[\mathrm{r}_\tau F_{ng} - r_s F_{nv} \sin \alpha_v - r_s F_{tv} \cos \alpha_v - B_{vz} x_{10} - T_{fv}\right] / J_v, \\ \dot{x}_{11} = x_{12}, \\ \dot{x}_{12} = \left[k_t x_{14} - B_2 x_{12} - r_\tau F_{ng}\right] / J, \\ \dot{x}_{13} = x_2 - \sigma_0 \dfrac{\left|\dot{x}_2\right|}{F_c + \left(F_{sc} - F_c\right) e^{-\left(x_2 / v_{sk}\right)^2}} x_{13}, \\ \dot{x}_{14} = \left[u_q - R x_{14} - k_e x_{12}\right] / L_0, \end{cases} \tag{2.2}$$

where

$$w_1 = -F_L / M_t, \quad w_2 = \frac{\left[-C_0 x_3 - C_1 \left(x_3 - x_4\right)\right] \beta_e}{V_{01} + A_1 x_1}, \quad w_3 = \frac{\left[-C_0 x_4 + C_1 \left(x_3 - x_4\right)\right] \beta_e}{V_{02} - A_2 x_1}.$$

Let us consider the hydraulic cylinder load force and leakage as disturbances in the system, namely

$$\begin{cases} w_2 \le \dfrac{\beta_e P_s \left(C_1 + C_0\right)}{\left|V_1\right|_{\min}}, \\ w_3 \le \dfrac{\beta_e P_s \left(C_1 + C_0\right)}{\left|V_2\right|_{\min}}. \end{cases} \tag{2.3}$$

Therefore, the disturbances w_1, w_2, and w_3 are bounded:

$$w = \left[\begin{array}{cccccccc} 0 & w_1 & w_2 & w_3 & 0 & \ldots & 0 \end{array} \right]_{1 \times 14}. \tag{2.4}$$

And the system state space expression is

$$\begin{cases} \dot{x} = f(x) + g(x) u + p(x) w, \\ z = h(x) x. \end{cases} \tag{2.5}$$

In formula (2.5):

$$
f(x)=\begin{cases}
\dot{x}_1 = x_2, \\
\dot{x}_2 = \left[\begin{array}{r} A_1\left(x_3 - m x_4\right) - F_{np}\cos\alpha_p - F_{tp}\sin\alpha_p - \left(k_1 x_1 + k_3 x_1^3\right) \\ - \sigma_0 x_{13} + \sigma_1 \dfrac{|x_2|}{g\left(x_2\right)} x_{14} + \left(\sigma_2 - \sigma_1\right) x_2 \end{array}\right] \Big/ M_t, \\
\dot{x}_3 = \left[Q_1 - A_1 x_2\right] \beta_e / (V_{01} + A_1 x_1), \\
\dot{x}_4 = \left[-Q_2 - A_2 x_2\right] \beta_e / (V_{02} - A_2 x_1), \\
\dot{x}_5 = x_6, \\
\dot{x}_6 = \left[F_{nv}\cos\alpha_v - F_{tv}\sin\alpha_v - F_{yd} - B_{vp} x_6 - F_{tg} - F_{fv}\right] / m_v, \\
\dot{x}_7 = x_8, \\
\dot{x}_8 = \left[\begin{array}{r} r_{vs} F_{nv}\sin\alpha_v + r_{vs} F_{tv}\cos\alpha_v + r_{ps} F_{np}\sin\alpha_p \\ - r_{ps} F_{tp}\cos\alpha_p - T_{fs} - B_s x_8 \end{array}\right] \Big/ J_s, \\
\dot{x}_9 = x_{10}, \\
\dot{x}_{10} = \left[\mathrm{r}_\tau F_{ng} - r_s F_{nv}\sin\alpha_v - r_s F_{tv}\cos\alpha_v - B_{vz} x_{10} - T_{fv}\right] / J_v, \\
\dot{x}_{11} = x_{12}, \\
\dot{x}_{12} = \left[k_t x_{14} - B_2 x_{12} - r_\tau F_{ng}\right] / J, \\
\dot{x}_{13} = x_2 - \sigma_0 \dfrac{|\dot{x}_2|}{F_c + \left(F_{sc} - F_c\right) e^{-\left(x_2 / v_{sk}\right)^2}} x_{13}, \\
\dot{x}_{14} = \left[-R x_{14} - k_e x_{12}\right] / L_0,
\end{cases}
\tag{2.6}
$$

$$
\begin{cases}
g(x) = \left[\begin{array}{cccccc} 0 & \ldots & 0 & 0 & 1 \end{array}\right]^{\mathrm{T}}_{1\times 14}, \\
p(x) = \left[\begin{array}{cccccc} 0 & 1 & 1 & 1 & 0 & \ldots & 0 \end{array}\right]^{\mathrm{T}}_{1\times 14}, \\
h(x) = \left[\begin{array}{cccccc} 1 & 0 & 0 & \ldots & 0 \end{array}\right]_{1\times 14}.
\end{cases}
\tag{2.7}
$$

3. Design of the TDAFSMC controller

TD is essentially a signal processing technique that filters the input signal and extracts its derivative. Particularly when the input signal undergoes abrupt changes, the TD can provide a smooth input signal for the controller. Meanwhile, its filtering capability mitigates the impact of sudden signal variations, preventing system overshoot. This effectively resolves the inherent conflict between "rapid response" and "overshoot", thereby enhancing system stability. The TD can achieve the dynamic performance metrics of closed-loop systems, ensuring high-quality real-time tracking curves for the system.

In this study, the digital hydraulic cylinder is modeled as a second-order system. For continuously differentiable input signals, a conventional second-order TD in cascade configuration would

suffice. However, when the input signal is a step function, its derivative theoretically approaches infinity. To address this fundamental limitation, a third-order TD is proposed in this work.

The third-order TD formulation constructed using the inverse hyperbolic sine function *arsh* is presented as follows:

$$\begin{cases} \dot{v}_1 = v_2, \\ \dot{v}_2 = v_3, \\ \dot{v}_3 = R^3 \left\{ -a_1 \mathrm{arsh}\left[b_1\left(v_1(t) - r(t)\right)\right] - a_2 \mathrm{arsh}\left[b_2 v_2(t)/R\right] - a_3 \mathrm{arsh}\left[b_3 v_3(t)/R^2\right] \right\}. \end{cases} \tag{3.1}$$

In formula (3.1), $r(t)$ represents the input signal, and all parameters are positive constants.

For any bounded integrable input signal $r(t)$, given a sufficiently large parameter R, the solution of Eq. (3.1) can asymptotically converge to $r(t)$ within arbitrary finite time, yielding outputs $v_2(t) = \dot{r}(t)$ and $v_3(t) = \ddot{r}(t)$. The proposed TD demonstrates superior differential tracking capability while effectively suppressing derivative noise amplification, making it widely applicable in engineering implementations.

To enhance the system's rapid response capability, this paper employs sliding mode variable structure control. However, increasing the switching gain may induce chattering phenomena. To address this issue, fuzzy control is adopted to approximate the switching term, thereby achieving term continuity and effectively mitigating chattering. Below we present the design of a fuzzy sliding mode adaptive controller.

The switching function is formally defined as follows:

$$s(x,t) = k_1 e + k_2 \dot{e} + ... + k_{n-1} e^{(n-1)} + e^{(n-1)} = ke, \tag{3.2}$$

where the matrices $e = x - x_d = \left(e, \dot{e}, ..., e^{(n-1)}\right)^{\mathrm{T}}$ and $k_1, k_2, ..., k_{n-1}$ satisfy the Hurwitz polynomial condition.

The sliding mode control law is designed as follows:

$$u(t) = \frac{1}{g(x,t)} \left(-f(x,t) - \sum_{i=1}^{n-1} k_i e^{(i)} + x_d^{(n)} - u_{sw} \right). \tag{3.3}$$

In formula (3.3), $u_{sw} = \eta \,\mathrm{sgn}\,(s)$, $\eta \geq D$. Thus:

$$\begin{aligned} \dot{s}(x,t) &= \sum_{i=1}^{n-1} k_i e^{(i)} + e^{(n)} = \sum_{i=1}^{n-1} k_i e^{(i)} + x^{(n)} - x_d^{(n)} \\ &= \sum_{i=1}^{n-1} k_i e^{(i)} + f(x,t) + g(x,t)u(t) + d(t) - x_d^{(n)}. \end{aligned} \tag{3.4}$$

Substituting formula (2.5) and formula (3.3) yields:

$$s(x,t) \cdot \dot{s}(x,t) = ds - \eta \left| s \right| \leq 0. \tag{3.5}$$

When the upper bounds of f, g, and d are unknown, the control law (3.3) becomes inapplicable. To address this limitation, fuzzy systems $\widehat{f}$, $\widehat{g}$, and $\widehat{h}$ are employed to approximate f, g, and $\eta \,\mathrm{sgn}\,(s)$, respectively.

The fuzzy systems are constructed using a product inference engine, singleton fuzzifier, and center-average de-fuzzifier, with their respective outputs designated as $\widehat{f}$, $\widehat{g}$, and $\widehat{h}$, whereby the control law is consequently modified to:

$$u(t) = \frac{1}{\widehat{g}(x,t)} \left(-\widehat{f}(x,t) - \sum_{i=1}^{n-1} k_i e^{(i)} + x_d^{(n)} - \widehat{h}(s) \right), \tag{3.6}$$

$$\begin{cases} \widehat{f}\left(x|\,\theta_f\right) = \theta_f^T \xi(x), \\ \widehat{g}\left(x|\,\theta_g\right) = \theta_g^T \xi(x), \\ \widehat{h}\left(s|\,\theta_h\right) = \theta_h^T \phi(s), \end{cases} \tag{3.7}$$

where $\widehat{f}\left(x|\,\theta_f\right)$, $\widehat{g}\left(x|\,\theta_g\right)$, and $\widehat{h}\left(s|\,\theta_h\right)$ denote the outputs of the fuzzy systems, $\xi(x)$ and $\phi(s)$ represent fuzzy vectors, while θ_f^T, θ_g^T, and θ_h^T are dynamically adjusted according to the adaptive laws;

$$\widehat{h}\left(x|\,\theta_h^*\right) = \eta_\Delta \operatorname{sgn}(s), \tag{3.8}$$

$$\eta_\Delta = D + \eta \qquad \eta \geq 0, \tag{3.9}$$

$$|d| \leq D. \tag{3.10}$$

The adaptive laws are designed as follows:

$$\begin{cases} \dot{\theta}_f = r_1 s \xi(x), \\ \dot{\theta}_g = r_2 s \xi(x) u, \\ \dot{\theta}_h = r_3 s \phi(s). \end{cases} \tag{3.11}$$

Subsequently, the convergence proof of the controller is established, where the optimal parameters are defined as

$$\theta_f^* = \arg \min_{\theta_f \in \Omega_f} \left[\sup \left| \widehat{f}\left(x| \underset{x \in R^n}{\theta_f} \right) - f(x,t) \right| \right], \tag{3.12}$$

$$\theta_g^* = \arg \min_{\theta_g \in \Omega_g} \left[\sup \left| \widehat{g}\left(x| \underset{x \in R^n}{\theta_g} \right) - g(x,t) \right| \right], \tag{3.13}$$

$$\theta_h^* = \arg \min_{\theta_h \in \Omega_h} \left[\sup \left| \widehat{h}\left(s| \underset{x \in R^n}{\theta_h} \right) - u_{sw} \right| \right], \tag{3.14}$$

where Ω_f, Ω_g, and Ω_h denote the sets of θ_f, θ_g, and θ_h, respectively.

The minimum approximation error is defined as

$$\omega = f(x,t) - \widehat{f}\left(x|\,\theta_f^*\right) + \left(g(x,t) - \widehat{g}\left(x|\,\theta_g^*\right)\right) u, \tag{3.15}$$

where $|\omega| \leq \omega_{\max}$.

Substituting the control law (3.6) yields:

$$\begin{aligned} \dot{s}(x,t) &= \sum_{i=1}^{n-1} k_i e^{(i)} + x^{(n)} - x_d^{(n)} \\ &= \sum_{i=1}^{n-1} k_i e^{(i)} + f(x,t) + g(x,t)u(t) + d(t) - x_d^{(n)} \\ &= \sum_{i=1}^{n-1} k_i e^{(i)} + f(x,t) + \widehat{g}(x,t)u(t) + \left(g(x,t) - \widehat{g}(x,t)\right) u + d(t) - x_d^{(n)} \\ &= f(x,t) - \widehat{f}(x,t) - \widehat{h}\left(s|\,\theta_h\right) + \left(g(x,t) - \widehat{g}(x,t)\right) u + d(t) \\ &= \widehat{f}\left(x|\,\theta_f^*\right) - \widehat{f}(x,t) - \widehat{h}\left(s|\,\theta_h\right) + \left(\widehat{g}\left(x|\,\theta_g^*\right) - \widehat{g}(x,t)\right) u + d(t) + \omega - \widehat{h}\left(s|\,\theta_h^*\right) \\ &= \varphi_f^T \xi(x) + \varphi_g^T \xi\left(x\right) u(t) + \varphi_h^T \phi(s) + d\left(t\right) + \omega - \widehat{h}\left(s|\,\theta_h^*\right), \end{aligned} \tag{3.16}$$

where $\varphi_f = \theta_f^* - \theta_f$, $\varphi_g = \theta_g^* - \theta_g$, $\varphi_h = \theta_h^* - \theta_h$.

The Lyapunov function candidate is defined as

$$V = \frac{1}{2}\left(s^2 + \frac{1}{r_1}\varphi_f^T\varphi_f + \frac{1}{r_2}\varphi_g^T\varphi_g + \frac{1}{r_3}\varphi_h^T\varphi_h\right), \tag{3.17}$$

where r_1, r_2, and r_3 are positive constants. Therefore:

$$\begin{aligned}
\dot{V} &= s\dot{s} + \frac{1}{r_1}\varphi_f^T\dot{\varphi}_f\frac{1}{r_2}\varphi_g^T\dot{\varphi}_g + \frac{1}{r_3}\varphi_h^T\dot{\varphi}_h \\
&= s\left(\varphi_f^T\xi(x) + \varphi_g^T\xi(x)u(t) + \varphi_h^T\phi(s) + d(t) + \omega - \widehat{h}\left(s|\,\theta_h^*\right)\right) \\
&\quad + \frac{1}{r_1}\varphi_f^T\dot{\varphi}_f + \frac{1}{r_2}\varphi_g^T\dot{\varphi}_g + \frac{1}{r_3}\varphi_h^T\dot{\varphi}_h \\
&= s\varphi_f^T\xi(x) + \frac{1}{r_1}\varphi_f^T\dot{\varphi}_f + s\varphi_g^T\xi(x)u(t) + \frac{1}{r_2}\varphi_g^T\dot{\varphi}_g + s\varphi_h^T\phi(s) \\
&\quad + \frac{1}{r_3}\varphi_h^T\dot{\varphi}_h + s\left(d(t) - \widehat{h}\left(s|\,\theta_h^*\right)\right) + s\omega.
\end{aligned} \tag{3.18}$$

Given $\widehat{h}\left(s|\,\theta_h^*\right) = \eta_\Delta \mathrm{sgn}\left(s\right)$, it follows that:

$$\begin{aligned}
\dot{V} &= \frac{1}{r_1}\varphi_f^T\left(r_1 s\xi(x) + \dot{\varphi}_f\right) + \frac{1}{r_2}\varphi_g^T\left(r_2 s\xi(x)u(t) + \dot{\varphi}_g\right) \\
&\quad + \frac{1}{r_3}\varphi_h^T\left(r_3 s\varphi(s) + \dot{\varphi}_h\right) + sd(t) + s\omega - (D+\eta)\,|s| \\
&= sd(t) + s\omega - (D+\eta)\,|s|\,,
\end{aligned} \tag{3.19}$$

where $\dot{\varphi}_f = -\dot{\theta}_f$, $\dot{\varphi}_g = -\dot{\theta}_g$, $\dot{\varphi}_h = -\dot{\theta}_h$.

Substituting the adaptive law (3.11) into the preceding equation yields:

$$\dot{V} \le s\omega - \eta\,|s|\,. \tag{3.20}$$

Based on fuzzy approximation theory, the adaptive fuzzy system can achieve an arbitrarily small approximation error ω. Consequently, by selecting a sufficiently large parameter η, the stability condition $\dot{V} \le 0$ can be guaranteed.

When $\dot{V} \equiv 0$ holds and $s \equiv 0$ is satisfied, then according to LaSalle's invariance principle, $t \to \infty$ implies $s \to 0$.

4. Simulation studies

This paper conducts simulation analysis of the proposed adaptive robust control strategy in MATLAB/Simulink environment. The hydraulic system's mathematical model is implemented using S-function based on formula (2.4), while the nonlinear controller is constructed according to formula (3.6). Simultaneously, online estimation of uncertain system parameters is achieved through formula (3.8). The complete control system architecture is illustrated in Fig. 3, where the structural parameters of the digital hydraulic cylinder follow Table 1 in (Jiang *et al.*, 2022).

To verify the control performance of the proposed TDAFSMC strategy, comprehensive tracking tests were conducted using step, sinusoidal, and composite (ramp-step hybrid) reference signals to analyze the system's tracking performance under different control strategies, where the PID controller parameters were set as $k_p = 10\,000$, $k_i = 600$, $k_d = 1000$, with a filter coefficient $N = 1000$. The TDAFSMC controller parameters were set as $r_1 = 50$, $r_2 = 1$, $r_3 = 10$, $k_1 = 35$, $\theta_f^T = 0.1$, $\theta_g^T = 0.1$, and $\theta_h^T = 0.1$, with five Gaussian membership functions employed for

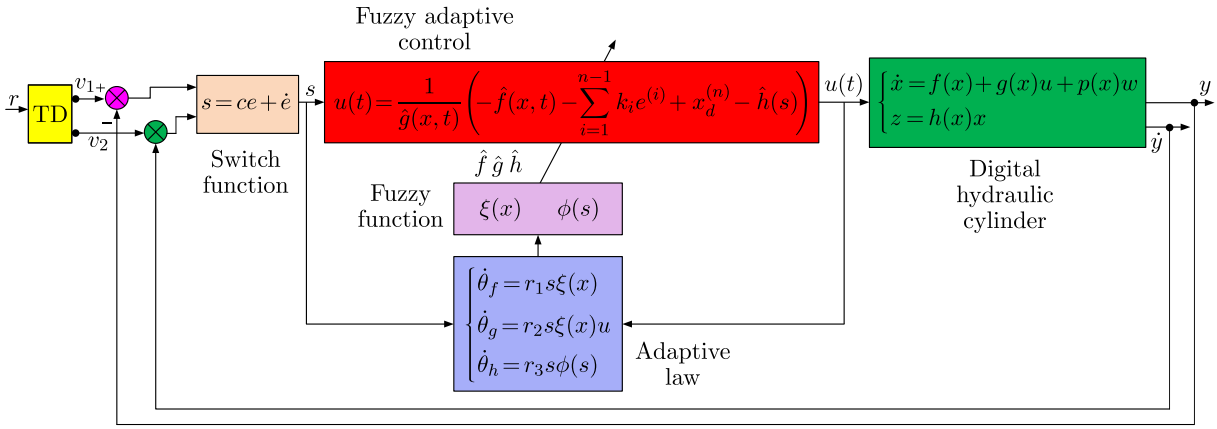

Fig. 3. Structure diagram of the digital hydraulic cylinder position control system based on TDAFSMC.

fuzzification: $\mu_{NM}(x_i) = \exp[-((x_i + \pi/6)/(\pi/24))^2]$, $\mu_{NS}(x_i) = \exp[-((x_i + \pi/12)/(\pi/24))^2]$, $\mu_Z(x_i) = \exp[-(x_i/(\pi/24))^2]$, $\mu_{PS}(x_i) = \exp[-((x_i - \pi/12)/(\pi/24))^2]$, $\mu_{PM}(x_i) = \exp[-((x_i - \pi/6)/(\pi/24))^2]$, resulting in 25 fuzzy rules each for approximating f and g. The switching function $s(t)$ utilized sigmoidal membership functions defined as $\mu_N(s) = 1/[1 + \exp(5(s + 3)]$, $\mu_Z(s) = \exp(-s^2)$ and $\mu_P(s) = 1/[1 + \exp(5(s - 3)])$.

As shown in Fig. 4, the system's positional displacement and tracking error curves are presented for a step reference signal with a 40 mm final magnitude initiated at $t = 1$ s.

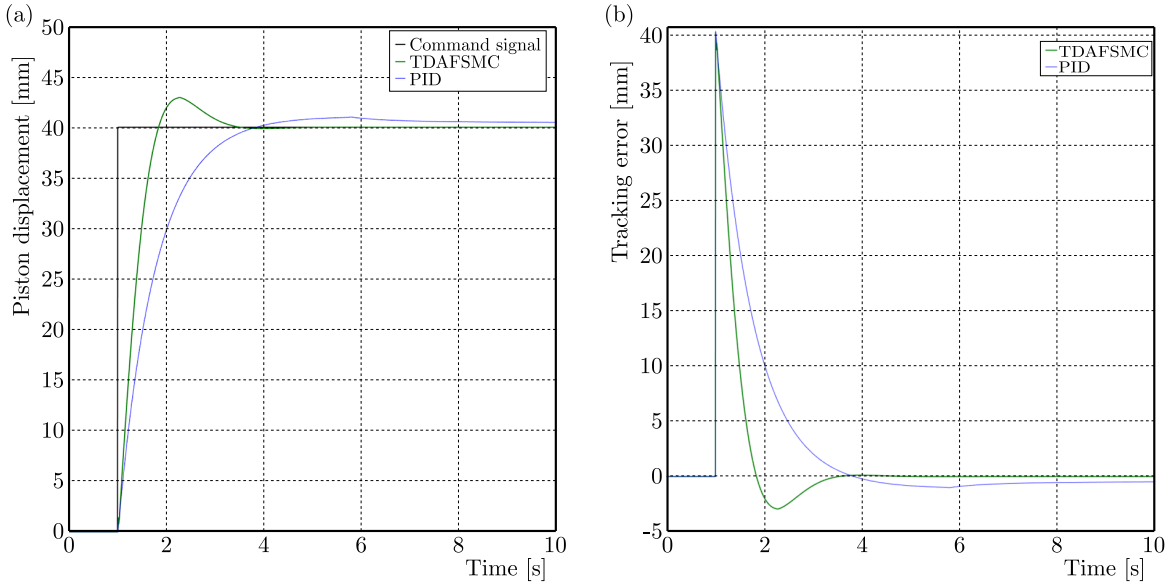

Fig. 4. Piston displacement and error curves: (a) piston displacement curve; (b) tracking error curves.

As evidenced by Fig. 4a, the PID-controlled system achieves the steady state at approximately 6 s with a residual error of 0.8 mm, whereas the proposed TDAFSMC strategy reaches the steady state in 3.5 s with near-zero error, demonstrating a 41.7 % improvement in response speed and 2.0 % enhancement in steady-state accuracy. Comparative analysis reveals that conventional PID control exhibits significant tracking errors and sluggish dynamics under nonlinear coupling forces, while the developed TDAFSMC method simultaneously achieves superior precision and faster transient response.

Figure 5 presents the system's positional tracking performance and corresponding error curves when subjected to a sinusoidal reference trajectory of $20\sin(t)$ mm, thereby demonstrating the controller's ability to manage periodic excitations.

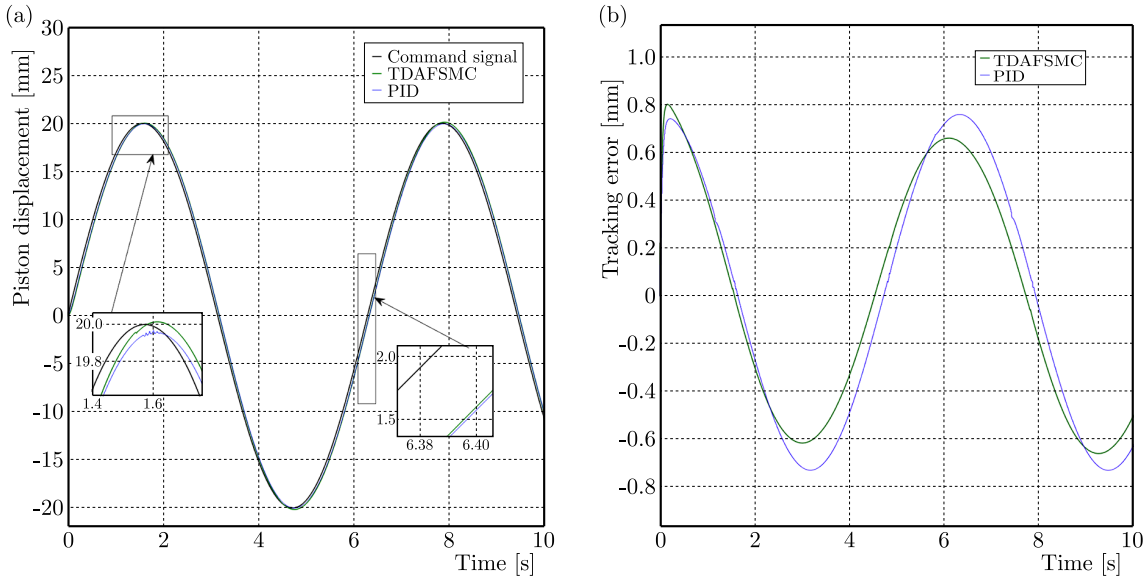

Fig. 5. Piston displacement and error curves: (a) piston displacement curve; (b) tracking error curves.

As demonstrated in Fig. 5, the tracking error under conventional PID control is confined to −0.75 mm–0.8 mm, whereas the proposed TDAFSMC strategy reduces this range to −0.6 mm–0.75 mm, achieving a measurable improvement in tracking precision. The magnified view in Fig. 5a reveals a phase lag of approximately 0.22 s for PID control throughout the simulation cycle, compared to 0.5 s for TDAFSMC. These results indicate that while traditional PID control struggles to compensate for nonlinearities such as backlash effects, the developed TDAFSMC controller effectively incorporates the digital hydraulic cylinder's nonlinear characteristics through a composite sliding-mode and fuzzy control architecture. This adaptive mechanism actively compensates for nonlinear disturbances within the control law, thereby significantly enhancing the hydraulic system's tracking performance.

The given composite signal period is 6 s, the displacement of 0 s–1 s is 0, 1 s–2 s stretches out at a slope of 40 mm/s, 2 s–4 s remains unchanged, 4 s–5 s retracts at a slope of −40 mm/s, and 5 s–6 s remains unchanged.

Figure 6 demonstrates the piston displacement curves and tracking error curves under both PID and TDAFSMC control strategies when following the custom reference signal. During the

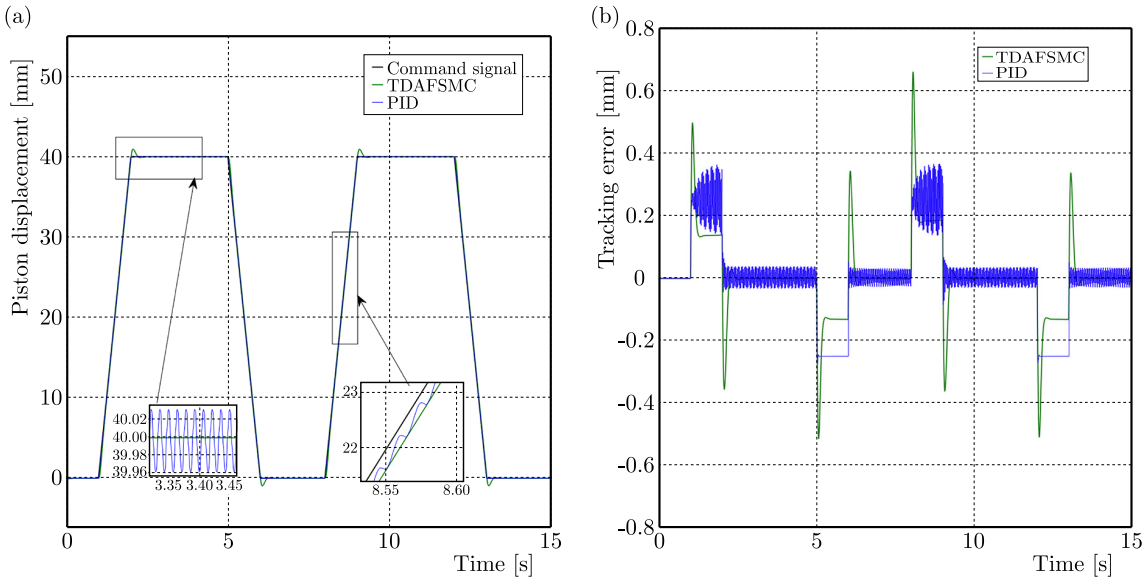

Fig. 6. Piston displacement and error curves: (a) piston displacement curve; (b) tracking error curves.

1 s–2 s period when the hydraulic cylinder piston transitions from rest to forward motion, both control methods exhibit transient errors, with TDAFSMC showing slightly larger initial errors compared to PID. However, during steady-state operation, the PID-controlled system displays sustained oscillations with approximately 0.35 mm error amplitude, which are attributed to system nonlinearities, including backlash, nonlinear friction, and other unmodeled dynamics. Prolonged exposure to these oscillations may lead to increased energy consumption, reduced operational stability, degraded precision, and potential equipment damage. In contrast, the TDAFSMC-controlled system maintains stable operation with only 0.16 mm steady-state error. During the 2 s–4 s interval, the PID-controlled system exhibits distinct limit cycle oscillations with sustained tracking errors averaging approximately 0.05 mm, while TDAFSMC achieves essentially zero error. When the piston reverses direction during 4 s–5 s, the PID-controlled system demonstrates 0.22 mm steady-state error compared to TDAFSMC's 0.15 mm. Overall, TDAFSMC improves tracking precision by 0.98 % across the complete operational cycle. These results confirm that the proposed TDAFSMC control strategy effectively enhances system stability, improves control accuracy, and significantly boosts the tracking performance of hydraulic systems by better compensating for nonlinear effects.

5. Experimental studies

To validate the controller's effectiveness and verify the simulation results, an experimental testbed for digital hydraulic cylinder position control was established, as illustrated in Fig. 7. Subsequent experiments were conducted to evaluate the system's response characteristics under various input signals. The main parameters of the digital hydraulic cylinder test platform are as follows: the variable vane oil pump of model VD1-30F-A3 has a displacement of 12 ml/r–40 ml/r, the motor of model CNS-2934/2.2 KW has a rotational speed of 1420 r/min, the control voltage of the West DAQ-Controller is ±10 V; and the MATLAB USB2.0 high data acquisition card has a rate of 38 Mb/s.

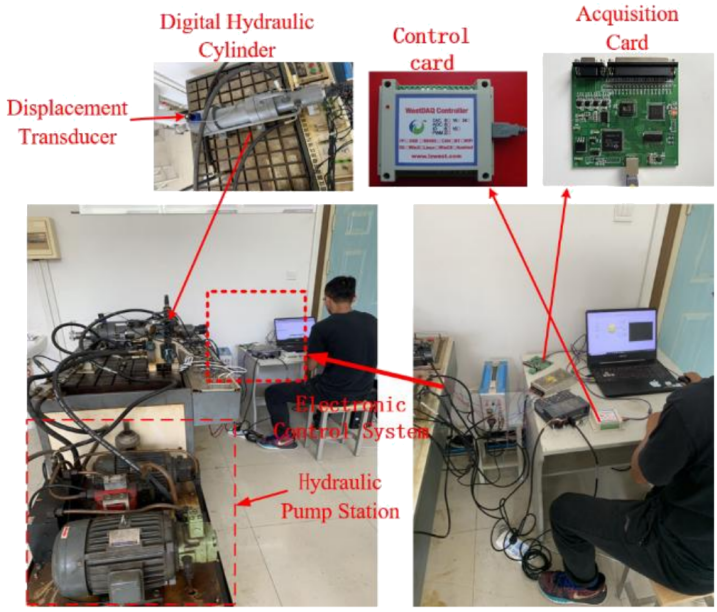

Fig. 7. Digital hydraulic cylinder position control system.

The digital hydraulic cylinder was operated under no-load conditions, with the relief valve in the hydraulic station functioning as a safety valve. The controller received the target displacement commands for piston rod 5 from the host computer 1. A wire-type displacement sensor acquired real-time position and velocity data during operation, which was transmitted

via a data acquisition card to provide feedback to the controller. Through the implemented control algorithm, the system achieved precise position control of the digital hydraulic cylinder.

To validate the control performance of the TDAMSFC strategy under real-world conditions, tracking experiments were conducted using the aforementioned three control signals. For step reference commands, Fig. 8 compares the tracking responses and errors under the different control strategies.

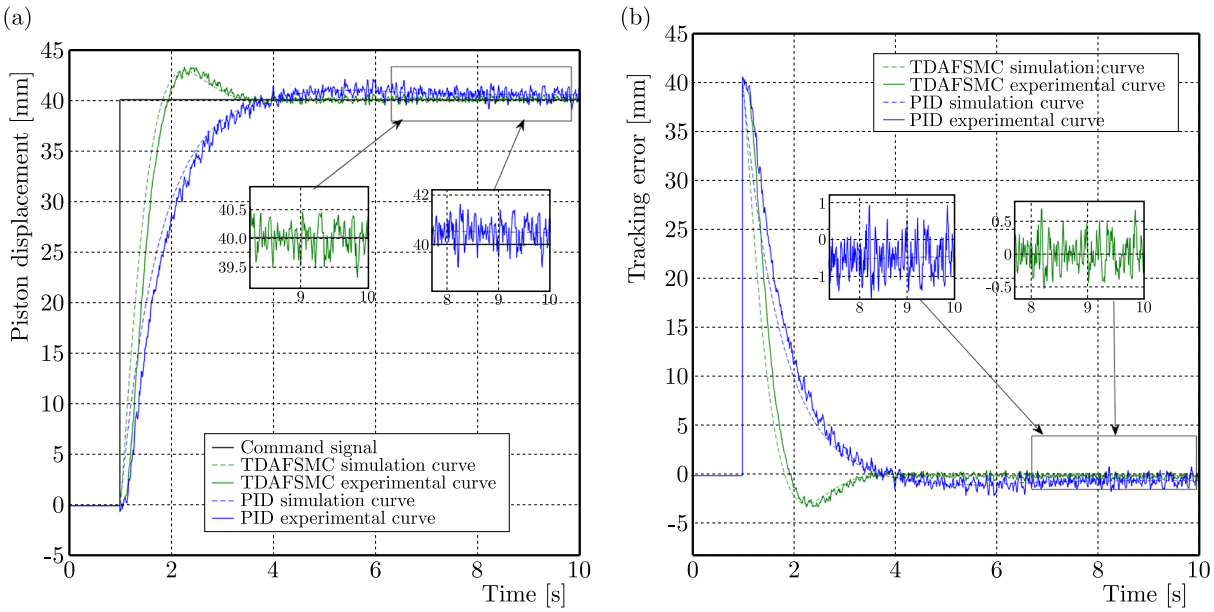

Fig. 8. Piston displacement and error curves: (a) piston displacement curve; (b) tracking error curves.

When reaching the target displacement, the PID-controlled system required approximately 6.5 s to stabilize, with ±1 mm deviation between the experimental and simulated trajectories. In contrast, the TDAMSFC-controlled system achieved stabilization in 3.3 s with only ±0.5 mm error, demonstrating a 49.2 % improvement in response speed and a 2.5 % enhancement in tracking accuracy. These experimental results confirm the superior transient performance and precision of the proposed TDAMSFC strategy, thereby verifying the theoretical analysis and simulation findings presented in this work.

Figure 9 presents the tracking responses and corresponding error profiles under sinusoidal reference commands for different control strategies. When tracking the target displacement, the PID-controlled system exhibits approximately 3 mm experimental error with a 2.1 mm deviation between the experimental and simulated trajectories, whereas the TDAMSFC-controlled system demonstrates superior performance with only 2 mm experimental error and 0.8 mm deviation between the experimental and simulated trajectories, representing a 3.25 % improvement in tracking accuracy. The magnified view in Fig. 9a further reveals that the TDAMSFC strategy significantly reduces the phase lag compared to PID control. These results confirm the enhanced tracking precision of the proposed TDAMSFC approach, providing additional validation for the theoretical and simulation analyses.

Figure 10 presents the tracking responses and corresponding error profiles under composite reference commands for different control strategies. When reaching the target displacement, the PID-controlled system requires approximately 3.0 s to stabilize with a 1.6 mm deviation between experimental and simulated trajectories, whereas the TDAMSFC-controlled system achieves stabilization in 2.6 s with only 1.4 mm deviation, demonstrating a 13.3 % improvement in response speed and a 0.5 % enhancement in tracking accuracy. These experimental results further validate that the proposed TDAMSFC strategy effectively improves control precision in practical applications.

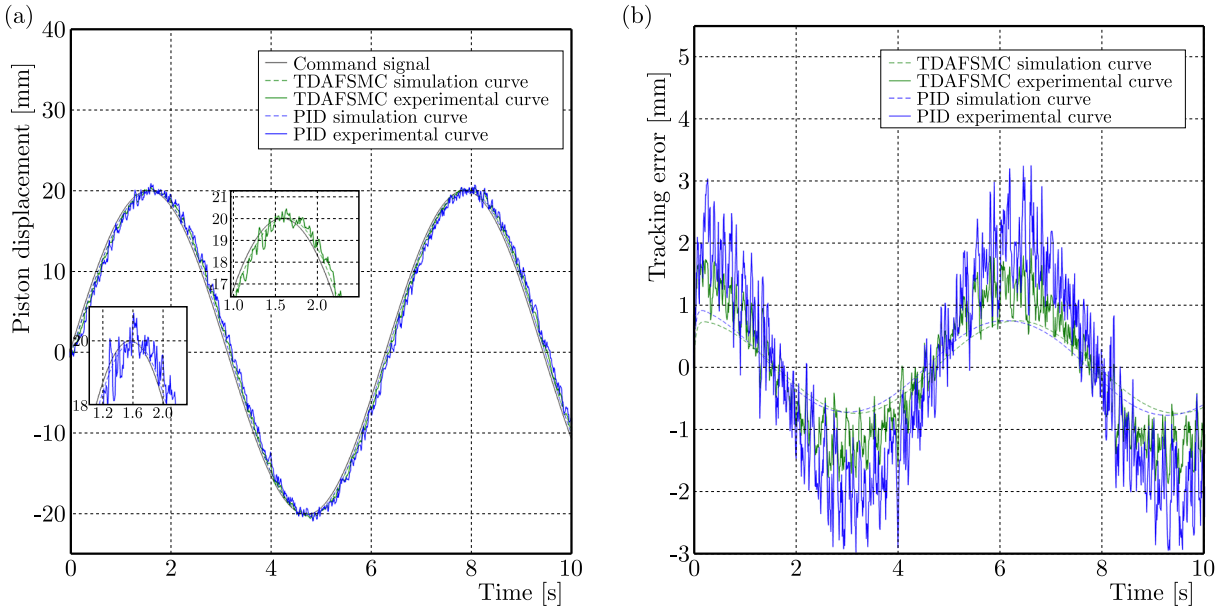

Fig. 9. Piston displacement and error curves: (a) piston displacement curve; (b) tracking error curves.

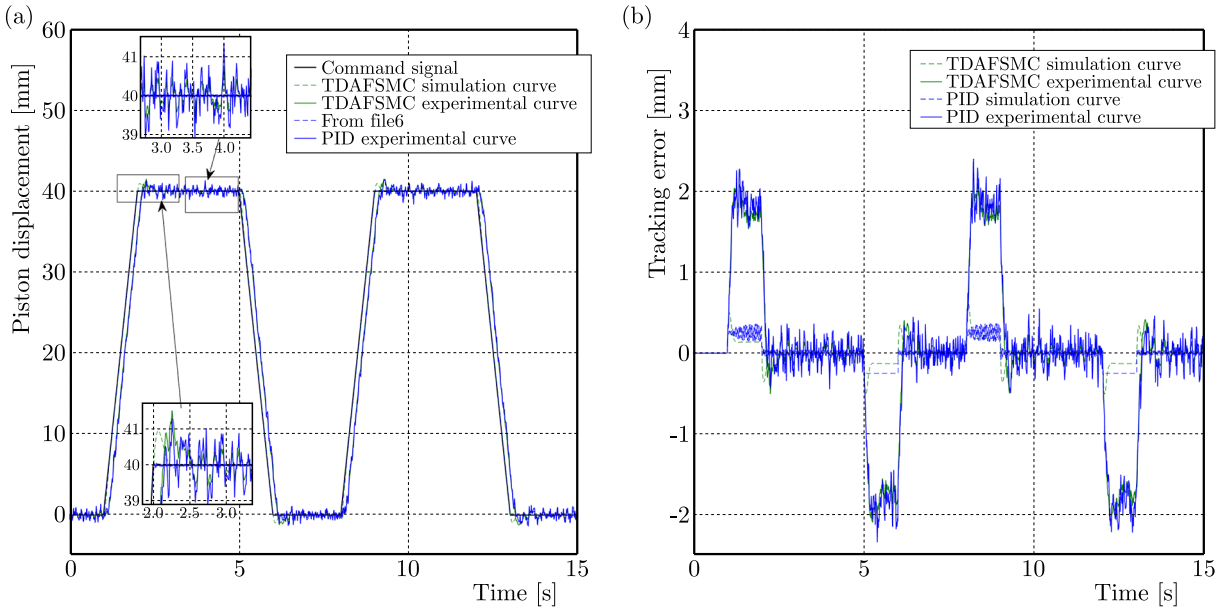

Fig. 10. Piston displacement and error curves: (a) piston displacement curve; (b) tracking error curves.

6. Conclusion

This study investigates output displacement tracking control for a digital hydraulic cylinder system characterized by nonlinear couplings such as clearance, hydrodynamic forces, and friction. By incorporating a TD, precise extraction of both the input signal and its differential information was achieved, significantly enhancing the perception of system dynamic characteristics. The TDAFSMC strategy was adopted, which utilizes a fuzzy system to approximate the switching term in sliding mode control, thereby ensuring controller continuity and effectively mitigating chattering. The stability and convergence of the closed-loop system were guaranteed via adaptive laws derived from Lyapunov theory.

A simulation model of the digital hydraulic cylinder position control system was constructed in the MATLAB/Simulink environment, and tests were conducted under various working con-

ditions, including step, sine, and composite signals. Simulation results demonstrate that under step response, the TDAFSMC strategy improved response speed by 41.7 % and reduced error by 2.0 % compared to traditional PID control. In sinusoidal tracking, both the phase lag and tracking error were significantly reduced. For composite signal tests, control accuracy was improved by 0.98 %. Experimental validation results were consistent with simulation trends, showing an average response error of less than 8.0 % and a tracking error below 1.0 %, fully confirming the superiority of the TDAFSMC strategy in terms of dynamic response, tracking accuracy, and disturbance rejection.

In conclusion, the proposed TDAFSMC method not only effectively enhances the control performance of digital hydraulic cylinder systems, exhibiting strong robustness and engineering applicability, but also provides a theoretical basis and technical support for the precise control of large-scale electro-hydraulic servo systems such as shearers and excavators. This study contributes positively to advancing control technology in high-end equipment systems.

Acknowledgments

This research was supported by the National Natural Science Foundation of China (52204169) and the Heze University Doctoral Foundation (XY24BS04).

References

1. Đào, T.L., & Thanh, L. (2023). Adaptive PID sliding mode controller application to position control of hydraulic system (in Vietnamese). *Journal of Transportation Science and Technology*, *12*(4), 26–33. https://doi.org/10.55228/jtst.12(4).26-33
2. Dang, X.J., Zhao, X.A., Dang, C., Jiang, H., Wu, X., & Zha, L. (2021). Incomplete differentiation-based improved adaptive backstepping integral sliding mode control for position control of hydraulic system. *ISA Transactions*, *109*, 199–217. https://doi.org/10.1016/j.isatra.2020.10.027
3. Gao, G., Zeng, Y., Liu, C., Wang, L., & Liu, R. (2023). Analysis of damping multi-mode switching control of semi-active suspension based on digital controlled hydraulic cylinders group. *Proceedings of the Institution of Mechanical Engineers, Part D: Journal of Automobile Engineering*, *239*(1), 98–112. https://doi.org/10.1177/09544070231210149
4. Ghani, M.F., Ghazali, R., Jaafar, H.I., & Soon, C.C. (2022). Real-time trajectory tracking control of an electro-hydraulic system using a fuzzy logic sliding mode controller. *2022 IEEE International Conference on Artificial Intelligence in Engineering and Technology (IICAIET)*, 1–6, https://doi.org/10.1109/iicaiet55139.2022.9936783
5. Guo, Y.-Q., Zha, X.-M., Shen, Y.-Y., Wang, Y.-N., & Chen, G. (2022). Research on PID position control of a hydraulic servo system based on Kalman genetic optimization. *Actuators*, *11*(6), Article 162. https://doi.org/10.3390/act11060162
6. He, J., Su, S., Wang, H., Chen, F., & Yin, B. (2023). Online PID tuning strategy for hydraulic servo control systems via SAC-based deep reinforcement learning. *Machines*, *11*(6), Article 593. https://doi.org/10.3390/machines11060593
7. Ji, X.H., Wang, C.W., Zhang, Z.Y., Chen, S., & Guo, X.P. (2021). Nonlinear adaptive position control of hydraulic servo system based on sliding mode back-stepping design method. *Proceedings of the Institution of Mechanical Engineers, Part I: Journal of Systems and Control Engineering*, *235*(4), 474–485. https://doi.org/10.1177/0959651820949663
8. Jiang, S.L., Wang, H., & Zhao, G.C. (2022). Research on neural network model reference adaptive disturbance rejection control of digital hydraulic cylinder. *Advances in Mechanical Engineering*, *14*(12). https://doi.org/10.1177/16878132221140706
9. Li, S., & Cao, X.H. (2021). Synchronous control characteristics analysis of shield propulsion hydraulic system based on tracking differentiator and self-adaptive PID. *International Journal of Pattern Recognition and Artificial Intelligence*, *35*(14), Article 2159053. https://doi.org/10.1142/s0218001421590539

10. Li, Z.B., Li, L., Zhang, J.Q., Huang, H.Y., & Sun, C.S. (2023). Nonsingular terminal sliding mode control of voice coil actuator fast steering mirror based on tracking differentiator. *2023 IEEE 18th Conference on Industrial Electronics and Applications (ICIEA)*, 1099–1105. https://doi.org/10.1109/iciea58696.2023.10241813

11. Liu, Y., Jiang, D., Yun, J., Sun, Y., Li, C., Jiang, G., Kong, J., Tao, B., & Fang, Z. (2022a). Self-tuning control of manipulator positioning based on fuzzy PID and PSO algorithm. *Frontiers in Bioengineering and Biotechnology*, *9*, Article 817723. https://doi.org/10.3389/fbioe.2021.817723

12. Liu, Y.J., Peng, X.W., Chen, X., & Guo, Y.J. (2022b). Electro-hydraulic proportional position control based on variable domain fuzzy PID. *2022 41st Chinese Control Conference (CCC)*, 2773–2778. https://doi.org/10.23919/ccc55666.2022.9902221

13. Qi, P.G., Chi, S., Zheng, Y.S., et al. (2024). Research on stiffness characteristics of 6-DOF parallel robot driven by digital hydraulic cylinder (in Chinese). *Journal of Ordnance Equipment Engineering*, *45*(6), 215–223. https://doi.org/10.11809/bqzbgcxb2024.06.030

14. Sun, C., Dong, X., Wang, M., & Li, J. (2022). Sliding mode control of electro-hydraulic position servo system based on adaptive reaching law. *Applied Sciences*, *12*(14), Article 6897. https://doi.org/10.3390/app12146897

15. Wang, L., Guan, S., Wu, Z., Wang, K., Li, Y., & Li, X. (2019). Design and simulation of intelligent lifting system based on digital hydraulic cylinder. *2019 IEEE 4th International Conference on Advanced Robotics and Mechatronics (ICARM)*, 24–29. https://doi.org/10.1109/icarm.2019.8833740

16. Yang, M.X., Zhang, Q., Lu, X.L., Xi, R., & Wang, X.S. (2019). Adaptive sliding mode control of a nonlinear electro-hydraulic servo system for position tracking. *Mechanika*, *25*(4), 283–290. https://doi.org/10.5755/j01.mech.25.4.22822

17. Yu, H., Wang, H., & Guo, C.G. (2024). Analysis of bandwidth expansion and interference suppression of digital hydraulic cylinder system. *International Journal of Control, Automation, and Systems*, *22*(5), 1739–1750. https://doi.org/10.1007/s12555-022-0589-3

18. Zhang, B., Niu, P., Guo, X., & He, J. (2024). Fuzzy PID control of permanent magnet synchronous motor electric steering engine by improved beetle antennae search algorithm. *Scientific Reports*, *14*, Article 2898. https://doi.org/10.1038/s41598-024-52600-8

19. Zhang, J.Z., & Fu, Y.J. (2025). Research on fluid motion characteristics of digital hydraulic cylinder control valve based on amesim and fluent. *Journal of Physics: Conference Series*, *3043*(1), Article 012046. https://doi.org/10.1088/1742-6596/3043/1/012046

20. Zhang, W., Xu, L., Liang, X., Zhang, Y., Yan, W., & Zhou, J. (2022). Position control of traction upper limb rehabilitation robot based on fuzzy sliding mode method. *2022 12th International Conference on CYBER Technology in Automation, Control, and Intelligent Systems (CYBER)*, 654–659. https://doi.org/10.1109/cyber55403.2022.9907696

Manuscript received July 13, 2025; accepted for publication November 15, 2025; published online December 17, 2025.

JOURNAL OF THEORETICAL
AND APPLIED MECHANICS
64, 1, pp. 45–56, Warsaw 2026
https://doi.org/10.15632/jtam-pl/214577

EVALUATION OF VISCOSITY AND RHEOLOGICAL CHARACTERISTICS OF CORN OIL COMBINED WITH GRAPHENE NANOPLATELETS FOR MACHINING LUBRICATION

Pungky EKA SETYAWAN, Anindito PURNOWIDODO*, Achmad AS'AD SONIEF, Yudy SURYA IRAWAN

Faculty of Engineering, Universitas Brawijaya, Malang, East Java, Indonesia
*corresponding author, *anindito@ub.ac.id*

This study aims to analyze the thermal conductivity, dynamic viscosity and rheology of corn oil (CO) with added graphene nanoplatelets (GNPs). The addition of GNPs to CO uses variations of $\Phi = 0.10\,\%$, $\Phi = 0.15\,\%$, $\Phi = 0.20\,\%$, $\Phi = 0.25\,\%$, and $\Phi = 0.30\,\%$. The highest thermal conductivity results were produced at a GNP percentage of $\Phi = 0.30\,\%$ with a value of $0.1620\,\mathrm{W \cdot m^{-1} \cdot K^{-1}}$. The viscosity results show that the highest dynamic viscosity value is produced at GNPs $\Phi = 0.20\,\%$ at all temperatures. The rheology results show that the stable percentage $0.10\,\%$ and $0.20\,\%$ approaches Newtonian properties.

Keywords: thermal conductivity; rheology; corn oil; graphene nanoplatelets; cutting fluid.

Articles in JTAM are published under Creative Commons Attribution 4.0 International.
Unported License https://creativecommons.org/licenses/by/4.0/deed.en.
By submitting an article for publication, the authors consent to the grant of the said license.

1. Introduction

Machining is the process of shaping a workpiece by removing material using a cutting tool. The cutting tool rubs against the material, directly generating significant heat. This significant heat can damage or wear the cutting tool components (Da Silva *et al.*, 2011). Therefore, cutting fluids are crucial for lubrication, cooling, and removing cutting material.

Vegetable oil is an alternative fluid for the machining cooling process. The cooling process is more effective because vegetable oils offer advantages such as a thick film, reduced friction, cutting force, cutting tool wear, and heat reduction (Debnath *et al.*, 2014). Research has frequently been conducted on the use of vegetable oils as cutting fluids, including cottonseed oil, coconut oil, soybean oil, canola oil, castor oil, palm oil, and sunflower oil (Gunjal & Patil, 2018).

Several vegetable oils have disadvantages, including castor oil (high viscosity that can impede fluid flow in the cutting zone), coconut oil (limited performance at high temperatures), and sunflower oil (expensive and limited availability). In contrast, corn oil (CO) offers relatively high saturated fatty acids, enabling it to form a strong film, with moderate viscosity, heat stability, and abundant availability. Therefore, based on these superior properties, CO is a prime candidate for base fluid in cutting fluid applications (Arsene *et al.*, 2021).

Improvements to vegetable oils in cutting fluids have been frequently attempted to enhance their properties, one example being the addition of graphene (Samuel *et al.*, 2011). The addition of graphene reduces friction between the cutting tool surface and the workpiece (Park *et al.*, 2011). This friction reduction results in a gradual, linear reduction in cutting force and temperature with increasing graphene percentage (Uysal, 2017). Furthermore, this reduction also depends on the minimum quantity lubrication (MQL) parameters and the proportion of graphene.

Numerous studies have been conducted to improve the performance of cutting fluids using graphene. Wang *et al.* (2022) examined the effect of adding graphene nanoplatelets (GNPs) and a sulfurized additive to an MQL system in the machining process of Ti-6Al-4V titanium alloy. Graphene nanoplatelets were added at concentrations of 0.05 %, 0.10 %, and 0.20 %, then mixed with the sulfurized additive. Test results showed a reduction in the tool wear rate of up to 31 % and a reduction in surface roughness of 18 %. Crystallographic microscopy observations revealed an even distribution of nanoparticles, improving lubrication and cooling capabilities. Overall, this nanofluid was able to extend tool life, improve surface quality, and improve thermal efficiency (Wang *et al.*, 2022). Caglayan (2021) evaluated the rheological and tribological properties of an oil-based nanofluid modified with silylated GNPs. This nanofluid was prepared by dispersing silane-modified graphene sheets into a base oil without the addition of surfactants or dispersants. Tribological tests were conducted using a ball-on-disk universal friction and wear tester. The test results showed that the addition of silylated GNPs significantly improved lubrication properties and wear resistance, with a reduction in the friction coefficient of up to 40 % and a reduction in wear of 35 % compared to pure base oil.

In a study by Bertolini *et al.* (2021), the use of GNPs as an additive in the MQL system while turning Inconel 718 alloy was shown to provide significant benefits. Graphene additives with concentrations of 0.05 % and 0.10 % were added to vegetable oil as a cutting fluid. The goal is to extend the life of the cutting tool by up to 50 % and improve the surface quality of the machined samples compared to using pure vegetable oil. These improvements are explained by a reduced coefficient of friction between the tool and chips, and increased cooling effectiveness in the cutting zone (Bertolini *et al.*, 2021).

Ramón-Raygoza *et al.* (2016) investigated the rheological and tribological characteristics of an oil-based nanofluid enriched with silane-modified GNPs, without the use of surfactants. Characterization was performed using friction force microscopy and phase contrast microscopy. The results showed that the addition of GNPs improved lubrication and wear resistance, with a 43 % reduction in the friction coefficient and a 63 % increase in wear resistance at a 2 % GNP concentration in the engine oil. The development of this nanofluid supports technological innovation for the modern manufacturing industry, focused on sustainable and environmentally friendly practices.

Vora *et al.* (2023) investigated the rheological properties and thermal conductivity of a nanofluid based on graphene nanoplatelets and castor oil. The nanofluid was prepared by mixing GNPs and castor oil, followed by ultrasonication to obtain a stable dispersion. Test results indicate that GNP/castor oil nanofluid exhibits Newtonian flow, with viscosity decreasing with increasing shear rate.

Manikanta *et al.* (2024) examined the combination of GNPs and CO for cooling during turning machining. GNP concentrations varied from 0.50 % to 3 %, with cutting forces and tool wear reduced by 2.5 %. The rheological characteristics of this study were not investigated.

The highly saturated acid content of CO, as compared to other vegetable oils, will affect lubrication efficiency and film strength. However, research related to cutting fluids using CO as a base fluid with added GNPs is still limited. Furthermore, testing has focused only on tool wear or cutting force reduction, but has never comprehensively analyzed rheological properties. While rheological characteristics are generally essential for analyzing fluid flow, heat transfer, and lubrication, this study aims to fill this gap by characterizing the thermal conductivity, dynamic viscosity, and rheological properties of cutting fluids.

2. Experimental procedure

The method used in this study included the preparation of GNPs. The resulting GNPs were then validated by morphological testing using scanning electron microscopy (SEM) and crystal structure using X-ray diffraction (XRD). The GNPs were then mixed with CO as a base

lubricant. The resulting mixture was then analyzed for thermal conductivity, dynamic viscosity, and rheology.

2.1. Preparation of GNPs/nanofluids

This study used CO as the base oil, which was combined with GNPs to form the nanofluid shown in Fig. 1. The preparation of nanofluids requires more attention to achieve a stable liquid suspension without precipitation. The GNPs used were type KNG-150, with a purity of 99 %, a thickness of 5 nm–10 nm, and a width of 10 µm, produced by Knano Nanotechnology Group (KNG), China. Mazola CO was produced by ACH Food Companies, Inc., USA. The properties of CO are shown in Table 1.

Fig. 1. Photo of pure CO nanofluid and nanofluid Φ 0.10 % to Φ 0.30 %.

Table 1. Properties of CO.

Property	Value
Appearance	Bright golden-yellow color
Specific gravity (at 25 °C)	0.92
Hydroxyl value	0.7–1.5
Saponification value	190–195
Iodine value	110–120
Acid (mg KOH/gram of oil)	0.5–2.0

The preparation of nanofluids aims to produce a homogeneous, stable, durable, and minimally sedimented mixture dispersion, as shown in Fig. 2.

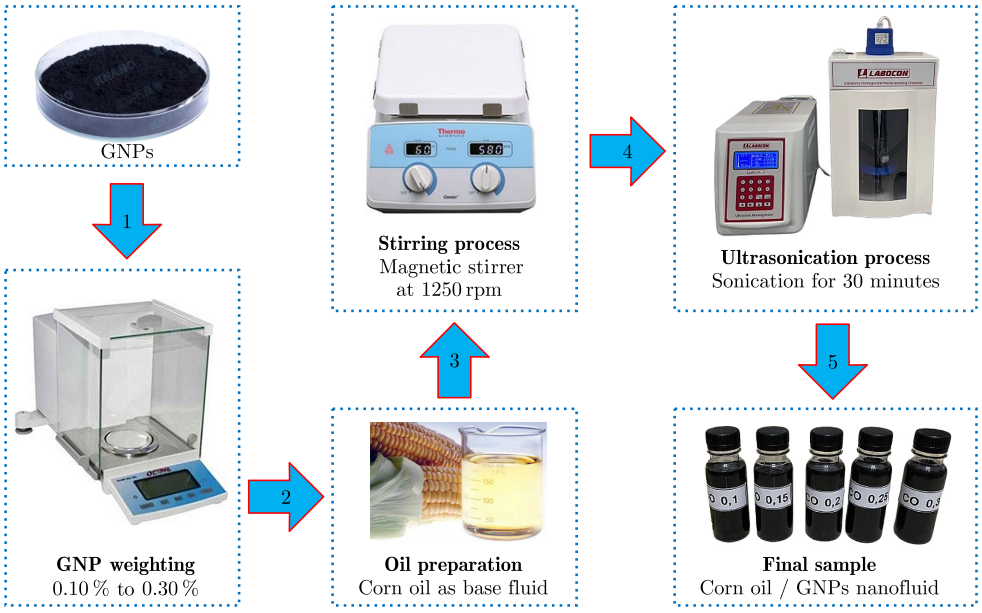

Fig. 2. Schematic of preparation of CO nanofluids combined with GNPs.

The preparation of a mixture of CO and GNP nanofluid was carried out using a two-step method. First, GNPs were weighed accurately using an analytical balance (Optima OPD-E204,

±0.1 mg), with varying concentrations of $\Phi = 0.10\,\%$, $\Phi = 0.15\,\%$, $\Phi = 0.20\,\%$, $\Phi = 0.25\,\%$, and $\Phi = 0.30\,\%$ of the weight of CO. GNPs were added to CO in a beaker, then stirred with a magnetic stirrer at 1250 rpm for 20 min to obtain an initial dispersion. The process was continued with ultrasonic dispersion for 30 min to ensure a stable dispersion and reduce agglomeration of graphene particles.

2.2. Material characterization

The morphology and crystal structure of GNPs were analyzed using SEM and XRD. Figure 3 shows the surface morphology of GNPs, with SEM results at 10 000× and 100 000× magnifications indicating that the GNP nanoparticles have a typical platelet shape, consistent with the GNP datasheet. The crystal structure of GNPs was analyzed using XRD, as shown in Fig. 3. This material characterization is important for identifying material properties, including shape, composition, chemical compounds, and functional groups, in order to understand the material's behavior in specific applications.

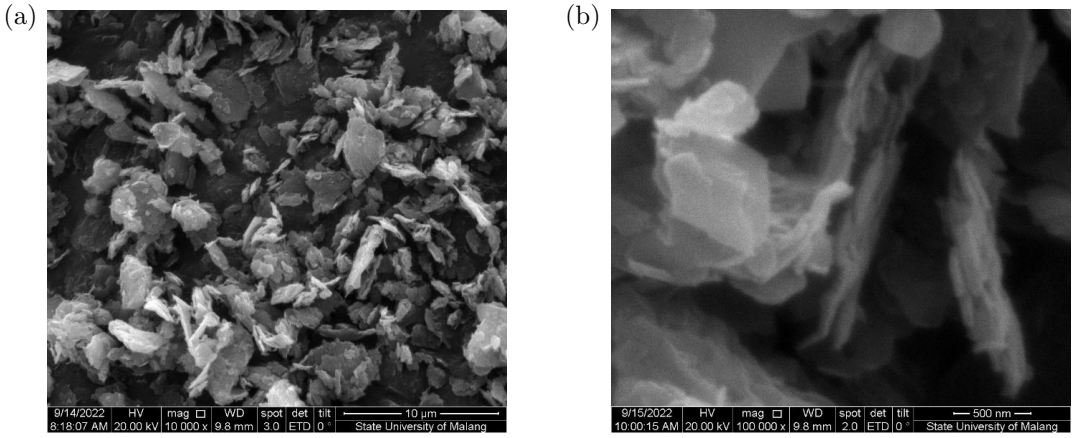

Fig. 3. Results of graphene morphology at magnifications of (a) 10 000× and (b) 100 000×.

XRD testing was conducted to examine the crystal structure and phase of graphene nanomaterials, as shown in Fig. 4. Sharp peaks at $2\theta = 26.4336°$ ((002) plane) and $2\theta = 54.5347°$

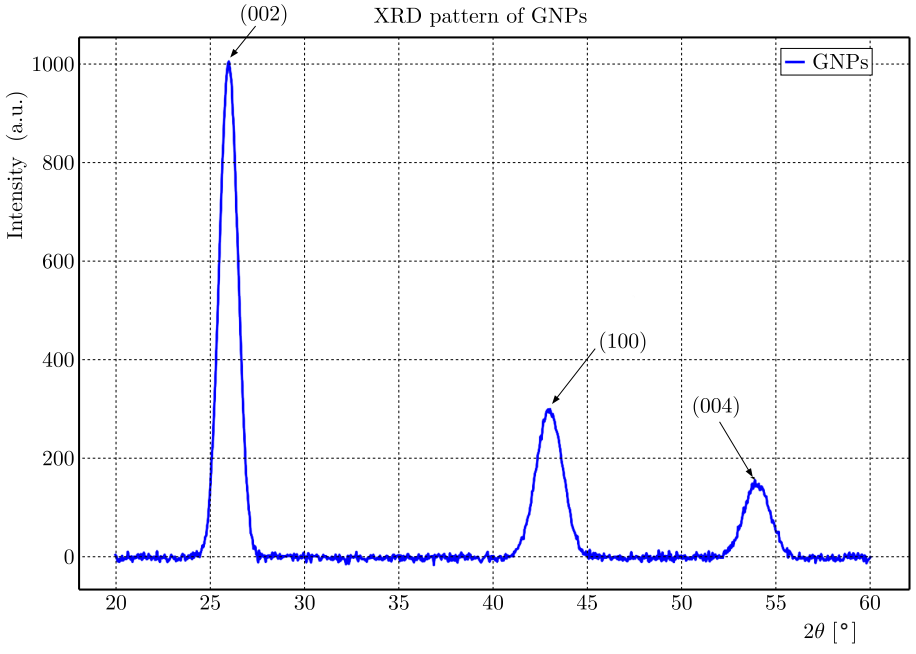

Fig. 4. XRD test graph of graphene nanomaterial.

((004) plane) indicate graphene's typical hexagonal crystal structure. These results indicate that the nanomaterial used is high-quality GNPs. Furthermore, the average crystallite size, calculated using the Scherrer equation, was 31.889 nm at 26.4336° and a FWHM of 0.2558 nm.

2.3. Thermal conductivity

The thermal conductivity of nanofluids was measured with a KD2 Pro Thermal Properties Analyzer using the Modified Transient Plane Source method at a temperature of 30 °C.

2.4. Dynamic viscosity

The dynamic viscosity of nanofluids was measured using an NDJ-8S viscometer at 30 °C and 100 °C. The viscometer geometry used spindles (radius (R_b) = 0.094 cm, cup radius = 0.1405 cm, and length = 0.65 cm). The spindle rotation speeds (n) used were 6 rpm, 12 rpm, 30 rpm, and 60 rpm. The angular velocity was then calculated for each rpm using:

$$\omega = \frac{2\pi}{60} n, \tag{2.1}$$

where ω – angular velocity [rad/s], n – rotation speed [rpm].

From the angular velocity results, the shear rate is then calculated using:

$$\gamma = \frac{2\omega R_{C^2} - R_{b^2}}{x^2(R_{C^2} - R_{b^2})}, \tag{2.2}$$

where γ – shear rate [s^{-1}], ω – angular velocity (spindle) [rad/s], R_C – vessel radius [cm], R_b – radius (spindle) [cm], X – radius at which the shear rate is being calculated [cm].

From the calculation results in Eq. (2.2), the shear rates are 0.0012 s^{-1}, 0.0022 s^{-1}, 0.0055 s^{-1}, and 0.01105 s^{-1}.

3. Results and discussion

3.1. Thermal conductivity

The results of the thermal conductivity test of nanofluids performed with the KD2 Pro Thermal Properties Analyzer are presented in Fig. 5.

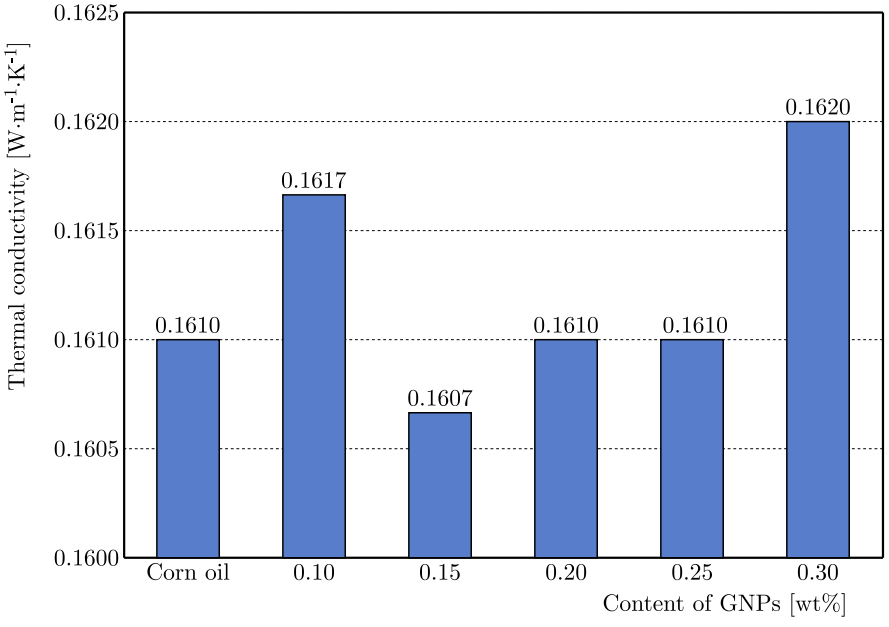

Fig. 5. Thermal conductivity of CO nanofluids with varying concentrations.

Based on the analysis of the thermal conductivity graph, there is an increase in thermal conductivity from the control condition (0 %) of 0.1610 $W \cdot m^{-1} \cdot K^{-1}$ to a nanoparticle concentration of $\Phi = 0.30$ %, which reaches 0.1620 $W \cdot m^{-1} \cdot K^{-1}$, an increase of approximately 1.24 %. This may be compared to the research conducted by Vora *et al.* (2023), where there was an increase in the value of thermal conductivity in nanofluid Al_2O_3/castor oil by 17.4 % at a concentration of 0.50 wt%. The range of values that are quite varied compared to this study is due to differences in several factors, such as the type of base fluid, type of nanoparticle and size, concentration, test temperature, and dispersion stability. Although the increase in this study is relatively small, it remains in the relevant category in MQL. This increase indicates a positive relationship between nanoparticle concentration and thermal conductivity: the higher the nanoparticle concentration (higher Φ), the greater the thermal conductivity (Manikandan & Nanthakumar, 2024). Although there is a small decrease at $\Phi = 0.15$ % (0.1607 $W \cdot m^{-1} \cdot K^{-1}$), which is common in nanofluids, overall, the thermal conductivity remains stable. This indicates that the addition of nanoparticles can increase thermal conductivity by expanding the surface area for heat transfer, although an increase in fluid viscosity also occurs (Kim *et al.*, 2015).

In general, the increase in thermal conductivity of nanofluids is influenced by several factors, namely: the concentration of nanoparticles, the type of nanoparticle material, and temperature (Bertolini *et al.*, 2021; Halelfadl *et al.*, 2013). Nanoparticles with high thermal conductivity will be more effective in increasing the thermal conductivity of nanofluids compared to nanoparticles that have low thermal conductivity (Jang *et al.*, 2022). In addition, the higher the concentration of nanoparticles in the fluid, the higher the thermal conductivity of the nanofluids. A moderate increase in thermal conductivity in GNP-rich CO nanofluids will be very beneficial for improving cooling capabilities in the machining process. With higher thermal conductivity, nanofluids can be more effective in transferring heat from the cutting zone, thereby reducing the cutting temperature and preventing tool wear more effectively.

3.2. Dynamic viscosity

The following are the results of the viscosity test of nanofluids against rotation at temperatures of 40 °C, 60 °C, 80 °C, and 100 °C (Fig. 6). The purpose of this test is to analyze the dynamic viscosity at various temperatures against the weight percentage of GNP. The results obtained in this study will provide the potential for GNP/CO fluid as a cutting fluid used in machining processes.

The decrease in viscosity at high shear rates provides advantages in the cooling process in machining. Cooling in the cutting zone increases the high shear rate. This condition allows fluid to flow more easily at the tool-workpiece interface, thereby minimizing temperature and tool wear. The highest viscosity is produced at a weight percentage of 0.20 % GNP at all temperatures, while the lowest is produced in pure CO. The addition of nanoparticles to the CO solution increases the GNP concentration, resulting in a higher dynamic viscosity value for the nanofluid. However, the increase in dynamic viscosity with increasing concentration is not always linear or significant, especially at higher concentrations or in systems with complex interparticle interactions (Yahya *et al.*, 2024). In addition, the increase in viscosity is also caused by the presence of van der Waals attraction forces, where the inhibition of non-particle agglomeration occurs due to electrostatic repulsion caused by the presence of surfactants. Increasing the concentration of GNP will make the attractive force become more dominant than the repulsive force, causing agglomeration in the nanoparticles (Ebrahim *et al.*, 2023). Agglomeration in nanoparticles requires a greater force to separate the dispersed particles so that the internal shear stress in the nanofluid increases. This condition will linearly increase the viscosity (Müller *et al.*, 2021). Dynamic viscosity in cutting fluid applications plays a very important role, especially in thermal characteristics. In addition, cutting fluid with the right viscosity will provide a high film layer in the machining process, thereby minimizing tool wear.

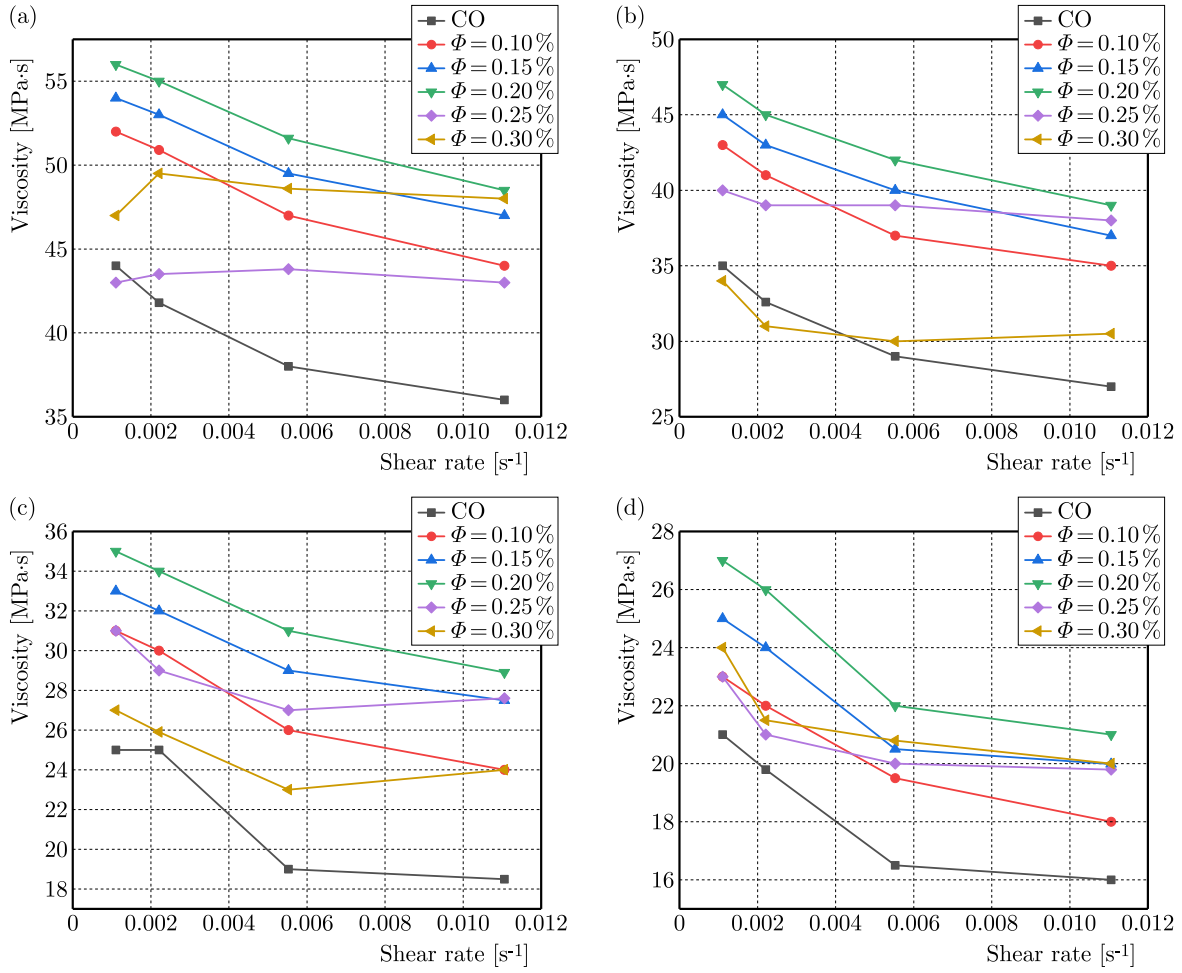

Fig. 6. Dynamic viscosity of cutting fluid versus shear rate at different temperatures: (a) 40 °C; (b) 60 °C; (c) 80 °C; (d) 100 °C. The case $\Phi = 0\,\%$ (corn oil (CO)) represents the base cutting fluid without GNPs, and legends indicate GNP concentrations ($\Phi = 0.10\,\%$ to $0.30\,\%$).

Viscosity decreases with an increasing shear rate (Fig. 6 and Fig. 7). This behavior exhibits pseudoplastic characteristics commonly found in nanofluids. In machining processes, this behavior is crucial because the contact area between the tool surface and the workpiece is very

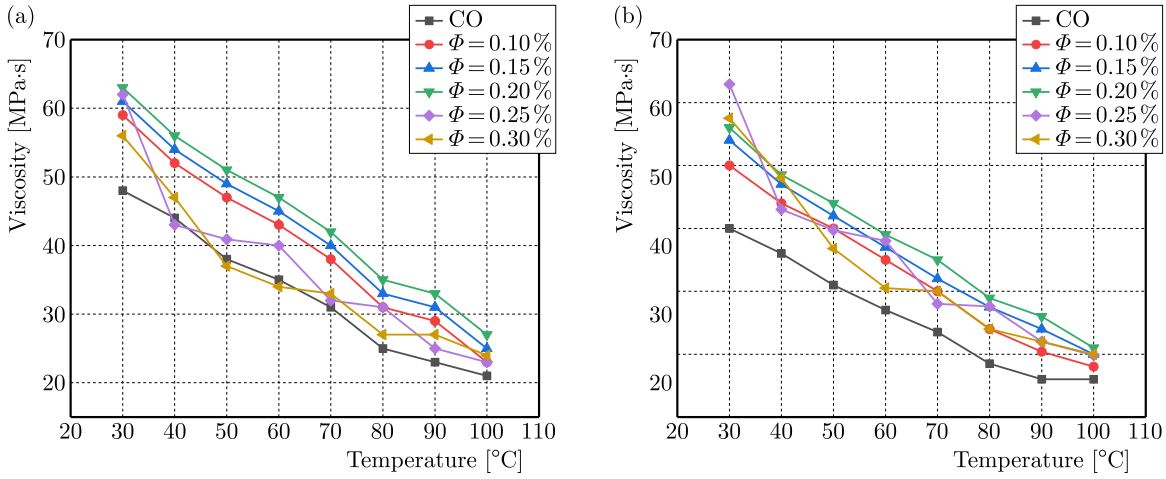

Fig. 7. Viscosity of cutting fluids with temperature at constant shear rates: (a) $0.0011\,\mathrm{s}^{-1}$ and (b) $0.011\,\mathrm{s}^{-1}$. The case $\Phi = 0\,\%$ (corn oil (CO)) represents the base cutting fluid without GNPs, and legends indicate GNP concentrations ($\Phi = 0.10\,\%$ to $0.30\,\%$).

large, causing the fluid to become thinner and accelerate flow in the cutting area, minimizing temperature and cooling efficiency. Conversely, under low shear rate conditions (before contact with the workpiece), the viscosity is relatively high, resulting in the formation of a strong film layer. The combination of high viscosity at low shear rates and low viscosity at high shear rates provides optimal protection and minimizes tool wear.

Under these conditions, in Fig. 7, the shear rate was kept constant between $0.0011\,s^{-1}$ and $0.011\,s^{-1}$, with a temperature range from 30 °C to 100 °C. The graph shows that viscosity decreases with increasing temperature at all shear rates. This decrease is caused by the increase in kinetic energy of fluid molecules at high temperatures, resulting in a weakening of intermolecular adhesion forces (La Mantia *et al.*, 2021). In general, Fig. 7 shows that viscosity decreases at high temperatures but remains stable up to 100 °C. This condition is also important in MQL cooling because high temperatures can reduce film thickness. However, because the viscosity decrease occurs in a controlled manner, the flow and distribution of the lubricant on the tool surface remain uniform.

3.3. Rheology

The results of the nanofluid rheology test can be seen in Fig. 8, which presents the relationship between shear stress and shear rates for GNP/CO nanofluid, showing that shear stress increases linearly with the shear rate at various temperatures. The Ostwald–de Waele method relates to the relationship between shear stress and the shear rate, which is used in calculating the

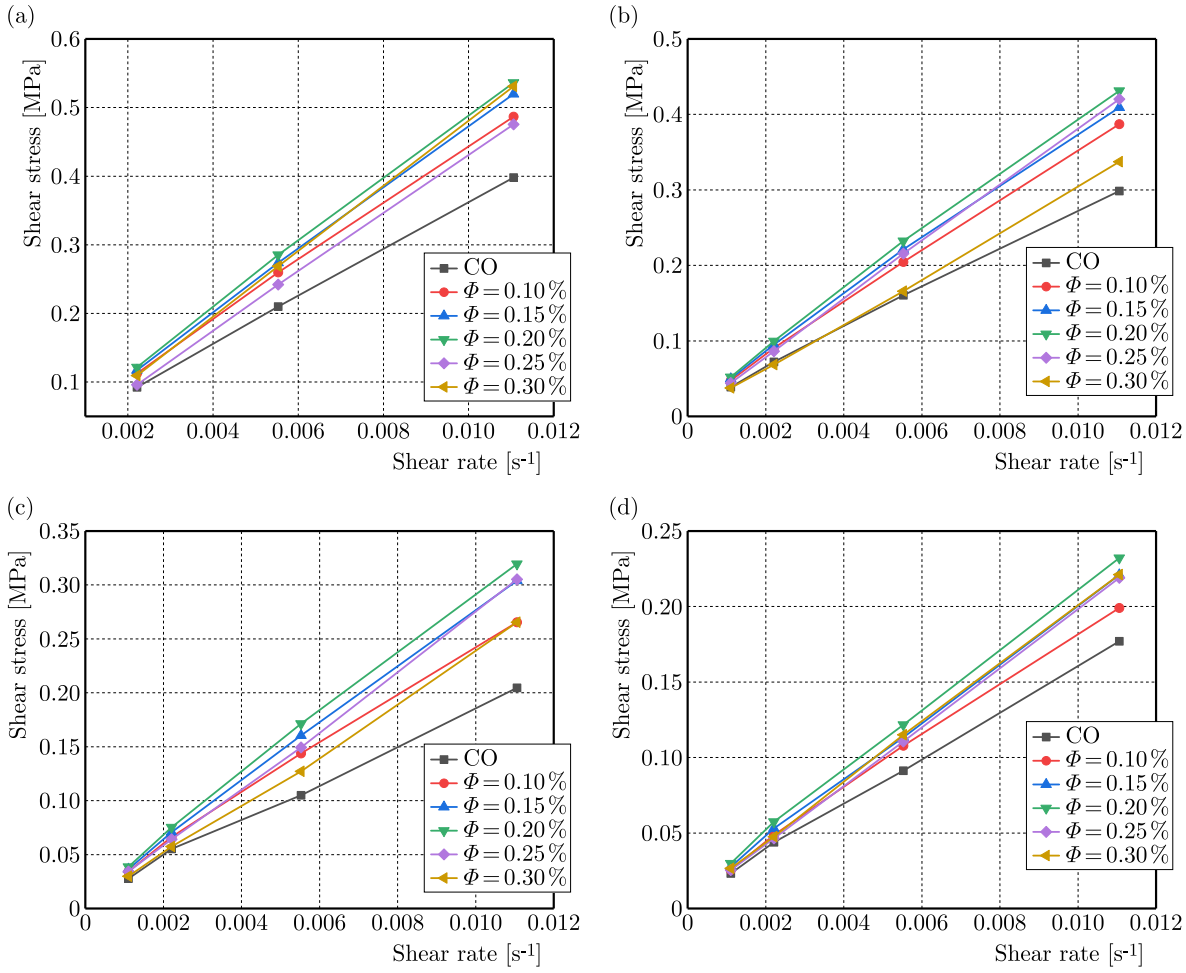

Fig. 8. Shear stress versus shear rate of cutting fluid at different temperatures: (a) 40 °C; (b) 60 °C; (c) 80 °C; (d) 100 °C. The case $\Phi = 0\,\%$ (corn oil (CO)) represents the base cutting fluid without GNPs, and legends indicate GNP concentrations ($\Phi = 0.10\,\%$ to $0.30\,\%$).

consistency index (m) and flow index (n). A flow index less than 1 indicates pseudoplastic behavior. Pseudoplastic behavior is characterized by a decrease in viscosity as the shear rate increases. Conversely, a flow index greater than 1 indicates dilatant flow, where an increase in the shear rate is followed linearly by viscosity (Chehadeh *et al.*, 2023).

At concentrations >0.20 wt%, the n value drops below 1 (e.g., 0.867 at 0.30 wt%), indicating a more dominant pseudoplastic behavior. This property is beneficial in increasing fluid penetration in the micro-contact area between the tool and the workpiece, where high friction and heat concentration occur.

Table 2 and Fig. 9 show that the power law index value at GNP percentage of 0.10 % to 0.20 % deviates from 1 (0.937–0.974). This value is still within the experimental uncertainty limit (±0.05), so it can be categorized as almost Newtonian, where the viscosity is relatively stable

Table 2. Power law index (n) and consistency index (m).

GNP [wt%]	Index	Temperature			
		40 °C	60 °C	80 °C	100 °C
0	m	26.588	17.422	25.000	11.783
	n	0.926	0.898	1	0.915
0.10	m	42.151	42.151	22.465	14.864
	n	0.969	0.969	0.953	0.936
0.15	m	44.944	28.795	8.995	16.743
	n	0.973	0.934	0.809	0.941
0.20	m	46.918	30.664	26.329	18.568
	n	0.974	0.937	0.958	0.945
0.25	m	48.170	31.194	16.103	9.413
	n	1.017	0.963	0.904	0.869
0.30	m	78.187	13.725	18.568	8.148
	n	1.075	0.867	0.945	0.841

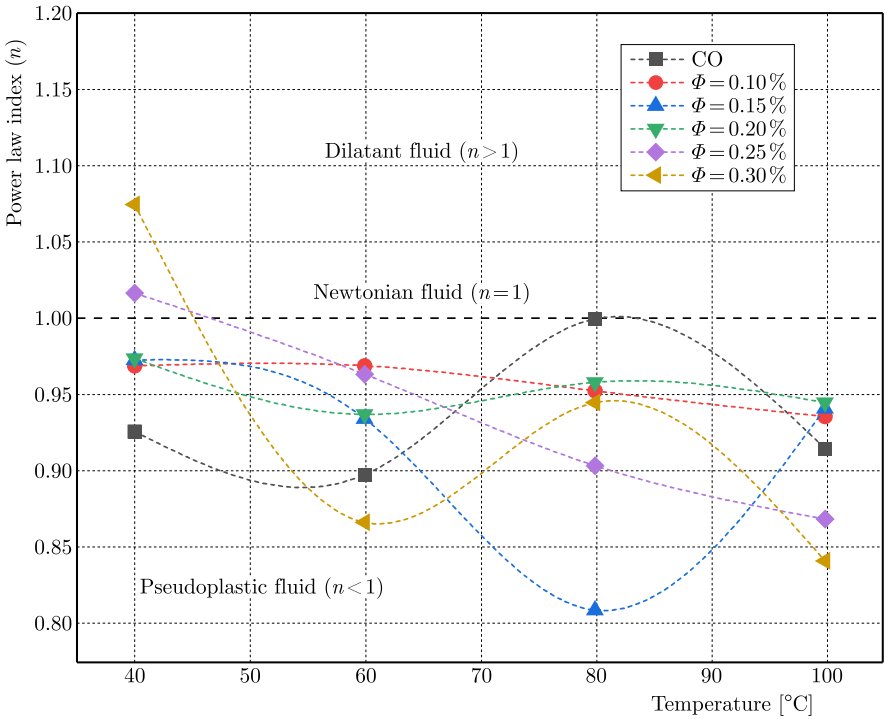

Fig. 9. Power law index against temperature for corn oil (CO, $\Phi = 0\,\%$) and nanoparticle-enhanced fluids with volume fractions $\Phi = 0.10\,\%$ to $0.30\,\%$.

against changes in the shear rate. This stability is crucial for low-pressure MQL lubrication systems because it ensures a constant flow from the nozzle into the cutting zone area, prevents spray fluctuations, and produces a uniform lubricant film (Gomez *et al.*, 2022).

Furthermore, Fig. 10 shows the relationship between the consistency index and temperature. The consistency index appears to decrease with increasing temperature. This condition indicates that with increasing temperature, fluid mobility also decreases and has an impact on reducing resistance in flowing fluid. Increasing temperature causes molecules in the fluid to move faster, reduces interactions between molecules as well as fluid viscosity. In addition, this generally occurs in pseudoplastic fluids (power law), where the dynamic viscosity value decreases exponentially with temperature, whereas according to the Arrhenius model, this is a normal effect based on increasing molecular energy and the release of internal structural networks (Adebowale & Sanni, 2013; Ahmed & Ramaswamy, 2003). Furthermore, the decrease in temperature under MQL conditions increases cooling efficiency because the fluid flows more easily and absorbs heat at high temperatures. However, this tendency needs to be optimized to avoid compromising the strength of the lubricant film at extreme temperatures.

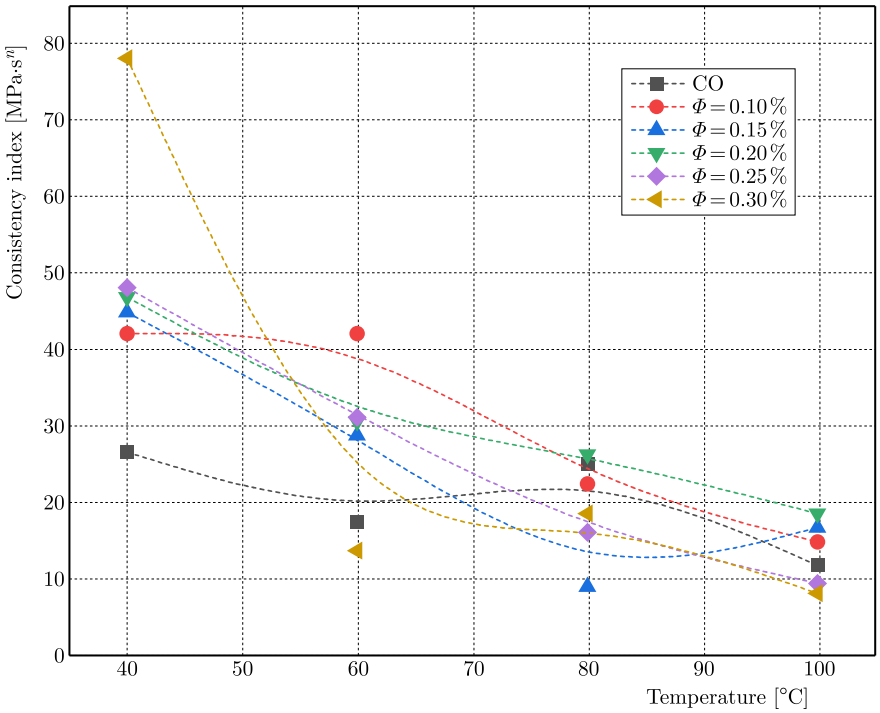

Fig. 10. Consistency index against temperature for corn oil (CO, $\Phi = 0\,\%$) and nanoparticle-enhanced fluids with volume fractions $\Phi = 0.10\,\%$ to $0.30\,\%$.

4. Conclusion

The purpose of this study was to analyze the thermal conductivity, dynamic viscosity, and rheological behavior of CO combined with GNPs. The results showed that the highest thermal conductivity was obtained at a concentration of $\Phi = 0.30\,\mathrm{wt\%}$, with a value of $0.1620\,\mathrm{W \cdot m^{-1} \cdot K^{-1}}$. This increase in thermal conductivity will provide the nanofluid's ability to remove heat from the cutting zone area, thereby reducing cutting temperatures and reducing tool wear. The highest viscosity value was found at $\Phi = 0.20\,\mathrm{wt\%}$, which indicates that increasing the GNP concentration strengthens the intermolecular attractive forces and encourages particle agglomeration. This agglomeration requires more energy to maintain dispersion stability, which can affect long-term performance. Rheological results show that nanofluids at $\Phi = 0.10\,\%$ and $\Phi = 0.20\,\%$ exhibit near-Newtonian properties, with a flow index (n) close to 1. This viscosity stability against changes in the shear rate is very beneficial in the lubrication of machining processes, as it en-

sures a constant fluid flow in the MQL nozzle and the formation of a uniform lubricant film at the tool-chip interface. Overall, GNP-CO nanofluid has the potential to be an environmentally friendly lubricant capable of improving cooling efficiency, reducing friction, and minimizing tool wear under real-world machining conditions. However, further research is needed to improve sedimentation stability and long-term dispersion resistance, which are important factors in industrial applications.

Acknowledgments

This research received funding support from the Ministry of Research and Technology (Directorate General of Higher Education) through a BPPDN scholarship under contract number B/67/D.D3/KD.02.00/2019. Furthermore, this research received funding support from the University of Merdeka Malang through the LPPM (Research Institute for Research and Community Service) in 2025. This research received data analysis and review support from Prof. Mahros Darsin, S.T., M.Sc., Ph.D., a lecturer at the University of Jember.

References

1. Adebowale, A.-R.A., & Sanni, L.O. (2013). Effects of solid content and temperature on viscosity of tapioca meal. *Journal of Food Science and Technology*, *50*(3), 573–578. https://doi.org/10.1007/s13197-011-0363-7
2. Ahmed, J., & Ramaswamy, H.S. (2003). Effect of high-hydrostatic pressure and temperature on rheological characteristics of glycomacropeptide. *Journal of Dairy Science*, *86*(5), 1535–1540. https://doi.org/10.3168/jds.S0022-0302(03)73738-2
3. Arsene, B., Gheorghe, C., Sarbu, F.A., Barbu, M., Cioca, L.-I., & Calefariu, G. (2021). MQL-assisted hard turning of AISI D2 steel with corn oil: Analysis of surface roughness, tool wear, and manufacturing costs. *Metals*, *11*(12), Article 2058. https://doi.org/10.3390/met11122058
4. Bertolini, R., Ghiotti, A., & Bruschi, S. (2021). Graphene nanoplatelets as additives to MQL for improving tool life in machining Inconel 718 alloy. *Wear*, *476*, Article 203656. https://doi.org/10.1016/j.wear.2021.203656
5. Caglayan, M.O. (2021). Rheological and tribological characterization of novel modified graphene/oil-based nanofluids using force microscopy. *Microscopy Research & Technique*, *84*(4), 814–827. https://doi.org/10.1002/jemt.23641
6. Chehadeh, D., Ma, X., & Al Bazzaz, H. (2023). Recent progress in hydrotreating kinetics and modeling of heavy oil and residue: A review. *Fuel*, *334*(1), Article 126404. https://doi.org/10.1016/j.fuel.2022.126404
7. Da Silva, R.B., Vieira, J.M., Cardoso, R.N., Carvalho, H.C., Costa, E.S., Machado, A.R., & De Ávila, R.F. (2011). Tool wear analysis in milling of medium carbon steel with coated cemented carbide inserts using different machining lubrication/cooling systems. *Wear*, *271*(9–10), 2459–2465. https://doi.org/10.1016/j.wear.2010.12.046
8. Debnath, S., Reddy, M.M., & Yi, Q.S. (2014). Environmental friendly cutting fluids and cooling techniques in machining: A review. *Journal of Cleaner Production*, *83*, 33–47. https://doi.org/10.1016/j.jclepro.2014.07.071
9. Ebrahim, S.A., Pradeep, E., Mukherjee, S., & Ali, N. (2023). Rheological behavior of dilute graphene-water nanofluids using various surfactants: An experimental evaluation. *Journal of Molecular Liquids*, *370*, Article 120987. https://doi.org/10.1016/j.molliq.2022.120987
10. Gómez-Merino, A.I., Jiménez-Galea, J.J., Rubio-Hernández, F.J., & Santos-Ráez, I.M. (2022). Experimental assessment of thermal and rheological properties of coconut oil-silica as green additives in drilling performance based on minimum quantity of cutting fluids. *Journal of Cleaner Production*, *368*, Article 133104. https://doi.org/10.1016/j.jclepro.2022.133104
11. Gunjal, S.U., & Patil, N.G. (2018). Experimental investigations into turning of hardened AISI 4340 steel using vegetable based cutting fluids under minimum quantity lubrication. *Procedia Manufacturing*, *20*, 18–23. https://doi.org/10.1016/j.promfg.2018.02.003

12. Halelfadl, S., Estellé, P., Aladag, B., Doner, N., & Maré, T. (2013). Viscosity of carbon nanotubes water-based nanofluids: Influence of concentration and temperature. *International Journal of Thermal Sciences*, *71*, 111–117. https://doi.org/10.1016/j.ijthermalsci.2013.04.013

13. Jang, J.-u., Nam, H.E., So, S.O., Lee, H., Kim, G.S., Kim, S.Y., & Kim, S.H. (2022). Thermal percolation behavior in thermal conductivity of polymer nanocomposite with lateral size of graphene nanoplatelet. *Polymers*, *14*(2), Article 323. https://doi.org/10.3390/polym14020323

14. Kim, S.Y., Noh, Y.J., & Yu, J. (2015). Thermal conductivity of graphene nanoplatelets filled composites fabricated by solvent-free processing for the excellent filler dispersion and a theoretical approach for the composites containing the geometrized fillers. *Composites Part A: Applied Science and Manufacturing*, *69*, 219–225. https://doi.org/10.1016/j.compositesa.2014.11.018

15. La Mantia, F.P., Titone, V., Milazzo, A., Ceraulo, M., & Botta, L. (2021). Morphology, rheological and mechanical properties of isotropic and anisotropic PP/rPET/GnP nanocomposite samples. *Nanomaterials*, *11*(11), Article 3058. https://doi.org/10.3390/nano11113058

16. Manikandan, S., & Nanthakumar, A.J.D. (2024). Development of a predictive model for thermal conductivity in graphene nanoplatelets-infused damper oil using ANN/RSM. *Thermal Science*, *28*(5B), 4235–4247. https://doi.org/10.2298/TSCI231130152M

17. Manikanta, J.E., Naga Raju, B., & Satankar, R.K. (2024). Development and characterization of novel green cutting fluids with nano-additives. *Periodica Polytechnica Mechanical Engineering*, *68*(4), 304–311. https://doi.org/10.3311/PPme.23466

18. Müller, M., Stahl, L., Arafat, R., Madanchi, N., & Herrmann, C. (2021). A case study on the observability of cutting fluid flow and the associated contact mechanics in scaled rough surfaces. *SN Applied Sciences*, *3*(5), Article 570. https://doi.org/10.1007/s42452-021-04572-x

19. Park, K.-H., Ewald, B. & Kwon, P.Y. (2011). Effect of nano-enhanced lubricant in minimum quantity lubrication balling milling. *Journal of Tribology*, *133*(3), Article 031803. https://doi.org/10.1115/1.4004339

20. Ramón-Raygoza, E.D., Rivera-Solorio, C.I., Giménez-Torres, E., Maldonado-Cortés, D., Cardenas-Alemán, E., & Cué-Sampedro, R. (2016). Development of nanolubricant based on impregnated multilayer graphene for automotive applications: Analysis of tribological properties. *Powder Technology*, *302*, 363–371. https://doi.org/10.1016/j.powtec.2016.08.072

21. Samuel, J., Rafiee, J., Dhiman, P., Yu, Z.-Z., & Koratkar, N. (2011). Graphene colloidal suspensions as high performance semi-synthetic metal-working fluids. *The Journal of Physical Chemistry C*, *115*(8), 3410–3415. https://doi.org/10.1021/jp110885n

22. Uysal, A. (2017). An experimental study on cutting temperature and burr in milling of ferritic stainless steel under MQL using nano graphene reinforced cutting fluid. *Advanced Materials Proceedings*, *2*(9), 560–563. https://doi.org/10.5185/amp.2017/038

23. Vora, V., Sharma, R.K., & Bharambe, D.P. (2023). Investigation of rheological and thermal conductivity properties of castor oil nanofluids containing graphene nanoplatelets. *International Journal of Thermophysics*, *44*(10), Article 155. https://doi.org/10.1007/s10765-023-03264-5

24. Wang, B., Yang, Q., Deng, J., Hou, N., Wang, X., & Wang, M. (2022). Effect of graphene nanoparticles and sulfurized additives to MQL for the machining of Ti-6Al-4 V. *The International Journal of Advanced Manufacturing Technology*, *119*(5–6), 2911–2921. https://doi.org/10.1007/s00170-021-08348-w

25. Yahya, M.N., Mohd Norddin, M.N.A., Ismail, I., Rasol, A.A.A., Risal, A.R., Yakasai, F., Oseh, J.O., Ngouangna, E.N., Younas, R., Ridzuan, N., Mahat, S.Q.A., & Agi, A. (2024). Graphene nanoplatelet surface modification for rheological properties enhancement in drilling fluid operations: A review. *Arabian Journal for Science and Engineering*, *49*(6), 7751–7781. https://doi.org/10.1007/s13369-023-08458-5

Manuscript received August 8, 2025; accepted for publication November 21, 2025; published online February 13, 2026.

JOURNAL OF THEORETICAL
AND APPLIED MECHANICS
64, 1, pp. 57–70, Warsaw 2026
https://doi.org/10.15632/jtam-pl/215405

PHYSICS-INFORMED NEURAL NETWORKS FOR INHOMOGENEOUS SWELLING ANALYSIS OF DUAL-LAYER GELS WITH CHAIN ENTANGLEMENT EFFECTS

Hengdi SU, Feifei SONG, Chengjin SUN, Jianjun ZHANG*

College of Information and Management Science, Henan Agricultural University, Zhengzhou, China
*corresponding author, *zjj@henau.edu.cn*

A field theory incorporating Edwards–Vilgis slip-link elasticity with Flory–Huggins mixing is developed for dual-layer gels containing rigid cores, capturing chain entanglement effects neglected by Neo–Hookean models. Physics-informed neural networks (PINNs) transform complexities of handling interfacial constraints into a neural network optimization problem, thereby reducing both algorithmic complexity and implementation requirements. Systematic parametric studies demonstrate that micromaterial parameters critically govern stress distributions, solvent concentration profiles, and swelling behavior. The framework enables precise control of target solvent concentrations and equilibrium configurations through optimal micromaterial parameter selection and thickness ratio design in dual-layer spherical gel systems.

Keywords: dual-layer gels; physics-informed neural networks; chain entanglement.

Articles in JTAM are published under Creative Commons Attribution 4.0 International.
Unported License https://creativecommons.org/licenses/by/4.0/deed.en.
By submitting an article for publication, the authors consent to the grant of the said license.

1. Introduction

Upon contact with a network of hydrophilic crosslinked polymer chains, solution molecules become enmeshed within the network due to intermolecular attractions, leading to volumetric expansion through solution imbibition. This hydrated, expanded state is characteristically termed a polymeric gel, which exhibits high solvent uptake and substantial swelling ratios, enabling applications in tissue engineering (Khan *et al.*, 2024), self-folding structures (Zhao *et al.*, 2021), and soft robotics (López-Díaz *et al.*, 2024). Their programmable deformation capabilities and tunable mechanical properties establish gels as essential materials for interdisciplinary technological advancement. In many applications, gels are commonly interfaced with diverse materials to create composite gel systems (Yang *et al.*, 2020), including gel-metal, gel-gel, and gel-tissue interfaces. Spherical gel shells coating a rigid core have been extensively studied due to their broad utility in soft matter and biomedical applications (Ballauff & Lu, 2007). However, single-layer gels often lack the functional versatility required to satisfy multiple design criteria. In contrast, multilayer gels offer a compelling solution by enabling spatially tailored properties across distinct layers. For example, Yan *et al.* (2021) developed a chitosan/silver nanoparticle multilayer gel that exploits chitosan's capacity to adsorb and stabilize metal salts, coupled with the antimicrobial action arising from silver-ion diffusion. In gel micro-valves, a relatively stiff outer layer is particularly beneficial, as it induces compressive radial stresses that stabilize the core-shell structure and reduce wear and degradation of the softer inner gel. The preparation, characterization and application of multilayer gels have been comprehensively reviewed by (Jin *et al.*, 2021).

When subjected to external mechanical constraints during equilibration, these gels typically develop inhomogeneous and anisotropic swelling deformations characterized by non-uniform solvent distribution. To better harness these gel systems, many theories have been established to elucidate and interpret the swelling behavior of gel systems under diverse mechanical con-

straints. Zhao *et al.* (2008) characterized the inhomogeneous and anisotropic equilibrium behavior in spherical gel shells adhered to rigid core materials, demonstrating how mechanical constraints in core-shell architectures influence swelling patterns. Morimoto and Ashida (2015) investigated bilayer gel systems comprising two thermally responsive hydrogel layers with differential swelling properties, observing spontaneous bending upon immersion in solution at specific temperatures. Ahmadi *et al.* (2020) conducted quantitative analyses of displacement fields, stress distributions, and solvent concentration gradients in bi-layered spherical hydrogels bonded to rigid cores. Wu and Zhong (2013) systematically evaluated the swelling equilibrium states of core-shell-coating gel structures.

The aforementioned theoretical frameworks characterizing deformation phenomena of gel systems are predominantly formulated within continuum mechanics principles, employing the Flory–Rehner free energy function as the fundamental constitutive relation that governs the material response. This idealized formulation integrates the Gaussian chain model to characterize the elastic response of polymer networks with the Flory–Huggins solution theory to account for polymer-solvent mixing energetics. Despite its widespread application in modeling various chemo-mechanical coupling phenomena in polymer gels, the classical Flory–Rehner model employs a Neo–Hookean representation for the network stretching free energy, which notably neglects chain extensibility limitations. To address this limitation, Chester and Anand (2010) developed a refined theory based on non-Gaussian statistical mechanics of polymer chains. While this non-Gaussian approach offers a more physically realistic representation compared to Gaussian statistics, it fails to incorporate the significant effects of chain entanglements – a crucial consideration given that these entanglements are ubiquitous in actual gel networks due to the fundamental uncrossability of network chains. These uncrosslinked polymer chain interactions, termed slip-links, represent inevitable structural features in hydrogel preparation, as the formation of defect-free chemically cross-linked polymer networks remains practically unattainable. Numerous models have been developed to characterize the entanglement effects in cross-linked polymer networks. Among these, the Edwards–Vilgis slip-link model (Edwards & Vilgis, 1986) has been shown to exhibit the strongest agreement with experimental results, as demonstrated by comparative analyses with experimental data (Urayama *et al.*, 2003). Yan and Jin (2012) propose a novel hybrid free energy function for polymeric gels that combines the Edwards–Vilgis slip-link model of elasticity with the Flory–Huggins mixing formulation, by which some elementary deformation scenarios in single-component gel segments are carried out, showing good agreement with experimental results.

In this work, we systematically investigate the influence of entanglements on the inhomogeneous and anisotropic swelling behavior of dual-layer gels containing rigid cores, and establish a rigorous framework for the design and optimization of micromechanical properties and thickness ratios in dual-layer gel systems, enabling precise control over target solvent concentrations and sealing-induced stresses.

Traditionally, complex phenomena in gel systems have been analyzed using finite element methods. However, these conventional numerical approaches require iterative solution procedures when addressing differential equations with interface continuity conditions, which necessitate the successive resolution of the governing equations at each iteration step, resulting in increased computational complexity and implementation overhead (Abdolahi *et al.*, 2017). Furthermore, these mesh-based methods necessitate the discretization of the computational domain into mesh points, approximating solutions at these discrete locations while yielding results with limited differentiability.

Recent years have witnessed a transformative application of artificial neural networks (ANNs) – also known as deep neural networks (DNNs) or deep learning (DL) – across numerous disciplines including image classification, handwriting recognition, speech processing, and computer vision. These computational paradigms have subsequently emerged in scientific computing, particularly for solving partial differential equations (PDEs). Among these approaches, physics-

informed neural networks (PINNs) have become a prominent methodology for training DNN-based solutions to PDEs and have been successfully applied to various engineering challenges (Diao *et al.*, 2023; Raissi *et al.*, 2019). In our prior work (Su *et al.*, 2021; 2022), we employed a deep learning approach to model the swelling behavior of core-shell gel responding to environmental stimuli. The inherent flexibility in defining DNNs, coupled with significant advances in algorithmic efficiency, positions DNNs as a compelling alternative for PDE solution approximation.

In this study, we employ PINNs to investigate the swelling behavior of dual-layer gels. The interface continuity conditions are elegantly incorporated into the loss function alongside other governing physical laws, thereby transforming the complexities of solving governing equations with interface continuity conditions into a neural network optimization problem. This approach represents a significant paradigm shift in computational mechanics, where traditional numerical challenges are reframed within the well-established domain of deep learning optimization techniques. Furthermore, PINNs generate closed-form, analytically differentiable solutions – a substantial advantage for subsequent calculations compared to the discrete or limited-differentiability solutions offered by conventional methods. Moreover, the near-mathematical syntax facilitated by TensorFlow or PyTorch frameworks enhances both implementation clarity and accessibility. Last but not least, PINNs efficiently leverage modern parallel computing architectures, enabling effective deployment across multiple graphics processing units (GPUs) or tensor processing units (TPUs).

The remainder of this paper is organized as follows: Section 2 presents a comprehensive theoretical framework for modeling the inhomogeneous and anisotropic swelling behavior of dual-layer spherical gels containing rigid cores, with particular emphasis on the incorporation of chain entanglement effects through the Edwards–Vilgis slip-link model. Section 3 introduces the PINN methodology specifically adapted for solving the dual-layer gel problem. Section 4 provides a systematic investigation of the influence of micromaterial parameters on the mechanical behavior of dual-layer gel systems.

2. Model description

2.1. Kinematic relations and equilibrium equations

In Fig. 1, we present a schematic illustration of inhomogeneous swelling deformations in a dual-layer spherical gel system with distinct micromaterial parameters. The reference state (Fig. 1a) depicts two stress-free dry spherical gels perfectly adhered to a rigid core. Gel 1 occupies the inner layer region $B^{(1)}$ between radii R_{in} and R_{inter}, while gel 2 forms the outer layer region between R_{inter} and R_{out}. Let $\boldsymbol{\chi}^{(s)}$, $s = 1, 2$ be first-order tensor fields denoting the deformation mappings from the regions $B^{(s)}$ into their deformed states occupying the regions $\mathcal{B}^{(s)}$ (throughout the subsequent analysis, where the superscript s appears without explicit specification of its range, it is understood to take values $s = 1, 2$, corresponding to the respective gel layers). Upon immersion in a solvent with chemical potential $\mu = 0$, the system reaches equilibrium with

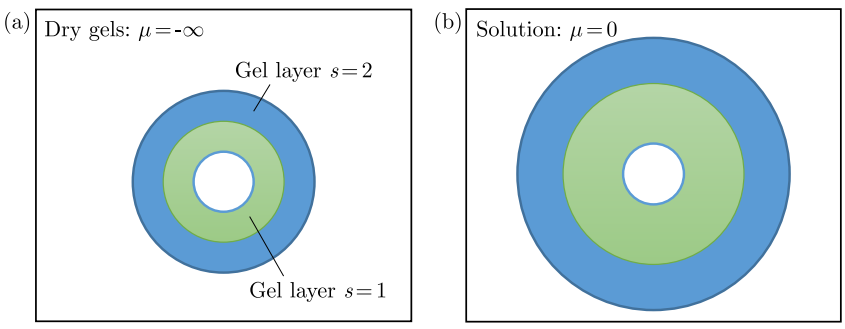

Fig. 1. Schematic illustration of a dual-layer gel containing a rigid core: (a) fluid-free and stress-free state serving as the reference configuration; (b) swollen state reaches equilibrium with the surrounding solution.

the external solution (Fig. 1b). Utilizing the orthogonal Cartesian basis vectors $\mathbf{e}_i$ $(i = 1, 2, 3)$, we formulate a spherical coordinate system $\mathbf{e}_R$, $\mathbf{e}_\theta$, and $\mathbf{e}_\varphi$. The deformation gradient can be represented by

$$\mathbf{F}^{(s)} = \boldsymbol{\chi}^{(s)} \otimes \nabla = \frac{\mathrm{d}r^{(s)}}{\mathrm{d}R^{(s)}} \mathbf{e}_R \otimes \mathbf{e}_R + \frac{r^{(s)}}{R^{(s)}} \mathbf{e}_\theta \otimes \mathbf{e}_\theta + \frac{r^{(s)}}{R^{(s)}} \mathbf{e}_\varphi \otimes \mathbf{e}_\varphi, \tag{2.1}$$

where $r^{(s)}$ represents the radial coordinate of the bilayer gels in a swollen state. The principal stretches in the radial and hoop directions are, respectively, defined as

$$\lambda_R^{(s)} = \frac{\mathrm{d}r^{(s)}}{\mathrm{d}R^{(s)}}, \qquad \lambda_\theta^{(s)} = \lambda_\varphi^{(s)} = \frac{r^{(s)}}{R^{(s)}}. \tag{2.2}$$

The incompressibility of all molecular constituents within the gel system yields a volumetric constraint wherein the total gel volume equals the sum of the dry polymer network volume and the volume of absorbed solvent molecules. This relationship can be mathematically expressed as

$$1 + vC^{(s)} = \det \mathbf{F}^{(s)} = J^{(s)}, \tag{2.3}$$

where v is the volume per solvent molecule, and $C^{(s)}$ denotes the solvent concentration in gel s.

The swelling mechanics of this structure can be characterized as follows: near the core-gel interface, the rigid core constrains hoop direction swelling while permitting radial stretching. Due to the dissimilar micromaterial parameters of gel 1 and gel 2, their respective swelling behaviors differ significantly, generating interfacial forces between the two layers. These forces either promote separation or cohesion between the gels. However, since the two gel layers are perfectly bonded, they must accommodate each other's deformation, maintaining identical radial displacement magnitudes at their interface. Phenomena such as asymmetric deformations, interfacial debonding, and fracture are beyond the scope of the current research.

In the absence of body forces, the conservation of linear momentum reduces to the equilibrium equations:

$$\mathbf{P}^{(s)} \cdot \nabla = \mathbf{0}, \tag{2.4}$$

where $\mathbf{P}^{(s)}$ represents the nominal stress tensor, also known as the first Piola–Kirchhoff stress tensor.

The nominal stress tensor in each gel layer, expressed in the spherical coordinate system, takes the form:

$$\mathbf{P}^{(s)} = P_R^{(s)} \mathbf{e}_R \otimes \mathbf{e}_R + P_\theta^{(s)} \mathbf{e}_\theta \otimes \mathbf{e}_\theta + P_\varphi^{(s)} \mathbf{e}_\varphi \otimes \mathbf{e}_\varphi. \tag{2.5}$$

Upon substitution of Eq. (2.5) into the equilibrium equation (2.4) and simplification, we obtain the governing differential equation:

$$\frac{\mathrm{d}P_R^{(s)}}{\mathrm{d}R^{(s)}} + \frac{2}{R^{(s)}} \left(P_R^{(s)} - P_\theta^{(s)} \right) = 0. \tag{2.6}$$

Under the assumption of spherically symmetric deformations and perfectly bonded interfaces between the core-gel and gel-gel, the boundary conditions can be formulated as

$$\lambda_\theta^{(1)}(R_{\mathrm{in}}) = 1, \qquad P_R^{(2)}(R_{\mathrm{out}}) = 0, \tag{2.7}$$

including the following interface continuity conditions:

$$P_R^{(1)}(R_{\mathrm{inter}}) = P_R^{(2)}(R_{\mathrm{inter}}), \qquad \lambda_\theta^{(1)}(R_{\mathrm{inter}}) = \lambda_\theta^{(2)}(R_{\mathrm{inter}}). \tag{2.8}$$

2.2. Constitutive equations

Let $W^{(s)}$ denote the Helmholtz free energy density of the gel s. Assuming the gel s is in equilibrium state characterized by the displacement field $\boldsymbol{\chi}^{(s)}$ and solvent concentration field $C^{(s)}$,

thermodynamic principles stipulate that the variation in the gel's free energy must equate to the work exerted by external mechanical force and solvent, as encapsulated by

$$\int_{B^{(s)}} \delta W^{(s)} \, \mathrm{d}V = \int_{\partial B^{(s)}} \mathbf{P}^{(s)} \mathbf{N}^{(s)} \delta \boldsymbol{\chi}^{(s)} \, \mathrm{d}A + \mu \int_{B^{(s)}} \delta C^{(s)} \, \mathrm{d}V, \tag{2.9}$$

where $\mathbf{N}^{(s)}$ denotes the unit vector normal to the boundary $\partial B^{(s)}$ of the reference configuration $B^{(s)}$.

Under the assumption that the free energy density function $W^{(s)}$ depends on the deformation gradient $\mathbf{F}^{(s)}$ and solvent concentration $C^{(s)}$, applying the divergence theorem to Eq. (2.9) yields:

$$\int_{B^{(s)}} \left(\frac{\partial W^{(s)}}{\partial \mathbf{F}^{(s)}} - \mathbf{P}^{(s)} \right) : \delta \mathbf{F}^{(s)} \, \mathrm{d}V + \int_{B^{(s)}} \left(\mathbf{P}^{(s)} \cdot \nabla \right) \delta \boldsymbol{\chi}^{(s)} \, \mathrm{d}V + \int_{B^{(s)}} \left(\frac{\partial W^{(s)}}{\partial C^{(s)}} - \mu \right) \delta C^{(s)} \, \mathrm{d}V = 0. \tag{2.10}$$

The middle term in Eq. (2.10) vanishes upon application of the equilibrium Eq. (2.4). Consequently, Eq. (2.10) boils down to the constitutive equations:

$$\frac{\partial W^{(s)}}{\partial \mathbf{F}^{(s)}} = \mathbf{P}^{(s)}, \qquad \frac{\partial W^{(s)}}{\partial C^{(s)}} = \mu. \tag{2.11}$$

Following Flory and Rehner (1943), the Helmholtz free energy of the gel takes the form:

$$W^{(s)} = W^{(s)}_{\mathrm{mix}} + W^{(s)}_{\mathrm{str}}, \tag{2.12}$$

where $W^{(s)}_{\mathrm{mix}}$ arises from mixing the polymers with the solvent molecules and $W^{(s)}_{\mathrm{str}}$ from stretching the gel network.

Flory (1942) and Huggins (1941) developed the expression for the free energy of mixing:

$$W^{(s)}_{\mathrm{mix}} = -\frac{kT}{v} \left(v C^{(s)} \ln \left(1 + \frac{1}{v C^{(s)}} \right) + \frac{\chi}{1 + v C^{(s)}} \right), \tag{2.13}$$

where χ represents a dimensionless parameter quantifying the enthalpy of mixing and kT the temperature in the unit of energy. For good solvents, the parameter χ typically falls within the range of 0.1 to 0.5. In our subsequent numerical calculations, we will set $\chi = 0.1$.

Including the molecular incompressibility constraint, the free energy of mixing can be reformulated as

$$W^{(s)}_{\mathrm{mix}} = -\frac{kT}{v} \left[(J^{(s)} - 1) \log \frac{J^{(s)}}{J^{(s)} - 1} + \frac{\chi}{J^{(s)}} \right]. \tag{2.14}$$

Taking into account the effect of polymer chain entanglements (Edwards & Vilgis, 1986), the Helmholtz free energy contribution attributable to the stretching of the network is formulated as

$$\begin{aligned} W^{(s)}_{\mathrm{str}} = {} & \frac{1}{2} N^{(s)}_s kT \ln \left(1 - \left(\alpha^{(s)} \right)^2 \sum \left(\lambda^{(s)}_i \right)^2 \right) \\ & + \frac{1}{2} N^{(s)}_c kT \left[\frac{\left(1 - \left(\alpha^{(s)} \right)^2 \right) \sum \left(\lambda^{(s)}_i \right)^2}{1 - \left(\alpha^{(s)} \right)^2 \sum \left(\lambda^{(s)}_i \right)^2} + \ln \left(1 - \left(\alpha^{(s)} \right)^2 \sum \left(\lambda^{(s)}_i \right)^2 \right) \right] \\ & + \frac{1}{2} N^{(s)}_s kT \sum \left\{ \frac{\left(\lambda^{(s)}_i \right)^2 \left(1 + \eta^{(s)} \right) \left(1 - \left(\alpha^{(s)} \right)^2 \right)}{\left(1 + \eta^{(s)} \left(\lambda^{(s)}_i \right)^2 \right) \left(1 - \left(\alpha^{(s)} \right)^2 \sum \left(\lambda^{(s)}_i \right)^2 \right)} + \ln \left(1 + \eta^{(s)} \left(\lambda^{(s)}_i \right)^2 \right) \right\}, \end{aligned} \tag{2.15}$$

where $N_c^{(s)}$ and $N_s^{(s)}$ denote the crosslink and slip-link concentrations, respectively, $\alpha^{(s)}$ characterizes the inextensibility parameter, $\eta^{(s)}$ is the slippage parameter, and $\lambda_i^{(s)}$ $(i = 1, 2, 3)$ represent the principal stretches.

Let $\mathbf{C^{(s)}} = \left(\mathbf{F}^{(s)}\right)^T \mathbf{F^{(s)}}$ be the right Cauchy–Green deformation tensor. The principal invariants of $\mathbf{C^{(s)}}$ can be written as

$$\begin{aligned} I_1^{(s)} &= \left(\lambda_1^{(s)}\right)^2 + \left(\lambda_2^{(s)}\right)^2 + \left(\lambda_3^{(s)}\right)^2, \\ I_2^{(s)} &= \left(\lambda_1^{(s)}\right)^2 \left(\lambda_2^{(s)}\right)^2 + \left(\lambda_2^{(s)}\right)^2 \left(\lambda_3^{(s)}\right)^2 + \left(\lambda_3^{(s)}\right)^2 \left(\lambda_1^{(s)}\right)^2, \\ I_3^{(s)} &= \left(\lambda_1^{(s)}\right)^2 \left(\lambda_2^{(s)}\right)^2 \left(\lambda_3^{(s)}\right)^2 = \left(J^{(s)}\right)^2. \end{aligned} \tag{2.16}$$

Combining Eqs. (2.15) and (2.16) yields

$$\begin{aligned} W_{\mathrm{str}}^{(s)}\left(I_1^{(s)}, I_2^{(s)}, J^{(s)}\right) &= \frac{1}{2} N_c^{(s)} kT \left[\frac{(1-(\alpha^{(s)})^2) I_1^{(s)}}{1-(\alpha^{(s)})^2 I_1^{(s)}} + \ln(1-(\alpha^{(s)})^2 I_1^{(s)})\right] \\ &+ \frac{1}{2} N_s^{(s)} kT \ln\left(\left(1+\eta^{(s)} I_1^{(s)} + (\eta^{(s)})^2 I_2^{(s)} + (\eta^{(s)})^3 (J^{(s)})^2\right)\left(1-(\alpha^{(s)})^2 I_1^{(s)}\right)\right] \\ &+ \frac{1}{2} N_s^{(s)} kT \left[\left(\frac{I_1^{(s)} + 2\eta^{(s)} I_2^{(s)} + 3(\eta^{(s)})^2 (J^{(s)})^2}{1+\eta^{(s)} I_1^{(s)} + (\eta^{(s)})^2 I_2^{(s)} + (\eta^{(s)})^3 (J^{(s)})^2}\right)\left(\frac{\left(1+\eta^{(s)}\right)\left(1-(\alpha^{(s)})^2\right)}{1-(\alpha^{(s)})^2 I_1^{(s)}}\right)\right]. \end{aligned} \tag{2.17}$$

Applying the Legendre transformation to the Helmholtz free energy yields

$$\widehat{W}^{(s)} = W^{(s)} - \mu C^{(s)}. \tag{2.18}$$

Thus, the constitutive Eqs. (2.11) can be rewritten as

$$\mathbf{P}^{(s)} = \frac{\partial \widehat{W}^{(s)}}{\partial \mathbf{F}^{(s)}}, \qquad C^{(s)} = -\frac{\partial \widehat{W}^{(s)}}{\partial \mu}. \tag{2.19}$$

By setting the chemical potential to zero and integrating Eqs. (2.18) and (2.19), we obtain

$$\begin{aligned} \mathbf{P}^{(s)} &= \frac{\partial \widehat{W}^{(s)}}{\partial \mathbf{F}^{(s)}} = \frac{\partial \widehat{W}^{(s)}}{\partial I_1^{(s)}} \frac{\partial I_1^{(s)}}{\partial \mathbf{C}^{(s)}} : \frac{\partial \mathbf{C}^{(s)}}{\partial \mathbf{F}^{(s)}} + \frac{\partial \widehat{W}^{(s)}}{\partial I_2^{(s)}} \frac{\partial I_2^{(s)}}{\partial \mathbf{C}^{(s)}} : \frac{\partial \mathbf{C}^{(s)}}{\partial \mathbf{F}^{(s)}} + \frac{\partial \widehat{W}^{(s)}}{\partial J^{(s)}} \frac{\partial J^{(s)}}{\partial \mathbf{F}^{(s)}} \\ &= 2\left[\frac{\partial \widehat{W}^{(s)}}{\partial I_1^{(s)}} \mathbf{F}^{(s)} + \frac{\partial \widehat{W}^{(s)}}{\partial I_2^{(s)}} \left(I_1^{(s)} \mathbf{F}^{(s)} - \mathbf{F}^{(s)} (\mathbf{C}^{(s)})^T\right) + \frac{\partial \widehat{W}^{(s)}}{\partial J^{(s)}} \frac{1}{2} J^{(s)} (\mathbf{F}^{(s)})^{-T}\right]. \end{aligned} \tag{2.20}$$

3. Physics-informed neural networks

As shown in Fig. 2, two DNNs serve as ansatz functions to approximate the stretch fields within the bilayer gel system. The input layer receives position coordinates $R^{(s)}$, while the output layer yields the corresponding radial and hoop stretches, $\lambda_R^{(s)}$ and$\lambda_\theta^{(s)}$, respectively (without causing notational ambiguity, we still use the notations $\lambda_R^{(s)}$ and $\lambda_\theta^{(s)}$ to represent their DNN ansatzes in this section).

Each DNN architecture incorporates six hidden layers, with each layer containing 20 neurons and employing hyperbolic tangent activation functions. The output layer utilizes linear activation

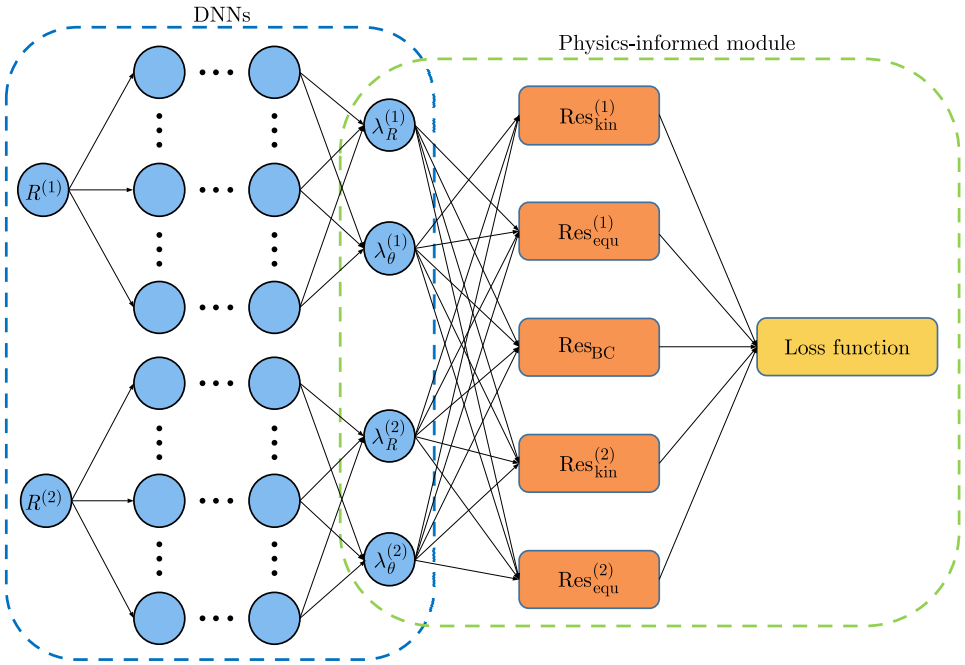

Fig. 2. Architecture of PINNs composed of DNNs and physics-informed module.

to ensure unbounded stretch predictions. Denoting the s-th DNN system as $\mathcal{N}^{(s)}$, the primary field variables (solutions) of the mechanical problem are expressed as

$$\left[\lambda_R^{(s)}, \lambda_\theta^{(s)}\right]^T = \mathcal{N}^{(s)}\left(R^{(s)}; \mathbf{W}^{(s)}\right), \tag{3.1}$$

where $\mathbf{W}^{(s)}$ represents the collection of trainable weights and biases associated with the s-th DNN.

The residual terms for the kinematic relations and equilibrium equations are formulated as

$$\begin{aligned} \mathrm{Res}_{\mathrm{kin}}^{(s)} &= \lambda_R^{(s)} - \lambda_\theta^{(s)} - R^{(s)} \frac{\mathrm{d}\lambda_\theta^{(s)}}{\mathrm{d}R^{(s)}}, \\ \mathrm{Res}_{\mathrm{equ}}^{(s)} &= \frac{\mathrm{d}P_R^{(s)}}{\mathrm{d}R^{(s)}} + \frac{2}{R^{(s)}}\left(P_R^{(s)} - P_\theta^{(s)}\right), \end{aligned} \tag{3.2}$$

where the stress components $P_R^{(s)}$ and $P_\theta^{(s)}$ are determined by substituting the DNN predictions $\lambda_R^{(s)}$ and $\lambda_\theta^{(s)}$ into the constitutive relations. The spatial derivatives of the DNN predictions are computed using automatic differentiation capabilities within the TensorFlow framework.

In conventional supervised learning paradigms, prediction accuracy is fundamentally constrained by training data availability. To mitigate this limitation, physics-informed approaches have been developed that incorporate governing physical laws as constraints. These constraints are enforced through penalty terms in the loss function, which regularize the solution by penalizing predictions that violate fundamental physical principles.

The physics-informed module in Fig. 2 systematically encodes prior knowledge, including kinematic relations, equilibrium equations, and boundary conditions, into the composite loss function:

$$\mathrm{Loss} = \mathrm{Loss}_{\mathrm{kin}}^{(1)} + \mathrm{Loss}_{\mathrm{equ}}^{(1)} + \mathrm{Loss}_{\mathrm{kin}}^{(2)} + \mathrm{Loss}_{\mathrm{equ}}^{(2)} + \mathrm{Loss}_{\mathrm{BC}}, \tag{3.3}$$

where $\mathrm{Loss}_{\mathrm{kin}}^{(s)}$ and $\mathrm{Loss}_{\mathrm{equ}}^{(s)}$ represent loss contributions from kinematic relations and equilibrium equations for the s-th gel layer, respectively, and $\mathrm{Loss}_{\mathrm{BC}}$ encompasses boundary condition constraints, including interface continuity requirements. The conventional numerical methods

encounter considerable inconvenience in handling these interface continuity conditions. In the present work, these conditions are directly encoded into the physics-informed neural network (PINN) framework, thereby transferring the complexities to the process of minimizing the associated loss function.

The individual loss terms are evaluated using mean square error formulations:

$$\begin{aligned}
\mathrm{Loss}_{\mathrm{kin}}^{(s)} &= \frac{1}{N^{(s)}}\sum_{i=1}^{N^{(s)}}\left|\mathrm{Res}_{\mathrm{kin}}^{(s)}(R_i^{(s)};\mathbf{W}^{(s)})\right|^2,\\
\mathrm{Loss}_{\mathrm{geo}}^{(s)} &= \frac{1}{N^{(s)}}\sum_{i=1}^{N^{(s)}}\left|\mathrm{Res}_{\mathrm{geo}}^{(s)}(R_i^{(s)};\mathbf{W}^{(s)})\right|^2,\\
\mathrm{Loss}_{\mathrm{BC}} &= \left|\lambda_\theta^{(1)}(R_{\mathrm{in}})-1\right|^2+\left|P_R^{(2)}(R_{\mathrm{out}})\right|^2+\left|P_R^{(1)}(R_{\mathrm{inter}})-P_R^{(2)}(R_{\mathrm{inter}})\right|^2\\
&\quad+\left|\lambda_\theta^{(1)}(R_{\mathrm{inter}})-\lambda_\theta^{(2)}(R_{\mathrm{inter}})\right|^2,
\end{aligned}\tag{3.4}$$

where $\left\{R_i^{(s)}\right\}_{i=1}^{N^{(s)}}$ denotes the set of collocation points for training the s-th neural network.

The composite loss function is minimized using the Adam optimization algorithm, a gradient-based adaptive learning rate method implemented within the TensorFlow computational environment. During the training process, primary variables $\lambda_R^{(s)}$ and $\lambda_\theta^{(s)}$ that deviate from prescribed physical constraints are penalized, thereby guiding the DNN approximations toward physically consistent results. This approach ultimately yields DNN-based solutions that satisfy the underlying physics constraints.

To enable a comparison with the PINN result, we computed a classical numerical solution using the shooting method. In the absence of entanglements ($N_s^{(s)} = \alpha^{(s)} = \eta^{(s)} = 0$), we set $vN_c^{(1)} = 0.009$ and $vN_c^{(2)} = 0.001$. We initially assume $\lambda_R^{(1)}(R_{\mathrm{in}}) = x$. Combined with the boundary condition $r^{(1)}(R_{\mathrm{in}}) = R_{\mathrm{in}}$, we solve Eq. (2.6) for $s = 1$. The solution yields $r^{(2)}(R_{\mathrm{inter}})$, which is equal to $r^{(1)}(R_{\mathrm{inter}})$. Combined with $P_R^{(2)}(R_{\mathrm{out}}) = 0$, we then solve Eq. (2.6) for $s = 2$. Finally, a root-finding algorithm adjusts the initial assumption x until the interface pressure mismatch $P_R^{(1)}(R_{\mathrm{inter}}) - P_R^{(2)}(R_{\mathrm{inter}})$ is minimized. As shown in Fig. 3, the shooting method results demonstrate good agreement with the PINN predictions.

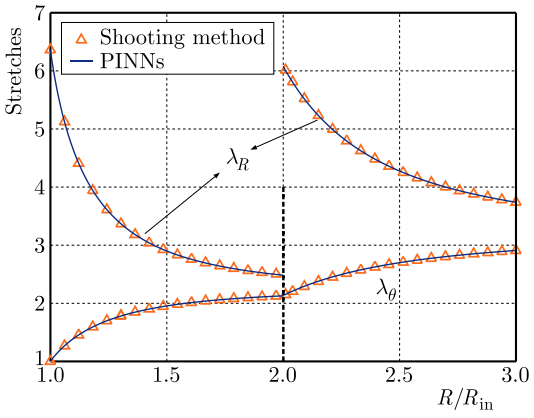

Fig. 3. Comparison of results obtained using PINNs and the shooting method.

4. Results and discussion

In this section, PINNs are employed to investigate the influence of micromaterial parameters on the inhomogeneous deformation, stress distribution, and solvent concentration in dual-layer spherical gels at equilibrium.

To examine the effect of slip-links, we maintain constant total concentrations of cross-links and slip-links in both gel layers, such that $vN_s^{(s)} + vN_c^{(s)} = 0.01$ for $s = 1, 2$, while varying the slip-link fraction defined as $\mathcal{K}^{(s)} = N_s^{(s)}/(N_s^{(s)} + N_c^{(s)})$. The inextensibility and slippage parameters are held constant at $\alpha^{(s)} = 0.1$ and $\eta^{(s)} = 0.1$ for $s = 1, 2$, respectively. Figure 4 illustrates the effects of the slip-link fraction on the radial and hoop stretches and normalized stresses when the dual-layer gels reach equilibrium. When the slip-link fractions in both layers are equal ($\mathcal{K}^{(1)} = \mathcal{K}^{(2)}$), the dual-layer system reduces to a single gel layer case, resulting in smooth stretch and stress functions. The upper panels of Fig. 4 demonstrate that near the rigid core, the hoop stretch remains constant due to core constraints, while the radial stretch increases substantially. With increasing distance from the core, the hoop and radial stretches converge. Moreover, the increasing slip-link fraction enhances both radial and hoop stretches. The lower panels reveal that near the core, the radial stress is tensile and the hoop stress is compressive due to core constraints. Both stresses diminish toward the outer surface, and their magnitudes decrease with the increasing slip-link fraction. When the slip-link fractions differ between layers ($\mathcal{K}^{(1)} \neq \mathcal{K}^{(2)}$), the behavior changes markedly. The radial stretch function exhibits discontinuity at the gel-gel interface (vertical dashed line in Fig. 4), whereas the hoop stretch function remains continuous owing to perfect bonding between the two gel layers. Nevertheless, the hoop stretch function becomes non-smooth at this interface. For systems with higher slip-link fractions in the outer layer ($\mathcal{K}^{(1)} = 0.1$, $\mathcal{K}^{(2)} = 0.9$), the radial stretch decreases with dimensionless radius R/R_{in} in gel 1, then exhibits a sudden discontinuous increase at the interface, before decreasing again. The hoop stretch increases with R/R_{in} in gel 1 and continues growing at an accelerated rate beyond the interface. Conversely, for systems with lower slip-link fractions in the outer layer ($\mathcal{K}^{(1)} = 0.9$, $\mathcal{K}^{(2)} = 0.1$), the radial stretch decreases with R/R_{in} in gel 1, then undergoes a discontinuous decrease at the interface followed by slight recovery. The hoop stretch increases

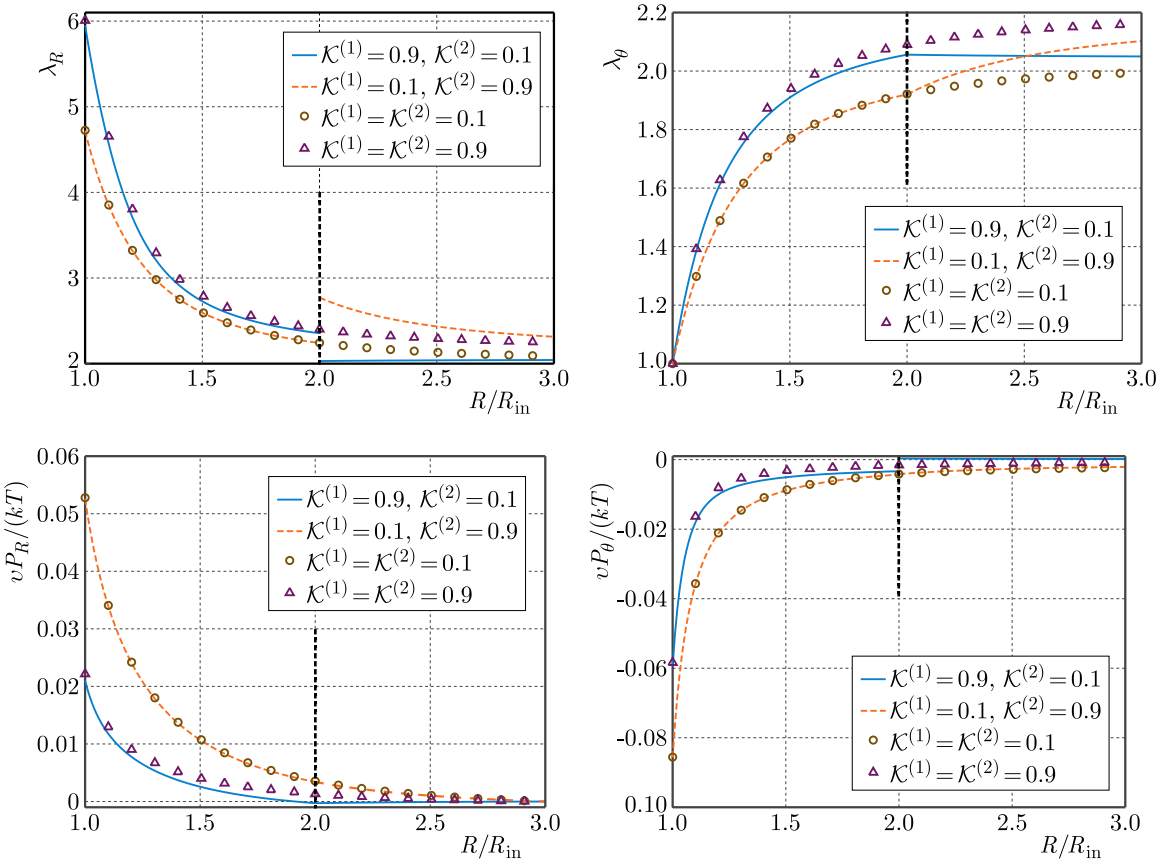

Fig. 4. Effects of slip-link fraction on the stretches (upper panels) and normalized stresses (lower panels) with $\alpha^{(s)} = 0.1$ and $\eta^{(s)} = 0.1$ for $s = 1, 2$.

with R/R_{in} in gel 1 but decreases beyond the interface. The stress distributions show distinct patterns. For $\mathcal{K}^{(1)} = 0.9$, $\mathcal{K}^{(2)} = 0.1$, the radial stress decreases with R/R_{in} in gel 1, transitions from tensile to compressive at the interface, then increases to zero at the outer surface. The hoop stress increases with R/R_{in} in gel 1, discontinuously changes from compressive to tensile at the interface, then decreases to zero at the outer surface. For $\mathcal{K}^{(1)} = 0.1$, $\mathcal{K}^{(2)} = 0.9$, both stress functions nearly coincide with the $\mathcal{K}^{(1)} = \mathcal{K}^{(2)} = 0.1$ case. Notably, the outer layer with a lower slip-link fraction exerts greater influence on the inner layer. Both stretch and stress functions in gel 1 show closer correspondence between cases $\mathcal{K}^{(1)} = 0.1$, $\mathcal{K}^{(2)} = 0.9$, and $\mathcal{K}^{(1)} = \mathcal{K}^{(2)} = 0.1$ compared to cases $\mathcal{K}^{(1)} = 0.9$, $\mathcal{K}^{(2)} = 0.1$, and $\mathcal{K}^{(1)} = \mathcal{K}^{(2)} = 0.9$.

The effects of the inextensibility parameter on mechanical behavior are opposite to those of the slippage parameter, as demonstrated in Fig. 5 and Fig. 6. Increasing the inextensibility parameter reduces stretches while amplifying stress magnitudes. Conversely, increasing the slippage parameter enhances stretches and diminishes stress magnitudes. Differences in inextensibility and slippage parameters between gel layers induce abrupt changes at the gel-gel interface. The upper panels of Figs. 5 and 6 reveal that dual-layer gel systems with lower inextensibility parameters or higher slippage parameters exhibit a sudden discontinuous increase in radial stretch at the interface, followed by a subsequent decrease, while the hoop stretch demonstrates accelerated growth beyond the interface. In contrast, systems with higher inextensibility parameters or lower slippage parameters display a sudden discontinuous decrease in radial stretch at the interface before recovery, accompanied by reduced hoop stretch beyond the interface. The lower panels of Fig. 5 and Fig. 6 reveal that gel systems with softer inner layers (characterized by lower inextensibility parameters or higher slippage parameters) exhibit a transition from tensile to compressive radial stress and from compressive to tensile hoop stress at the gel-gel interface. This behavior arises from the constraint imposed by the stiffer outer layer on the deformation

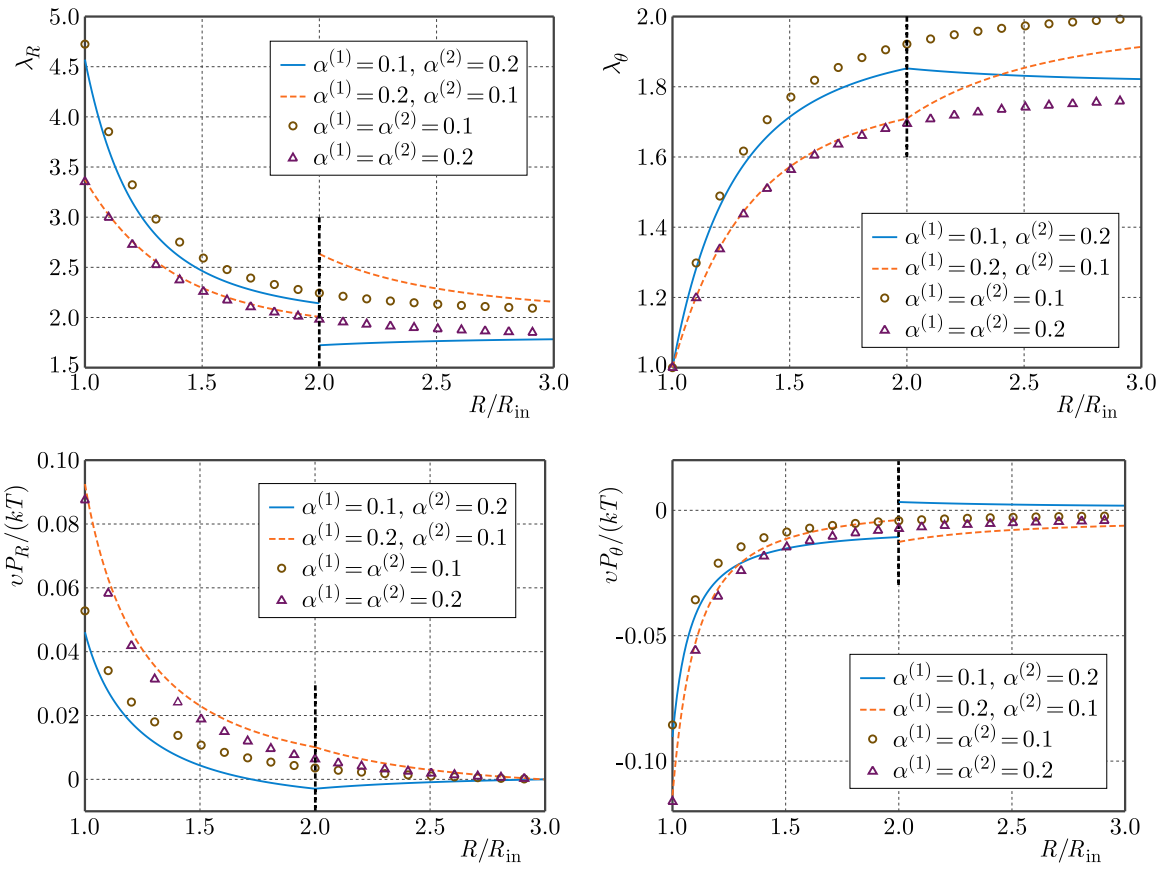

Fig. 5. Effects of inextensibility parameter on the stretches (upper panels) and normalized stresses (lower panels) with $\mathcal{K}^{(s)} = 0.1$ and $\eta^{(s)} = 0.1$ for $s = 1, 2$.

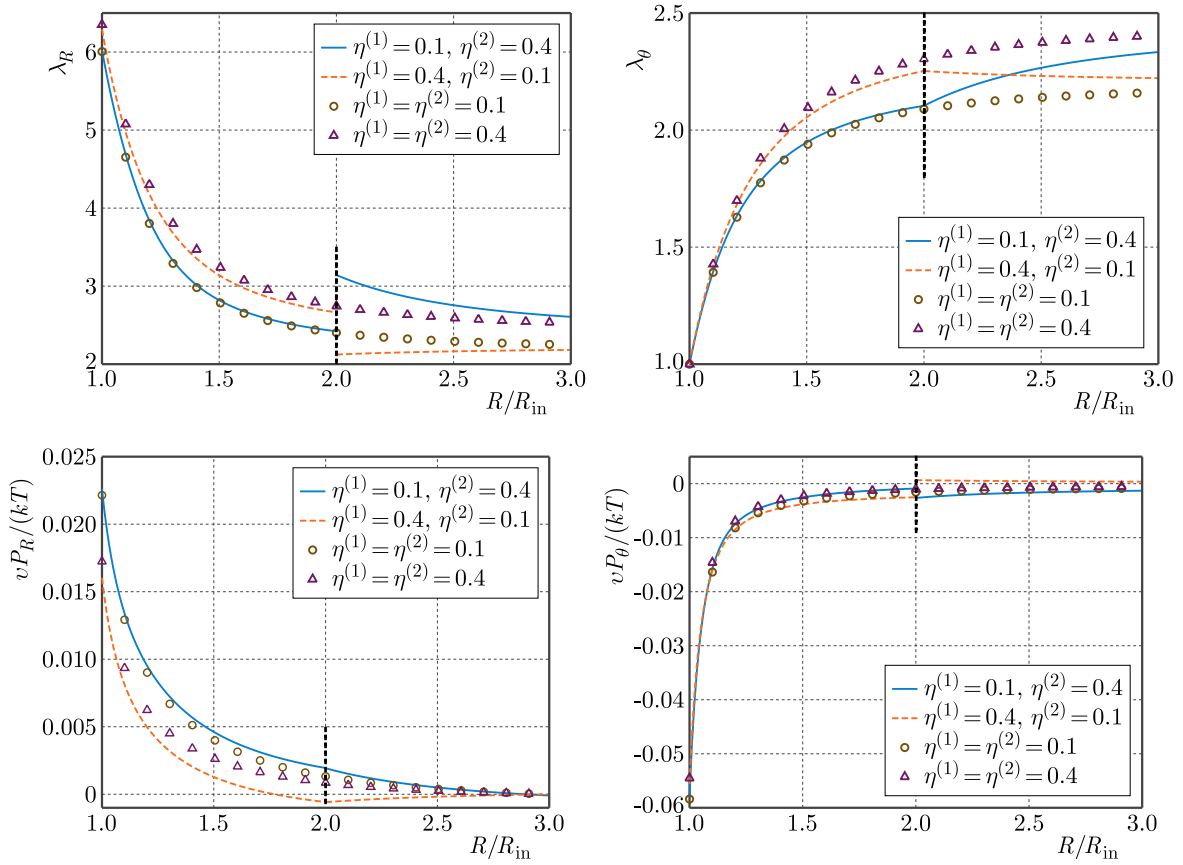

Fig. 6. Effects of slippage parameter on the stretches (upper panels) and normalized stresses (lower panels) with $\mathcal{K}^{(s)} = 0.9$ and $\alpha^{(s)} = 0.05$ for $s = 1, 2$.

of the softer inner layer. Conversely, systems with softer outer layers demonstrate an abrupt reduction in tensile radial stress and a sudden increase in compressive hoop stress, attributed to the enhanced deformation capacity of the softer outer layer. Both radial and hoop stresses approach to zero at the outer surface.

Figure 7 demonstrates the influence of micromaterial parameters on the solvent concentration distribution and equilibrium outer radius of the gel system. The left panels reveal that due to core constraints, solvent concentration increases with the distance from the core. The solvent concentration exhibits direct proportionality to the slip-link fraction and slippage parameter, while demonstrating inverse proportionality to the inextensibility parameter. Dual-layer gel systems with softer outer layers exhibit discontinuous increases in solvent concentration at the gel-gel interface, whereas systems with stiffer outer layers display the opposite behavior.

The equilibrium outer radius is crucial for various applications. We maintain a constant total thickness of the dual-layer gel, $(R_{\text{out}} - R_{\text{in}})/R_{\text{in}} = 2$, while varying the thickness ratio of the inner and outer layers, $\delta^{(1)}/\delta^{(2)}$, where $\delta^{(s)}$ represents the thickness of the s-th layer. The equilibrium outer radius is plotted as a function of the thickness ratio in the right panels of Fig. 7.

When micromaterial parameters are identical in both layers, the dual-layer gel system reduces to a single-layer gel system, and varying the thickness ratio does not affect the outer radius since the total thickness remains constant. Larger slip-link fractions and slippage parameters result in greater gel swelling, while the inextensibility parameter exhibits the opposite effect. For systems with softer inner layers, the outer radius increases with the thickness ratio, whereas systems with softer outer layers demonstrate the opposite trend. The variation range of the outer radius in dual-layer gel systems does not exceed that of single-layer gel systems. As the thickness ratio increases, the outer radius of dual-layer gel systems approaches that of the corresponding single-layer gel system.

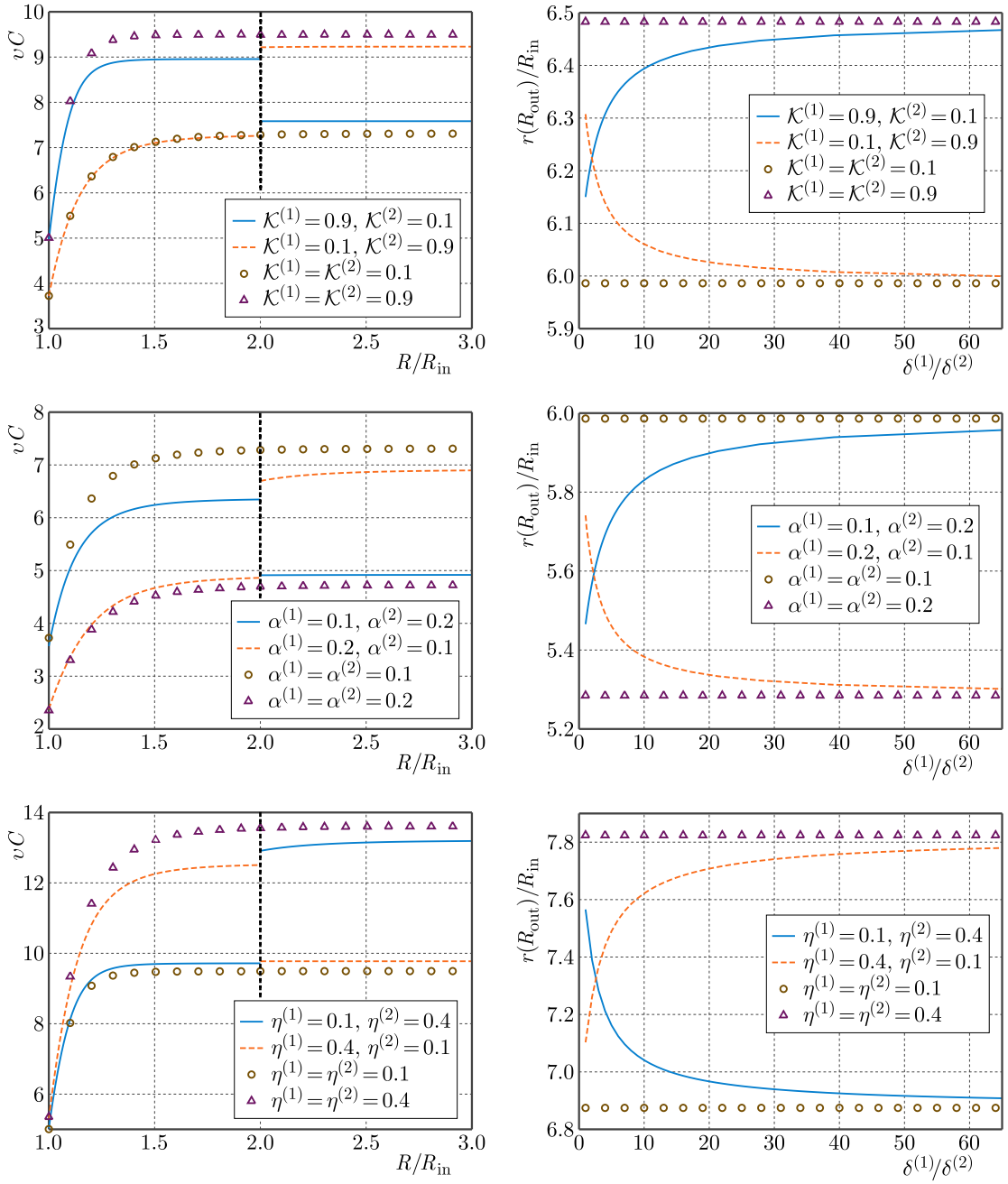

Fig. 7. Effects of slip-link fraction (upper panels, $\alpha^{(s)} = 0.1$ and $\eta^{(s)} = 0.1$ for $s = 1, 2$), inextensibility parameter (middle panels, $\mathcal{K}^{(s)} = 0.1$ and $\eta^{(s)} = 0.1$ for $s = 1, 2$), and slippage parameter (lower panels, $\mathcal{K}^{(s)} = 0.9$ and $\alpha^{(s)} = 0.05$ for $s = 1, 2$) on the distribution of solvent concentration (left panels) and outer radius of the gel system in equilibrium state (right panels).

5. Conclusion

This investigation presents a comprehensive theoretical and computational framework for analyzing the inhomogeneous swelling behavior of dual-layer spherical gels containing rigid cores. By incorporating the Edwards–Vilgis slip-link model, we successfully capture chain entanglement effects that are ubiquitous in actual gel networks but neglected by traditional Neo–Hookean formulations. The developed PINN methodology transforms the computational challenges of interface continuity conditions into an optimization problem, eliminating the need for iterative coupling procedures typically associated with interface problems, presenting a potentially more efficient computational paradigm for multi-domain or multi-physics applications.

Our systematic parametric analysis reveals that micromaterial parameters significantly influence mechanical behavior, stress distribution, and solvent concentration profiles. Notably, parameter disparities between gel layers induce discontinuous radial stretch distributions while maintaining interface continuity for hoop stretches. The outer layer exerts dominant influence on the inner layer's mechanical response. These findings establish a rigorous foundation for rational design and optimization of dual-layer gel systems, enabling precise control over target solvent concentrations, stress distributions, and equilibrium outer radii in dual-layer spherical gel systems. The framework advances fundamental understanding of dual-layer gel mechanics while providing practical tools for engineering applications in sensors, actuators, and drug delivery systems.

Acknowledgments

This work was supported by the National Science Foundation of China (12001172), the Natural Science Foundation of Fujian Province (2023J011031) and Joint Fund for Scientific and Technological Research and Development Plan in Henan Province (242103810029).

References

1. Abdolahi, J., Baghani, M., Arbabi, N., & Mazaheri, H. (2017). Finite bending of a temperature-sensitive hydrogel tri-layer: An analytical and finite element analysis. *Composite Structures*, *164*, 219–228. https://doi.org/10.1016/j.compstruct.2016.12.063
2. Ahmadi, M., Zholobko, O., & Wu, X.-f. (2020). Inhomogeneous swelling behavior of a bi-layered spherical hydrogel containing a hard core. *Journal of Applied Physics*, *128*(4), Article 044703. https://doi.org/10.1063/5.0016112
3. Ballauff, M., & Lu, Y. (2007). "Smart" nanoparticles: Preparation, characterization and applications. *Polymer*, *48*(7), 1815–1823. https://doi.org/10.1016/j.polymer.2007.02.004
4. Chester, S.A., & Anand, L. (2010). A coupled theory of fluid permeation and large deformations for elastomeric materials. *Journal of the Mechanics and Physics of Solids*, *58*(11), 1879–1906. https://doi.org/10.1016/j.jmps.2010.07.020
5. Diao, Y., Yang, J., Zhang, Y., Zhang, D., & Du, Y. (2023). Solving multi-material problems in solid mechanics using physics-informed neural networks based on domain decomposition technology. *Computer Methods in Applied Mechanics and Engineering*, *413*, Article 116120. https://doi.org/10.1016/j.cma.2023.116120
6. Edwards, S.F., & Vilgis, Th. (1986). The effect of entanglements in rubber elasticity. *Polymer*, *27*(4), 483–492. https://doi.org/10.1016/0032-3861(86)90231-4
7. Flory, P.J. (1942). Thermodynamics of high polymer solutions. *The Journal of Chemical Physics*, *10*(1), 51–61. https://doi.org/10.1063/1.1723621
8. Flory, P.J., & Rehner, J. (1943). Statistical mechanics of cross-linked polymer networks II. Swelling. *The Journal of Chemical Physics*, *11*(11), 521–526. https://doi.org/10.1063/1.1723792
9. Huggins, M.L. (1941). Solutions of long chain compounds. *The Journal of Chemical Physics*, *9*(5), 440. https://doi.org/10.1063/1.1750930
10. Jin, L., Xu, J., Xue, Y., Zhang, X., Feng, M., Wang, C., Yao, W., Wang, J., & He, M. (2021). Research progress in the multilayer hydrogels. *Gels*, *7*(4), Article 172. https://doi.org/10.3390/gels7040172
11. Khan, M.U.A., Stojanović, G.M., Abdullah, M.F.B., Dolatshahi-Pirouz, A., Marei, H.E., Ashammakhi, N., & Hasan, A. (2024). Fundamental properties of smart hydrogels for tissue engineering applications: A review. *International Journal of Biological Macromolecules*, *254*(Part 3), Article 127882. https://doi.org/10.1016/j.ijbiomac.2023.127882
12. López-Díaz, A., Vázquez, A.S., & Vázquez, E. (2024). Hydrogels in soft robotics: Past, present, and future. *ACS Nano*, *18*(32), 20817–20826. https://doi.org/10.1021/acsnano.3c12200

13. Morimoto, T., & Ashida, F. (2015). Temperature-responsive bending of a bilayer gel. *International Journal of Solids and Structures*, *56–57*, 20–28. https://doi.org/10.1016/j.ijsolstr.2014.12.009

14. Raissi, M., Perdikaris, P., & Karniadakis, G.E. (2019). Physics-informed neural networks: A deep learning framework for solving forward and inverse problems involving nonlinear partial differential equations. *Journal of Computational Physics*, *378*, 686–707. https://doi.org/10.1016/j.jcp.2018.10.045

15. Su, H., Yan, H., Zhang, X., & Zhong, Z. (2022). Multiphysics-informed deep learning for swelling of pH/temperature sensitive cationic hydrogels and its inverse problem. *Mechanics of Materials*, *175*, Article 104498. https://doi.org/10.1016/j.mechmat.2022.104498

16. Su, H., Yan, H., & Zhong, Z. (2021). Deep neural networks for large deformation of photo-thermo-pH responsive cationic gels. *Applied Mathematical Modelling*, *100*, 549–563. https://doi.org/10.1016/j.apm.2021.08.013

17. Urayama, K., Kawamura, T., & Kohjiya, S. (2003). Multiaxial deformations of end-linked poly(dimethylsiloxane) networks. 4. Further assessment of the slip-link model for chain-entanglement effect on rubber elasticity. *The Journal of Chemical Physics*, *118*(12), 5658–5664. https://doi.org/10.1063/1.1555636

18. Wu, Z., & Zhong, Z. (2013). Inhomogeneous equilibrium swelling of core-shell-coating gels. *Soft Materials*, *11*(2), 215–220. https://doi.org/10.1080/1539445x.2012.617644

19. Yan, H., & Jin, B. (2012). Influence of microstructural parameters on mechanical behavior of polymer gels. *International Journal of Solids and Structures*, *49*(3–4), 436–444. https://doi.org/10.1016/j.ijsolstr.2011.10.026

20. Yan, K., Xu, F., Wei, W., Yang, C., Wang, D., & Shi, X. (2021). Electrochemical synthesis of chitosan/silver nanoparticles multilayer hydrogel coating with pH-dependent controlled release capability and antibacterial property. *Colloids and Surfaces B: Biointerfaces*, *202*, Article 111711. https://doi.org/10.1016/j.colsurfb.2021.111711

21. Yang, J., Bai, R., Chen, B., & Suo, Z. (2020). Hydrogel adhesion: A supramolecular synergy of chemistry, topology, and mechanics. *Advanced Functional Materials*, *30*(2), Article 1901693. https://doi.org/10.1002/adfm.201901693

22. Zhao, X., Hong, W., & Suo, Z. (2008). Inhomogeneous and anisotropic equilibrium state of a swollen hydrogel containing a hard core. *Applied Physics Letters*, *92*(5), Article 051904. https://doi.org/10.1063/1.2840158

23. Zhao, Y.-D., Lai, J.-H., & Wang, M. (2021). 4D printing of self-folding hydrogel tubes for potential tissue engineering applications. *Nano LIFE*, *11*(04), Article 2141001. https://doi.org/10.1142/s1793984421410014

Manuscript received August 10, 2025; accepted for publication December 9, 2025; published online February 26, 2026.

JOURNAL OF THEORETICAL
AND APPLIED MECHANICS
64, 1, pp. 71–84, Warsaw 2026
https://doi.org/10.15632/jtam-pl/216285

STUDY ON ROOF FRACTURE MECHANISM AND MINE PRESSURE CHARACTERISTICS IN PSEUDO-INCLINED WORKING FACES OF STEEPLY INCLINED COAL SEAMS

Jiadi YIN[1], Yu WU[1*], Yang HAO[1], Kangsheng XUE[1], Yan ZHANG[2], Hualei ZHANG[2]

[1] *State Key Laboratory of Intelligent Construction and Healthy Operation and Maintenance of Deep Underground Engineering, China University of Mining and Technology, Xuzhou, China*
[2] *Anhui University of Science and Technology, Huainan, China*

*corresponding author, *wuyu@cumt.edu.cn*

An improperly designed pseudo-inclination angle in steeply inclined coal seams can lead to coal wall spalling and hydraulic support failure. This study establishes mechanical models for initial and periodic roof fractures under pseudo-inclined mining and derives analytical solutions using the variational method. The optimal pseudo-inclination angle has been determined to be 5° to 10°. Field monitoring shows that initial fractures occur at the center of the working face, while periodic fractures originate in the upper-middle section, where support loads are also highest. These results validate the mechanical model and offer theoretical guidance for the safe mining of steeply inclined seams.

Keywords: steeply inclined coal seam; pseudo-inclined mining; rock layer failure; thin plate model; mining pressure patterns.

Articles in JTAM are published under Creative Commons Attribution 4.0 International.
Unported License https://creativecommons.org/licenses/by/4.0/deed.en.
By submitting an article for publication, the authors consent to the grant of the said license.

1. Introduction

Steeply inclined coal seams are widely distributed in western and central China, accounting for approximately 10 % to 20 % of the country's proven coal reserves (Wu *et al.*, 2020). Due to their large dip angles, these seams exhibit highly complex mining conditions and are recognized as a typical category of difficult-to-mine coal seams (Sun *et al.*, 2019). Under steeply inclined conditions, the downslope component of the gravitational force is enhanced, resulting in significant shear-induced strata sliding. This leads to pronounced asymmetry and unpredictability in roof fracture behavior, ground pressure evolution, and support system stability (Xie *et al.*, 2020). These complex mechanical responses directly influence the effectiveness of roof control, operational safety, and equipment adaptability. Therefore, elucidating the mechanisms governing roof fracture and pressure transmission in steeply inclined coal seams holds considerable theoretical and practical engineering significance.

International research, particularly in the United Kingdom, France, Germany, and Ukraine, began relatively early and focused on the characteristics of stress distribution and ground pressure evolution during mining in steeply inclined seams (Eremin *et al.*, 2022; Das *et al.*, 2017). These studies further promoted the development of fully mechanized mining technologies (Rak *et al.*, 2020; Kumar *et al.*, 2023; Çelik *et al.*, 2023; Das *et al.*, 2021), the design of specialized mining equipment (Proyavkin *et al.*, 1993; Islavath *et al.*, 2016; 2023), and detailed investigations into post-mining strata deformation and surface subsidence (Do *et al.*, 2017). In China, systematic research started in the 1990s and has since supported the transition from non-mechanized to fully mechanized longwall mining (Luo *et al.*, 2021; Tu *et al.*, 2015), resulting in extensive engineering experience and research achievements. Existing studies have revealed the temporal

sequence of roof fracture (Lang *et al.*, 2021), the non-uniformity of goaf filling – an effect that intensifies with an increasing dip angle and the resulting asymmetric deformation patterns and shell-like roof structures (Xie *et al.*, 2020). Ground pressure is particularly severe in the central region of the working face, while the roof weighting intervals vary along the inclination direction (Yang *et al.*, 2020). The asymmetric stress distribution and shear-dominated deformation tendencies predispose hydraulic supports to instability cases, such as sliding, tilting, reverse tilting, and torsion (Li *et al.*, 2017), thus further complicating mining operations. Consequently, flexible shield supports with enhanced anti-slip and anti-shear performance are more suitable for steeply inclined conditions (Zhao *et al.*, 2022), and lateral constraints must be provided during support movement to prevent instability (Wang *et al.*, 2016). To mitigate rock ejection and equipment sliding, a pseudo-inclined face layout has been increasingly adopted in steep seam mining (Pan *et al.*, 2017), resulting in a parallelogram-shaped rather than rectangular roof structure behind the working face. The selection of pseudo-inclination angle plays a critical role in roof control and the stability of the coal wall ahead of the face (Zhang *et al.*, 2025). However, current engineering practices rely mainly on numerical simulations and field experience, lacking a systematic theoretical framework.

In this study, a mechanical model of an elastic thin plate is established for the basic roof of a pseudo-inclined working face in steeply inclined coal seams. The deformation characteristics, principal stress distribution, and the spacing of initial and periodic roof fractures are systematically analyzed, and a rational range of pseudo-inclination angles is proposed. Theoretical results are validated using field monitoring data, providing a transferable theoretical basis and engineering reference for optimizing pseudo-inclined layout, predicting roof weighting behavior, and designing support parameters in steeply inclined coal seam longwall mining.

2. Geological background and technology synopsis

2.1. Geological background

The II4 mining area of the Taoyuan Coal Mine extends approximately 2200 meters along the strike, with a dip width ranging from 900 to 1500 meters, covering an area of about 2.5 km^2. The 1044 working face is located within the no. 10 coal seam in the II4 mining area, as depicted in Fig. 1a. The coal seam thickness varies between 3.2 and 4.2 meters, with a localized parting layer ranging from 0 to 0.23 meters. The coal seam dips at approximately 42°. The immediate roof comprises mudstone and fine sandstone, whereas the floor is predominantly composed of mudstone. The stratigraphic column of the coal seam is presented in Fig. 1b.

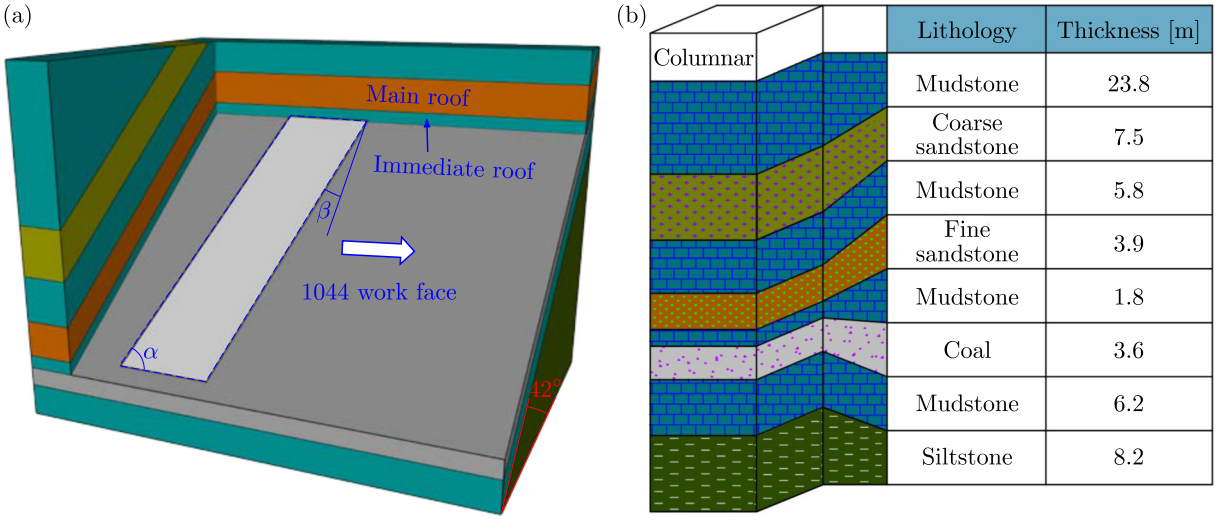

Lithology	Thickness [m]
Mudstone	23.8
Coarse sandstone	7.5
Mudstone	5.8
Fine sandstone	3.9
Mudstone	1.8
Coal	3.6
Mudstone	6.2
Siltstone	8.2

Fig. 1. Geological overview of Coal Mine.

2.2. Technology synopsis

When a steeply inclined working face is arranged along the dip direction of the coal seam, excessive inclination can cause the advancing conveyor and support movement, particularly the pushing of the conveyor to shift downward, creating challenges for coal mining operations (Zhao *et al.*, 2025). The primary issue is that extracted coal tends to slide freely along the coal seam floor, leading to the formation of flying gangue within the entire mining space, which poses significant safety hazards to both equipment and personnel. To address these issues, the 1044 working face adopts a pseudo-inclined layout with an inclination angle of β, as shown in Fig. 1a. This layout offers two key advantages. First, coal naturally slides along the coal wall, reducing potential damage to equipment and minimizing risks to personnel. Second, it leverages the spatial offset between adjacent supports to balance the upward movement caused by support advancement with the downward displacement due to the coal seam inclination, effectively mitigating equipment slippage during the support and conveyor advancement process.

In this working face, the caving method is employed, whereby the goaf is formed as the basic roof and the immediate roof naturally collapses with face advance, producing an accumulation of caved rock. In addition, several engineering measures have been incorporated to enhance equipment stability under mechanized mining conditions on steeply inclined seams. These include anti-slip structures on the bases of hydraulic supports, increased initial supporting force, lateral constraint devices between adjacent supports, and anti-slip control within the shearer traction system, all of which prevent sliding or rolling instability along the dip direction.

3. Mechanical mechanism of main roof fracture

3.1. Mechanical model of the initial fracture

When pseudo-inclined mining is applied to steeply inclined coal seams, as the working face advances, the main roof fails and collapses into the mined-out area, with the roof forming a parallelogram that hangs above the cavity. This leads to periodic deformations and failure. The main roof can be treated as a parallelogram plate for mechanical analysis. Prior to its first fracture, the main roof behaves as an elastically supported thin plate with four fixed edges. The load acting on the inclined plate is considered as the resultant of the normal and tangential forces from the overlying strata. As illustrated in Fig. 2a, the working face has a length of b and an advancement distance of a, with a roof thickness of h. The rock layer exhibits an inclination angle of θ, while the working face is oriented at an angle α relative to the horizontal plane. The pseudo-inclination angle of the working face is β. As shown in Fig. 2b, the boundaries of the working face are constrained on all four sides.

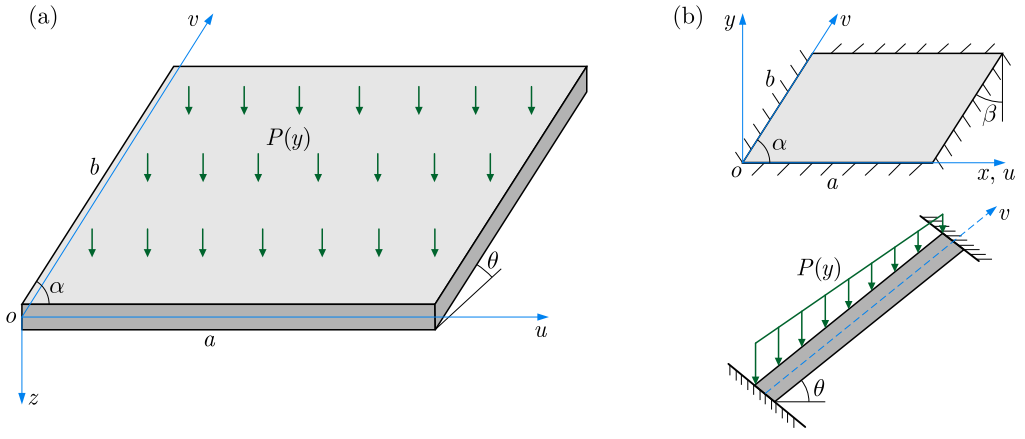

Fig. 2. Mechanical model of initial fracture.

The load function is given by:

$$P(y) = q_0 - ky. \tag{3.1}$$

In the equation, q_0 represents the load applied to the bottom of the main roof, and k is the load distribution coefficient.

The deformation of the parallelogram plate is solved using the Kantorovich approximation method (Wang, 1983). The coordinate transformation is as follows:

$$\begin{cases} u = x - y\cot\alpha, \\ v = y/\sin\alpha. \end{cases} \tag{3.2}$$

Let the deflection function of the roof deformation be denoted as $\omega_1(u, v)$. The strain energy of the main roof can be expressed as

$$U = \frac{D}{2}\iint\limits_S \left(\nabla^2 w_1\right)^2 \mathrm{d}x\,\mathrm{d}y = \frac{D}{2}\iint \frac{1}{\sin^3\alpha}\left[\frac{\partial^2\omega_1}{\partial u^2} - 2\cos\alpha\frac{\partial^2\omega_1}{\partial u\partial v} + \frac{\partial^2\omega_1}{\partial v^2}\right]^2 \mathrm{d}u\,\mathrm{d}v, \tag{3.3}$$

where D is the bending stiffness of the thin plate.

The work done by the load on the main roof is given by

$$W = \iint (q_0 - ky)\cos\theta\omega_1\,\mathrm{d}x\,\mathrm{d}y = \iint (q_0 - kv\sin\alpha)\sin\alpha\cos\theta\omega_1\,\mathrm{d}u\,\mathrm{d}v. \tag{3.4}$$

According to the principle of minimum potential energy, the functional is given by

$$\prod = U - W. \tag{3.5}$$

Let the beam function that satisfies the boundary conditions $v = 0$ and $v = b$ be

$$V = \frac{v^4}{b^4} - 2\frac{v^3}{b^3} + \frac{v^2}{b^2}. \tag{3.6}$$

By solving Eqs. (3.3), (3.4), (3.5), and (3.6) simultaneously, the following results can be obtained:

$$\begin{aligned} \prod = {} & \frac{D}{2}\frac{1}{\sin^3\alpha}\int_0^a \left(\frac{b}{630}U''^2 + \frac{8\cos^2\alpha}{105b}U'^2 + \frac{4}{5b^3}U^2 - \frac{4}{105b}UU''\right)\mathrm{d}u \\ & - \frac{2bq_0 - k\sin\alpha b^2}{60}\sin\alpha\cdot\cos\theta\int_0^a U\,\mathrm{d}u. \end{aligned} \tag{3.7}$$

The following can be derived from the Euler–Lagrange equation:

$$\frac{\partial\prod}{\partial U} - \frac{\mathrm{d}}{\mathrm{d}u}\frac{\partial\prod}{\partial U'} + \frac{\mathrm{d}^2}{\mathrm{d}u^2}\frac{\partial\prod}{\partial U''} = 0. \tag{3.8}$$

By simplifying the calculations, the following ordinary differential equation can be obtained:

$$b^4U'''' - 3(8 + 16\cos^2\alpha)b^2U'' + 504U = (42q_0 - 21k\sin\alpha b)\,b^4\sin^4\alpha\cdot\cos\theta/2/D. \tag{3.9}$$

The general solution of the ordinary differential equation is given by

$$\begin{aligned} U = {} & A_1\cosh\left(\eta\frac{u}{b}\right)\cos\left(\xi\frac{u}{b}\right) + A_2\sinh\left(\eta\frac{u}{b}\right)\sin\left(\xi\frac{u}{b}\right) + A_3\cosh\left(\eta\frac{u}{b}\right)\sin\left(\xi\frac{u}{b}\right) \\ & + A_4\sinh\left(\eta\frac{u}{b}\right)\cos\left(\xi\frac{u}{b}\right) + K. \end{aligned} \tag{3.10}$$

In the equation, $K = (2q_0 - kb\sin\alpha)b^4\sin^4\alpha\cdot\cos\theta/(48D)$, and $\pm(\eta \pm \xi i)$ represent the four roots of the equation $\lambda^4 - 3(8 + 16\cos^2\alpha)\lambda^2 + 504 = 0$.

The deflection function equation of the main roof is given by

$$\omega_1 = UV = \left(\frac{v^4}{b^4} - 2\frac{v^3}{b^3} + \frac{v^2}{b^2}\right)\left[A_1\cosh\left(\eta\frac{u}{b}\right)\cos\left(\xi\frac{u}{b}\right) + A_2\sinh\left(\eta\frac{u}{b}\right)\sin\left(\xi\frac{u}{b}\right) + A_3\cosh\left(\eta\frac{u}{b}\right)\sin\left(\xi\frac{u}{b}\right) + A_4\sinh\left(\eta\frac{u}{b}\right)\cos\left(\xi\frac{u}{b}\right) + A_5\right]. \tag{3.11}$$

The boundary conditions for the initial fracture of the main roof are as follows:

$$\begin{cases} \omega_1|_{v=0,b} = \left.\dfrac{\partial\omega_1}{\partial y}\right|_{v=0,b} = 0, \\ \omega_1|_{u=0,a} = \left.\dfrac{\partial\omega_1}{\partial x}\right|_{u=0,a} = 0. \end{cases} \tag{3.12}$$

By applying the boundary conditions from Eq. (3.12), the following results can be obtained:

$$\begin{cases} A_1 = -K, \\ A_2 = \dfrac{K\left[\cosh\left(\eta\frac{a}{b}\right)\cos\left(\xi\frac{a}{b}\right) - 1\right] + \frac{\eta}{\xi}A_4\cosh\left(\eta\frac{a}{b}\right)\sin\left(\xi\frac{a}{b}\right) - A_4\sinh\left(\eta\frac{a}{b}\right)\cos\left(\xi\frac{a}{b}\right)}{\sinh\left(\eta\frac{a}{b}\right)\sin\left(\xi\frac{a}{b}\right)}, \\ A_3 = -\dfrac{\eta}{\xi}A_4, \\ A_4 = \left\{\begin{array}{l} -\left[\eta\cosh\left(\eta\frac{a}{b}\right)\sin\left(\xi\frac{a}{b}\right) + \xi\cos\left(\xi\frac{a}{b}\right)\sinh\left(\eta\frac{a}{b}\right)\right]K\left[\cosh\left(\eta\frac{a}{b}\right)\cos\left(\xi\frac{a}{b}\right) - 1\right] \\ \quad + \sinh\left(\eta\frac{a}{b}\right)\sin\left(\xi\frac{a}{b}\right)\left[-A_1\eta\sinh\left(\eta\frac{a}{b}\right)\cos\left(\xi\frac{a}{b}\right) + A_1\xi\cosh\left(\eta\frac{a}{b}\right)\sin\left(\xi\frac{a}{b}\right)\right] \end{array}\right\} \Big/ \\ \qquad \left\{\begin{array}{l} \eta\cosh\left(\eta\frac{a}{b}\right)\sin\left(\xi\frac{a}{b}\right)\left[\frac{\eta}{\xi}\cosh\left(\eta\frac{a}{b}\right)\sin\left(\xi\frac{a}{b}\right) - \sinh\left(\eta\frac{a}{b}\right)\cos\left(\xi\frac{a}{b}\right)\right] \\ \quad + \xi\cos\left(\xi\frac{a}{b}\right)\sinh\left(\eta\frac{a}{b}\right)\left[\frac{\eta}{\xi}\cosh\left(\eta\frac{a}{b}\right)\sin\left(\xi\frac{a}{b}\right) - \sinh\left(\eta\frac{a}{b}\right)\cos\left(\xi\frac{a}{b}\right)\right] \\ \quad - \sinh^2\left(\eta\frac{a}{b}\right)\sin^2\left(\xi\frac{a}{b}\right)\left(\frac{\eta^2}{\xi} + \xi\right) \end{array}\right\}. \end{cases} \tag{3.13}$$

3.2. Mechanical model of periodic fracture

During the periodic fracturing stage of the main roof, it remains in a state where three edges are fixed while one edge is suspended. To simplify the boundary conditions, let us refer to Fig. 3.

The solution process for the periodic fracture of the main roof is similar to that of the initial fracture. Let the deflection function for the periodic failure of the main roof be

$$\omega_2(u,v) = U_2V = \left(\frac{v^4}{b^4} - 2\frac{v^3}{b^3} + \frac{v^2}{b^2}\right)U_2. \tag{3.14}$$

Similarly, the calculation for the periodic fracture of the main roof yields:

$$U_2 = B_1\cosh\left(\eta\frac{u}{b}\right)\cos\left(\xi\frac{u}{b}\right) + B_2\sinh\left(\eta\frac{u}{b}\right)\sin\left(\xi\frac{u}{b}\right) + B_3\cosh\left(\eta\frac{u}{b}\right)\sin\left(\xi\frac{u}{b}\right) + B_4\sinh\left(\eta\frac{u}{b}\right)\cos\left(\xi\frac{u}{b}\right) + K. \tag{3.15}$$

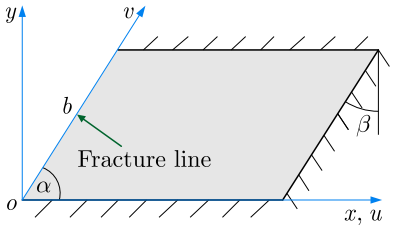

Fig. 3. Mechanical model for the periodic failure.

The boundary conditions for the periodic failure of the main roof are as follows:

$$\begin{cases} \omega_2|_{v=0,b} = \left.\dfrac{\partial \omega_2}{\partial y}\right|_{v=0,b} = 0, \qquad \omega_2|_{u=a} = \left.\dfrac{\partial \omega_2}{\partial x}\right|_{u=a} = 0, \\ M_x|_{u=0} = M_{xy}|_{u=0} = Q_x|_{u=0} = 0. \end{cases} \tag{3.16}$$

Based on the boundary conditions, the expressions for each parameter can be derived as follows:

$$\begin{cases} B_1 = -K_1K_2/K_3, \qquad B_2 = K_4B_1, \qquad B_3 = K_5B_4, \qquad B_4 = K_6B_1 + K_1, \\ K_1 = -K/\left[K_3\cosh\left(\eta\dfrac{a}{b}\right)\sin\left(\xi\dfrac{a}{b}\right) + \sinh\left(\eta\dfrac{a}{b}\right)\cos\left(\xi\dfrac{a}{b}\right)\right], \\ K_2 = K_3\eta\sinh\left(\eta\dfrac{a}{b}\right)\sin\left(\xi\dfrac{a}{b}\right) + K_3\xi\cosh\left(\eta\dfrac{a}{b}\right)\cos\left(\xi\dfrac{a}{b}\right) \\ \qquad + \eta\cosh\left(\eta\dfrac{a}{b}\right)\cos\left(\xi\dfrac{a}{b}\right) - \xi\sinh\left(\eta\dfrac{a}{b}\right)\sin\left(\xi\dfrac{a}{b}\right), \\ K_3 = \eta\sinh\left(\eta\dfrac{a}{b}\right)\cos\left(\xi\dfrac{a}{b}\right) - \xi\cosh\left(\eta\dfrac{a}{b}\right)\sin\left(\xi\dfrac{a}{b}\right) + K_2\eta\cosh\left(\eta\dfrac{a}{b}\right)\sin\left(\xi\dfrac{a}{b}\right) \\ \qquad + K_2\xi\sinh\left(\eta\dfrac{a}{b}\right)\cos\left(\xi\dfrac{a}{b}\right) + K_3K_4\eta\sinh\left(\eta\dfrac{a}{b}\right)\sin\left(\xi\dfrac{a}{b}\right) \\ \qquad + K_3K_4\xi\cosh\left(\eta\dfrac{a}{b}\right)\cos\left(\xi\dfrac{a}{b}\right) + K_4\eta\cosh\left(\eta\dfrac{a}{b}\right)\cos\left(\xi\dfrac{a}{b}\right) \\ \qquad - K_4\xi\sinh\left(\eta\dfrac{a}{b}\right)\sin\left(\xi\dfrac{a}{b}\right), \\ K_4 = \left(\xi^2 - \eta^2\right)/2\eta\xi, \\ K_5 = \left(3\eta\xi^2 - \eta^3\right)/\left(3\eta^2\xi - \xi^3\right), \\ K_6 = -\left[\cosh\left(\eta\dfrac{a}{b}\right)\cos\left(\xi\dfrac{a}{b}\right) + K_2\sinh\left(\eta\dfrac{a}{b}\right)\sin\left(\xi\dfrac{a}{b}\right)\right] \Big/ \\ \qquad\qquad \left[K_3\cosh\left(\eta\dfrac{a}{b}\right)\sin\left(\xi\dfrac{a}{b}\right) + \sinh\left(\eta\dfrac{a}{b}\right)\cos\left(\xi\dfrac{a}{b}\right)\right]. \end{cases} \tag{3.17}$$

3.3. Stress distribution in the main roof

According to plate theory (Xu, 2006), the deflection functions of the main roof (Eqs. (3.11) and (3.14)) yield:

$$\begin{cases} \sigma_x = -\dfrac{Ez}{1-\mu^2}\left[\dfrac{\partial^2\omega}{\partial u^2} + \mu\dfrac{1}{\sin^2\alpha}\left(\dfrac{\partial^2\omega}{\partial u^2}\cos^2\alpha - 2\dfrac{\partial^2\omega}{\partial u\partial v}\cos\alpha + \dfrac{\partial^2\omega}{\partial v^2}\right)\right], \\ \sigma_y = -\dfrac{Ez}{1-\mu^2}\left[\dfrac{1}{\sin^2\alpha}\left(\dfrac{\partial^2\omega}{\partial u^2}\cos^2\alpha - 2\dfrac{\partial^2\omega}{\partial u\partial v}\cos\alpha + \dfrac{\partial^2\omega}{\partial v^2}\right) + \mu\dfrac{\partial^2\omega}{\partial u^2}\right], \\ \tau_{xy} = -\dfrac{Ez}{1+\mu}\dfrac{1}{\sin\alpha}\left(\dfrac{\partial^2\omega}{\partial u\partial v} - \dfrac{\partial^2\omega}{\partial u^2}\cos\alpha\right). \end{cases} \tag{3.18}$$

The expression for the maximum principal stress is as follows:

$$\sigma_1 = \frac{1}{2}\left[\sigma_x + \sigma_y + \sqrt{(\sigma_x - \sigma_y)^2 + 4\tau_{xy}^2}\right]. \tag{3.19}$$

The failure criterion for the roof is defined as follows:

$$\sigma_1 > \sigma_t. \tag{3.20}$$

In this equation, σ_t represents the tensile strength of the roof rock mass.

3.4. Analysis of main roof stress distribution

Taking the 1044 working face of the Taoyuan Mine as an example, the working face length is $b = 165\,\text{m}$, and the main roof is composed of fine sandstone. For the convenience of parameter analysis, the mechanical properties of the basic roof are assumed to be homogeneous. The rock layer elastic modulus is $E = 8\,\text{GPa}$, $\mu = 0.23$, $h = 3.9\,\text{m}$, $\sigma_t = 6.4\,\text{MPa}$, and $\theta = 42°$. The pseudo-inclination angle is taken as $\beta = 6°$ for the analysis.

Figure 4 illustrates the stress distribution patterns during the initial fracture stage. The stress distribution exhibits an asymmetrical pattern, with the maximum tensile stress of 9.08 MPa occurring at the center of the lower surface. This indicates that fracturing of the lower surface will initiate at the central region. In contrast, the edges of the lower surface are primarily subjected to compressive stress, with a maximum value of 4.25 MPa. The maximum tensile stress of 18.32 MPa occurs in the central region of the long edge on the upper surface of the main roof. The stress on the upper surface is greater than that on the lower surface, indicating that the initial fracture occurs first in the central region of the long edge on the upper surface.

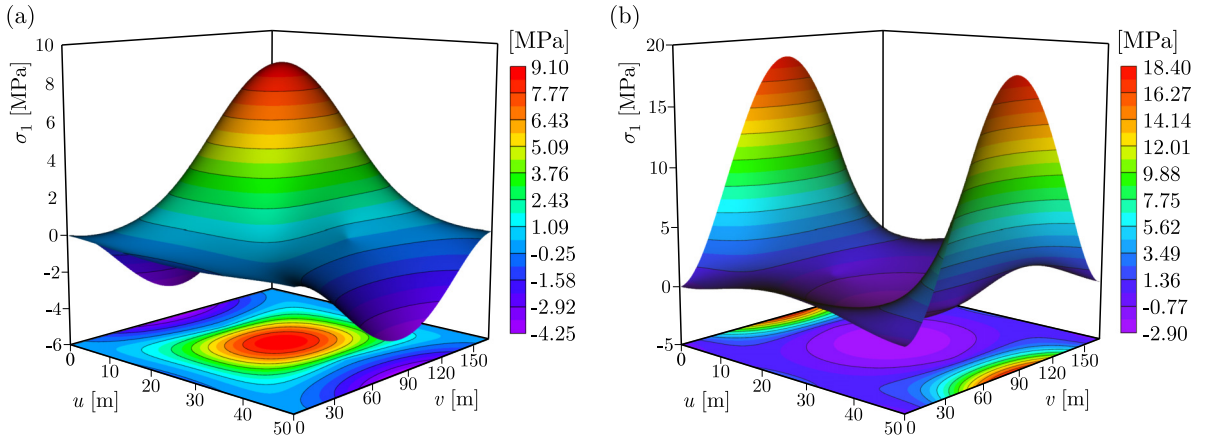

Fig. 4. Stress distribution during the initial failure of the main roof: (a) lower surface; (b) upper surface.

Figure 5 depicts the stress distribution on the upper and lower surfaces of the main roof during the periodic fracture stage. The maximum tensile stress of 2.16 MPa occurs slightly above the center of the free edge on the lower surface, which may be attributed to the linearly distributed overlying load and the parallelogram-shaped roof structure resulting from the inclined mining layout. This configuration leads to an uneven stress distribution. The maximum stress on the fixed long edge of the upper surface of the main roof is 18.74 MPa, occurring at the central region, which is greater than the maximum tensile stress on the lower surface. This indicates that the periodic fracture of the main roof first occurs in the central region of the fixed long edge on the upper surface.

3.5. Analysis of the optimal pseudo-inclined angle

In steeply inclined coal seams, a pseudo-inclined layout is commonly adopted to prevent coal self-flow and the safety hazards associated with flying debris. Therefore, determining the optimal

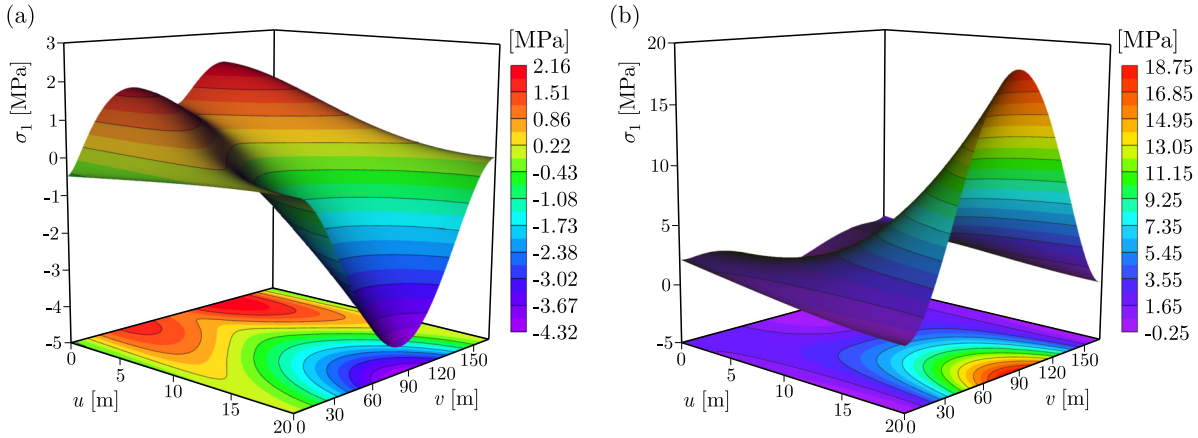

Fig. 5. Stress distribution during the periodic failure of the main roof: (a) lower surface; (b) upper surface.

pseudo-inclination angle is a critical issue. Figures 6 and 7 illustrate variations in the maximum principal stress at the main roof under different pseudo-inclination angles.

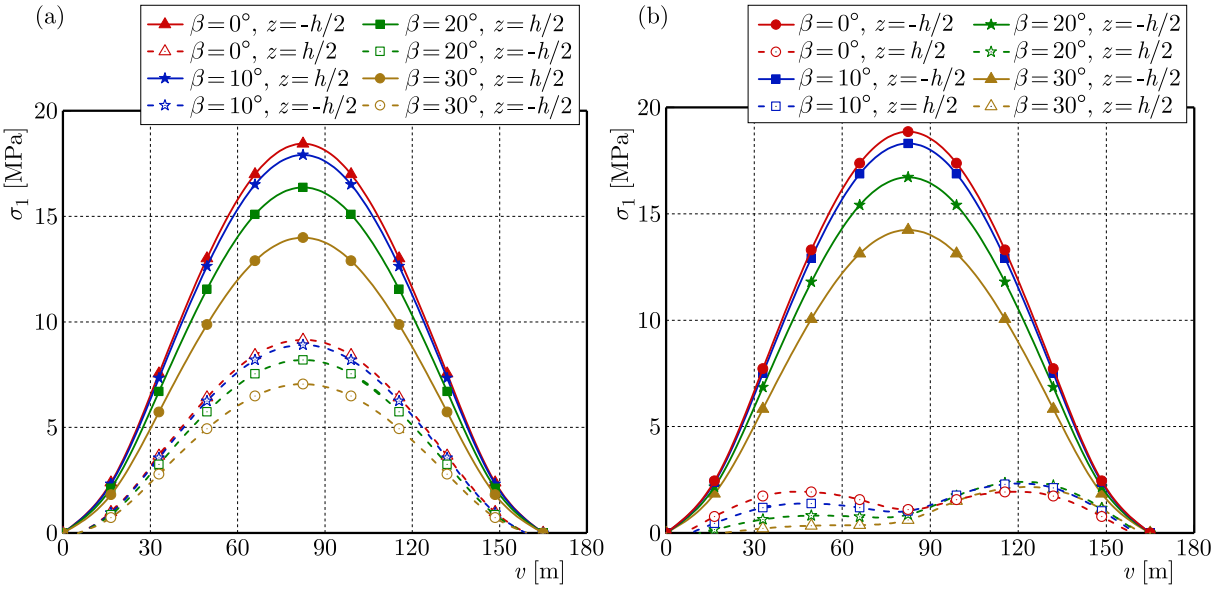

Fig. 6. Variations in deflection and maximum principal stress during initial fracture.

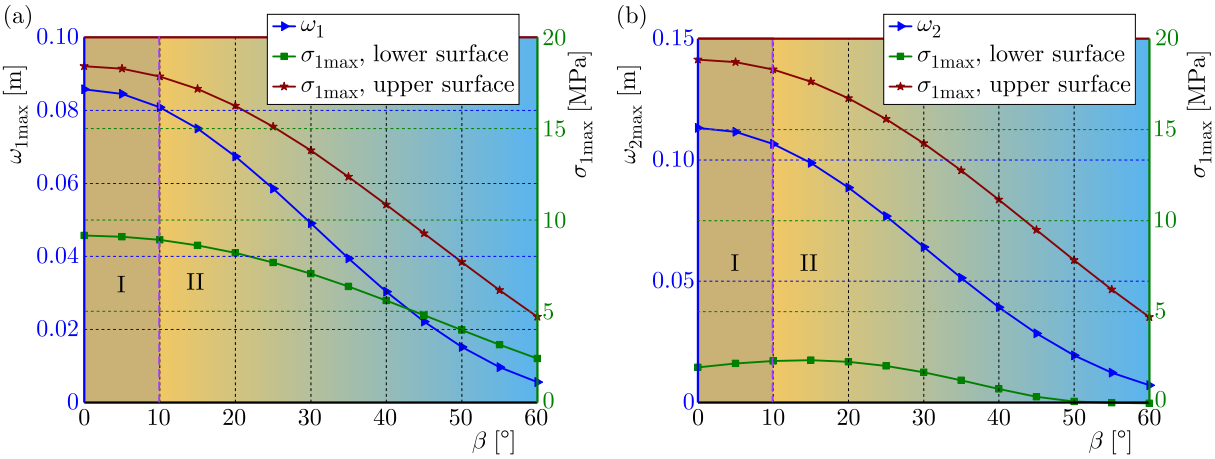

Fig. 7. Variation curves of maximum deflection and maximum principal stress with pseudo-inclination angle.

Figure 6 illustrates the variation patterns of the maximum principal stress during the initial fracture stage. As illustrated in Fig. 6a, the maximum principal stress during the initial fracture stage decreases gradually as the pseudo-inclination angle increases, thereby resulting in an extended initial weighting step distance. This is due to the fact that as the pseudo-inclined angle increases, the long edge of the roof becomes progressively larger, enhancing the support constraints along this direction, and thereby increasing the roof stability. Figure 6b illustrates the variation patterns of the maximum principal stress during the periodic fracture stage. Figure 6b indicates that the stress on the fixed boundary of the upper surface ($u = a$, $z = -h/2$) decreases as the pseudo-inclination angle increases, as is the case with the stress variation observed in the initial fracture stage. In contrast, the maximum principal stress on the free edge of the lower surface ($u = 0$, $z = h/2$) exhibits an irregular M-shaped distribution, with an increasing trend as the pseudo-inclination angle grows. The stress in the upper-middle section of the working face tends to increase, whereas the stress in the lower-middle section decreases, leading to the initial fracture of the lower surface in the upper-middle region. Because the load on the lower part of the roof is greater than that on the upper part, the fractured roof rock blocks rotate downward from the upper-middle region, posing challenges to the support of hydraulic props in the lower-middle section of the working face and the stability of the coal wall.

Figure 7 illustrates the variation curves of the maximum deflection and maximum tensile stress of the roof with respect to the pseudo-inclination angle. As the pseudo-inclined angle increases, both the deflection and the maximum principal stress decrease. As shown in region I of Fig. 7, when the pseudo-inclined angle is between 0° and 10°, the changes in both deflection and stress are relatively gradual. In region II of Fig. 7, when the pseudo-inclined angle ranges from 10° to 60°, the maximum deflection and the maximum principal stress decrease sharply, and the step distance for roof fracture also increases. Based on the above analysis, when the pseudo-inclination angle of the working face exceeds 10°, the stress distribution of the basic roof becomes significantly more uneven. This increased heterogeneity poses challenges to the hydraulic supports in the middle and lower sections of the working face and compromises coal wall stability, making roof control more difficult. Consequently, mechanized mining may face issues with equipment stability and safety. Considering these factors, the maximum pseudo-inclination angle for the 1044 working face layout should not exceed 10°.

In summary, when designing the pseudo-inclined angle for the working face, it is essential to ensure an angle that provides sufficient advance distance, thereby preventing the sliding of coal or rock that may pose a safety risk to personnel and equipment. However, during the cyclical fracture of the main roof, excessively large pseudo-inclined angles may pose challenges for hydraulic support and compromise the stability of the coal wall. Therefore, the reasonable design range of the pseudo-inclination angle of the 1044 working face is 5° to 10°, the leading distance of the working face is 14.3 m to 28.6 m. While mining the working face, the pseudo-inclination angle is set to about 8°. According to theoretical calculations, the initial fracture step distance of the main roof is 32 m, and the periodic fracture step distance is 13 m.

4. Engineering analysis

The 1044 working face utilizes a pseudo-inclined layout, with the pseudo-inclined angle controlled between 5° and 10° during mining. The hydraulic supports used on the working face are of the ZZ10000/21/45D model, with a total of 110 units, spaced at 1.5 m intervals. Pressure sensors are installed on the support units to monitor the mining pressure. A sensor is installed for every 10 sets of electromagnetic valves. The monitoring of support loads serves as a fundamental technique for assessing the stability of the working face, providing key information on roof structure evolution and the response of the support system. The layout of the working resistance measurement zones for the hydraulic supports, shown in Fig. 8a, divides the working face into five areas: lower, lower-middle, middle, upper-middle, and upper. By analyzing variations in

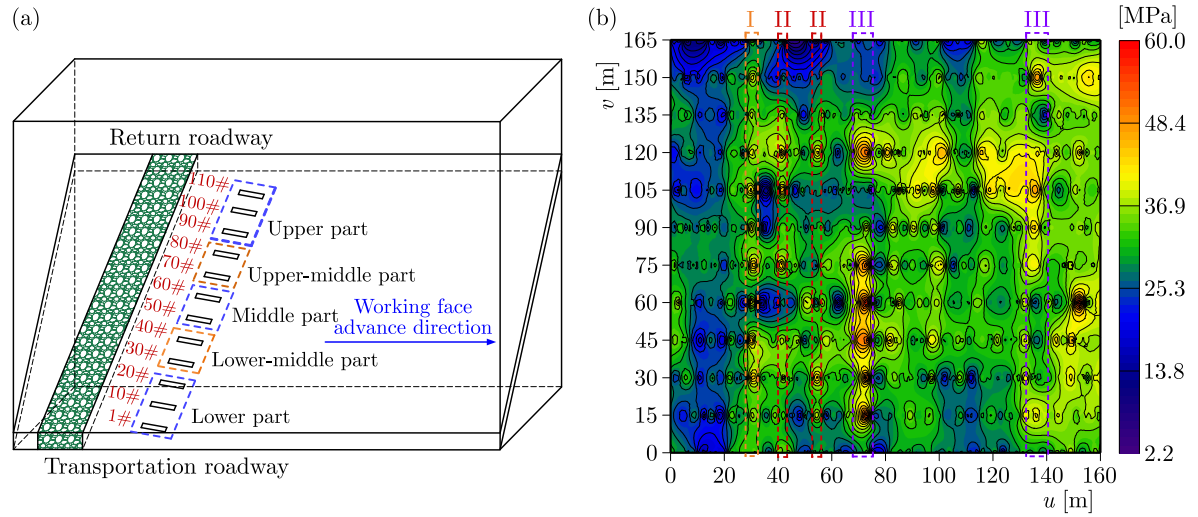

Fig. 8. Monitoring of hydraulic support load.

hydraulic support pressure, the roof fracture pattern and the collapse step distance can be determined. Based on the data obtained from hydraulic support monitoring, pressure distribution contour maps were generated using Origin software. The load distribution of hydraulic supports at different mining distances is shown in Fig. 8b.

In the load distribution map, area I represents the initial roof pressure, area II represents the periodic roof pressure, and area III shows a significant increase in support load compared to other locations, indicating roof pressure caused by the fracture of the key strata above the working face. The initial roof pressure occurs at around 30 meters, the first periodic roof pressure occurs at around 42 meters, and key strata fractures in the roof occur at 72 meters and 136 meters. During the periodic roof pressure phase, the loads on the upper and lower hydraulic supports are noticeably smaller than those in other areas. The reduced load on the upper hydraulic supports is due to the uneven distribution of the roof load, with the upper part of the roof carrying significantly less load than the lower part. The reduced load on the lower hydraulic supports may be due to two reasons: first, the pseudo-inclined mining layout results in a sharp angle at the bottom of the roof, where the constraints of the coal and overlying rock layers are stronger. Second, after the overlying strata fracture, the rock fragments slide downward, filling the lower goaf and counteracting some of the vertical stress on the roof, which slows the roof's fracture and rotation.

The support load curves for five positions on the working face: upper, upper-middle, middle, lower-middle, and lower, are shown in Fig. 9. From the variation in hydraulic support pressure at different locations, it can be observed that the initial roof pressure occurs at around 30 meters. The maximum average load during the initial roof pressure phase is 32.9 MPa, with the load at the middle of the working face exceeding that at other locations. The 50# support at the center of the working face experiences the first roof pressure at the earliest, with a maximum load of 47.3 MPa. Since the middle of the roof experiences the greatest deflection, the first fracture occurs in the middle, which is consistent with the field results and theoretical analysis.

The step distance for periodic roof pressure is 10 to 15 meters, and the first periodic roof pressure has a maximum load of 49.1 MPa, occurring at the 80# support in the middle-upper section, as shown in Fig. 9e. From the curve, it can be seen that the load at the first periodic roof pressure on the middle-upper supports is greater than the initial roof pressure, unlike the roof pressure behavior at other locations. The maximum average load during the periodic roof pressure phase is 36.9 MPa, and the load on the middle-upper section is significantly higher than that at other locations. The theoretical analysis indicates that when a pseudo-inclined layout is used, periodic fractures in the roof first occur in the middle-upper section, which

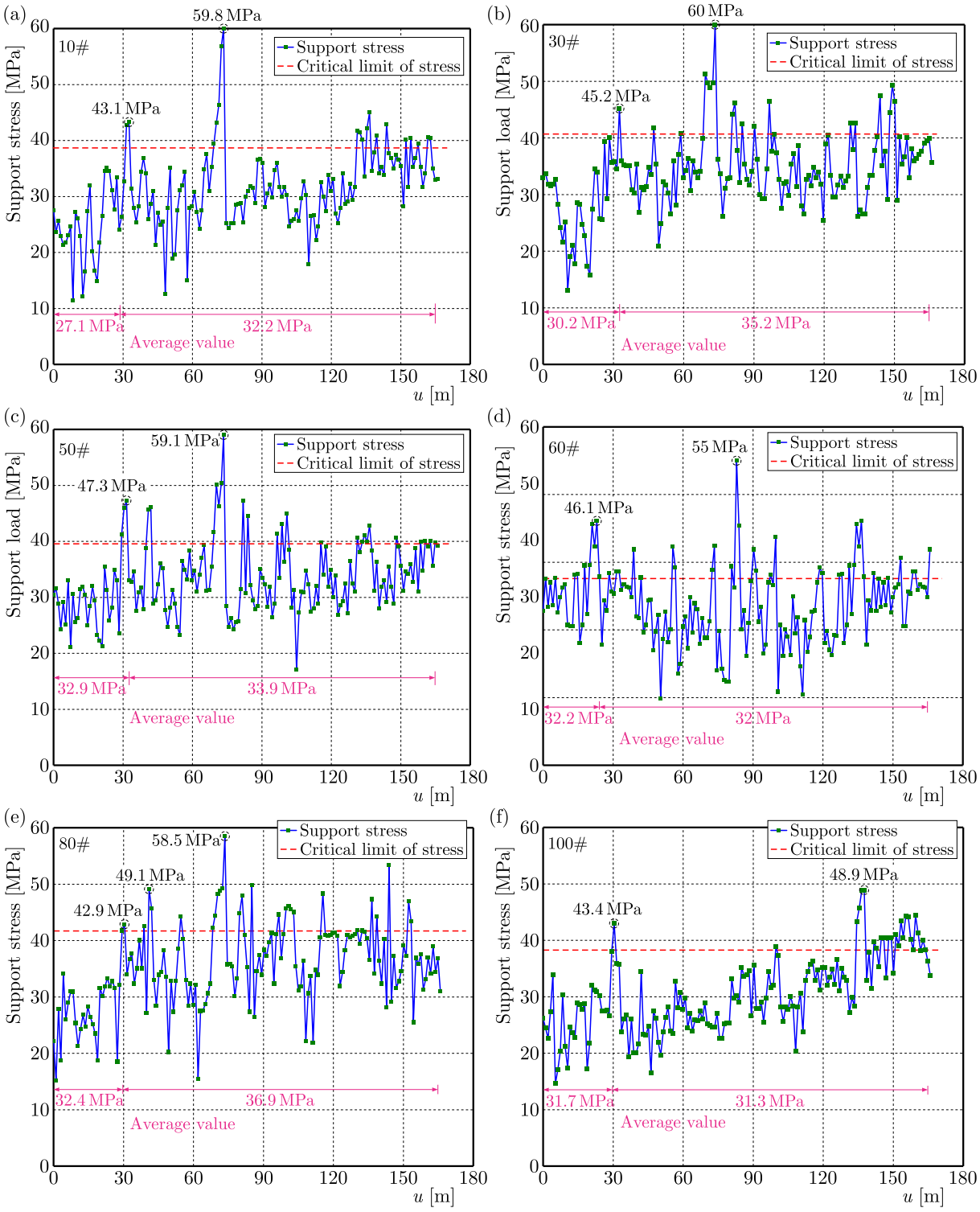

Fig. 9. Hydraulic support working resistance.

results in higher periodic roof pressure in this area. The field monitoring results confirm the reliability of the theoretical analysis. The ultimate working resistance of the hydraulic supports is 70 MPa. When the support load exceeds this limit, the support system may become overloaded, potentially compromising the stability of the mining space. Field monitoring results indicate that the peak loads during roof failure did not exceed the ultimate working resistance of the hydraulic supports. No support collapses occurred, and no large-scale coal wall spalling was observed, demonstrating that the hydraulic supports effectively maintained working face stability.

5. Discussion

This study establishes a mechanical model for the basic roof failure of pseudo-inclined working faces in steeply inclined coal seams based on elastic thin-plate theory and validates it through field monitoring. Compared with conventional roof-breakage theories that assume a rectangular plate, the present work introduces a parallelogram-plate model that better represents the spatial geometry after pseudo-inclined layout. This approach improves the applicability for simulating asymmetric deformation, stress distribution, and roof failure locations. The results indicate that both the initial and periodic breakage of the basic roof exhibit pronounced asymmetry, with failures more likely to occur in the upper-middle region, consistent with the observed mine pressure behavior.

The theoretical derivation further quantifies the influence of pseudo-inclination angle adjustment on roof deflection, principal stresses, and breakage intervals, thereby defining a rational range of angles and enhancing the theoretical basis and generalizability of angle design. It should be noted, however, that the mechanical model adopted herein remains based on the elastic thin-plate assumption and does not account for more complex factors such as stratified rock structures, jointed weak planes, or shear-dominated failure. Future research may incorporate discrete-element methods to improve the model's completeness.

6. Conclusion

To investigate the fracture mechanism of the roof in an inclined mining face of a steeply dipping coal seam and determine the optimal pseudo-inclination angle for face layout, a mechanical model of roof fracture was established. The stress and deformation characteristics of the roof were analyzed, and the reasonable range of pseudo-inclination angles was identified. Furthermore, field monitoring data were employed to validate the theoretical model. The following conclusions were drawn:

1) A mechanical model for the initial and periodic breakage of the basic roof in pseudo-inclined working faces was developed based on elastic thin-plate theory, revealing the asymmetric deformation and stress distribution induced by the pseudo-inclined layout. The results show that initial roof breakage first occurs near the fixed long edge of the upper surface and the central region of the lower surface. Periodic breakage also exhibits strong asymmetry, appearing first at the central area of the fixed long edge on the upper surface and the upper–middle portion of the free edge on the lower surface, which differs substantially from the breakage patterns typically observed in conventional coal-seam extraction.
2) As the pseudo-inclined angle increases, the maximum tensile stress in the upper-middle region of the working face rises, whereas the maximum tensile stress in the lower region decreases, resulting in reduced roof stability and concentrated loading on the hydraulic supports, thereby increasing the risk of support adaptation failure. Theoretical analysis indicates that the optimal pseudo-inclined angle for the 1044 working face ranges from 5° to 10°, which satisfies the combined requirements for equipment anti-slip performance, spontaneous gangue sliding control, and coal wall stability. Field monitoring data show that the support loads did not exceed the ultimate working resistance during extraction, and no support collapses or severe coal wall spalling occurred, confirming the rationality of the design parameters.
3) Field mine-pressure monitoring reveals that initial weighting is concentrated in the middle of the working face, while peak periodic loading occurs in the upper–middle region. These observations are fully consistent with the theoretical predictions, demonstrating that the proposed model effectively identifies roof-breakage locations and the intensity of mine-pressure manifestation in pseudo-inclined working faces. The findings provide a theoretical basis for evaluating roof stability and designing support parameters for hydraulic supports.

Acknowledgments

This research was financially supported by the National Natural Science Foundation of China (no. 52204114), the Natural Science Foundation of Jiangsu Province (no. BK20210522).

References

1. Çelik, A., & Özçelik, Y. (2023). Investigation of the effect of caving height on the efficiency of the longwall top coal caving production method applied in inclined and thick coal seams by physical modeling. *International Journal of Rock Mechanics and Mining Sciences*, *162*, Article 105304. https://doi.org/10.1016/j.ijrmms.2022.105304
2. Das, A.J., Mandal, P.K., Bhattacharjee, R., Tiwari, S., Kushwaha, A., & Roy, L.B. (2017). Evaluation of stability of underground workings for exploitation of an inclined coal seam by the ubiquitous joint model. *International Journal of Rock Mechanics and Mining Sciences*, *93*, 101–114. https://doi.org/10.1016/j.ijrmms.2017.01.012
3. Das, A.J., Paul, P.S., Mandal, P.K., Kumar, R., & Tewari, S. (2021). Investigation of failure mechanism of inclined coal pillars: Numerical modelling and tensorial statistical analysis with field validations. *Rock Mechanics and Rock Engineering*, *54*(6), 3263–3289. https://doi.org/10.1007/s00603-021-02456-5
4. Do, T.N., Wu, J.-H., & Lin, H.-M. (2017). Investigation of sloped surface subsidence during inclined seam extraction in a jointed rock mass using discontinuous deformation analysis. *International Journal of Geomechanics*, *17*(8). https://doi.org/10.1061/(ASCE)GM.1943-5622.0000894
5. Eremin, M., Peryshkin, A., Esterhuizen, G., Pavlova, L., & Fryanov, V. (2022). Numerical analysis of pillar stability in longwall mining of two adjacent panels of an inclined coal seam. *Applied Sciences*, *12*(21), Article 11028. https://doi.org/10.3390/app122111028
6. Islavath, S.R. (2023). Numerical modelling approach for estimation of a yield zone in the face of a deep longwall panel. *Scientific Reports*, *13*, Article 20811. https://doi.org/10.1038/s41598-023-47683-8
7. Islavath, S.R., Deb, D., & Kumar, H. (2016). Numerical analysis of a longwall mining cycle and development of a composite longwall index. *International Journal of Rock Mechanics and Mining Sciences*, *89*, 43–54. https://doi.org/10.1016/j.ijrmms.2016.08.003
8. Kumar, R., Mandal, P.K., Ghosh, N., Das, A.J., & Banerjee, G. (2023). Design of stable parallelepiped coal pillars considering geotechnical uncertainties. *Rock Mechanics and Rock Engineering*, *56*(9), 6581–6602. https://doi.org/10.1007/s00603-023-03415-y
9. Lang, D., Wu, X., Wu, Y., Lin, H., & Luo, S. (2021). Boundary distribution of top-coal limit-equilibrium zone in fully mechanized caving in steeply dipping coal seams. *Geomatics, Natural Hazards and Risk*, *12*(1), 2561–2589. https://doi.org/10.1080/19475705.2021.1969450
10. Li, X., Wang, Z., & Zhang, J. (2017). Stability of roof structure and its control in steeply inclined coal seams. *International Journal of Mining Science and Technology*, *27*(2), 359–364. https://doi.org/10.1016/j.ijmst.2017.01.018
11. Luo, S., Wang, T., Wu, Y., Huangfu, J., & Zhao, H. (2021). Internal mechanism of asymmetric deformation and failure characteristics of the roof for longwall mining of a steeply dipping coal seam. *Archives of Mining Sciences*, *66*(1), 101–124. https://doi.org/10.24425/ams.2021.136695
12. Pan, R., Cao, S., Shen, D., Liang, J., & Liao, J. (2017). Model of the roof fracture in pitching diagonal mining panel and its field measurement (in Chinese). *Journal of Mining and Safety Engineering*, *34*(4), 637–643. https://doi.org/10.13545/j.cnki.jmse.2017.04.005
13. Proyavkin, E.T. (1993). New nontraditional technology of working thin and steep coal seams. *Ugol Ukrainy*, *3*, 2–4.
14. Rak, Z., Stasica, J., Burtan, Z., & Chlebowski, D. (2020). Technical aspects of mining rate improvement in steeply inclined coal seams: A case study. *Resources*, *9*(12), Article 138. https://doi.org/10.3390/resources9120138

15. Sun, J., Liu, X., & Ren, T. (2019). Overburden stability of an inclined backfill stope in the context of the nonlinear elastic mechanical properties of the backfill body. *Environmental Earth Sciences*, *78*(24), Article 719. https://doi.org/10.1007/s12665-019-8728-8

16. Tu, H., Tu, S., Yuan, Y., Wang, F., & Bai, Q. (2015). Present situation of fully mechanized mining technology for steeply inclined coal seams in China. *Arabian Journal of Geosciences*, *8*(7), 4485–4494. https://doi.org/10.1007/s12517-014-1546-0

17. Wang, J.-a., & Jiao, J.-l. (2016). Criteria of support stability in mining of steeply inclined thick coal seam. *International Journal of Rock Mechanics and Mining Sciences*, *82*, 22–35. https://doi.org/10.1016/j.ijrmms.2015.11.008

18. Wang, L. (1983). The Kantorovich method for the bending problem of parallelogram plates (in Chinese). *Journal of Hunan University*, (04):36–47. https://doi.org/10.19636/j.cnki.cjsm42-1250/o3.1983.03.013

19. Wu, Y., Yun, D., Xie, P., Wang, H., Lang, D., & Hu, B. (2020). Progress, practice and scientific issues in steeply dipping coal seams fully-mechanized mining (in Chinese). *Journal of China Coal Society*, *45*(1), 24–34. https://doi.org/10.13225/j.cnki.jccs.YG19.0494

20. Xie, P., Luo, Y., Wu, Y., Gao, X., Luo, S., & Zeng, Y. (2020). Roof deformation associated with mining of two panels in steeply dipping coal seam using subsurface subsidence prediction model and physical simulation experiment. *Mining Metallurgy & Exploration*, *37*(2), 581–591. https://doi.org/10.1007/s42461-019-00156-x

21. Xu, Z. (2006). *Elasticity mechanics* (in Chinese). Higher Education Press, Beijing.

22. Yang, Y., Lai, X., Shan, P., & Cui, F. (2020). Comprehensive analysis of dynamic instability characteristics of steeply inclined coal-rock mass. *Arabian Journal of Geosciences*, *13*(6), Article 241. https://doi.org/10.1007/s12517-020-5217-z

23. Zhang, P., Li, Z., Wei, Y., Chen, Y., & Dong, L. (2025). Analysis of the roof damage range in close-proximity gently inclined coal seams mining and the feasibility of upward mining. *Scientific Reports*, *15*, Article 5324. https://doi.org/10.1038/s41598-025-89808-1

24. Zhao, Z., Pan, W., & Deng, C. (2025). Analysis of longwall shield operation in inclined coal seams. *Mining, Metallurgy & Exploration*, *42*(4), 2237–2252. https://doi.org/10.1007/s42461-025-01303-3

Manuscript received May 16, 2025; accepted for publication December 30, 2025; published online February 13, 2026.

JOURNAL OF THEORETICAL
AND APPLIED MECHANICS
64, 1, pp. 85–97, Warsaw 2026
https://doi.org/10.15632/jtam-pl/217048

MACHINE LEARNING-AUGMENTED UNIVERSAL WEIGHT FUNCTION METHOD FOR STRESS INTENSITY FACTOR DETERMINATION

Kaimin GUO*, Wei TANG, Zijiang YANG, Changxi WANG, Tianyu SUN

China Aero-Polytechnology Establishment, Beijing, China
*corresponding author, *dr_guokaimin@163.com*

The accurate calculation of stress intensity factors (SIFs) constitutes a critical yet challenging task within linear elastic fracture mechanics. While the universal weight function method (WFM) has emerged as a prominent approach due to its high computational efficiency, its predictive accuracy is often constrained. This limitation arises from the difficulty in characterizing the nonlinear mapping relationships between the geometric dimensions of cracked bodies and the requisite weight function parameters. To address these challenges, this study introduces an innovative machine learning-augmented universal WFM. This method leverages Gaussian process regression (GPR) models to characterize the nonlinear mapping relationships between the geometric dimensions of cracked bodies and the weight function parameters, thereby enhancing the computational accuracy of the universal WFM. Validation cases demonstrate that the proposed method achieves superior accuracy compared to the traditional universal WFM, with the maximum relative error not exceeding 5.09 %.

Keywords: stress intensity factor solutions, weight function method, machine learning, Gaussian process regression, a corner crack at a hole.

Articles in JTAM are published under Creative Commons Attribution 4.0 International.
Unported License https://creativecommons.org/licenses/by/4.0/deed.en.
By submitting an article for publication, the authors consent to the grant of the said license.

1. Introduction

Under linear elastic and small-scale yielding conditions, the stress intensity factor (SIF, commonly denoted as K) serves as the fundamental parameter characterizing the crack-tip stress field and the primary driving force for crack propagation. The accuracy of SIF calculations directly governs the reliability of crack growth life predictions, rendering its computational methodology a central focus in linear elastic fracture mechanics research.

Closed-form solutions, finite element methods (FEMs), weight function methods (WFMs), and machine learning-based approaches represent principal computational methodologies for determining SIFs (McClung *et al.*, 2013). Closed-form equations were proposed in (Newman & Raju, 1981; 1984; Raju & Newman, 1979). Their fundamental principle resides in fitting SIFs, obtained from extensive FEM calculations, into explicit closed-form equations. During computation, one simply substitutes the geometric and characteristic parameters into these closed-form equations. This approach is computationally efficient, requiring minimal computational effort. However, its applicability is restricted to simple geometric configurations and basic loading conditions, specifically remote tension and bending. Commercial finite element analysis (FEA) software packages offer high computational accuracy and represent an effective tool for determining SIFs (Wawrzynek *et al.*, 2010; Xiao & Yan, 2008). However, it should be noted that while the FEM inherently provides high accuracy, it inevitably suffers from computational inefficiency. For complex geometries, crack configurations, and loading conditions, FEM analyses typically entail substantial computational time and significant computational expenses. Propelled by rapid advances in artificial intelligence and data-driven technologies, machine learning (ML) has emerged

as a prominent research focus for predicting SIFs (Guo *et al.*, 2024; Keprate *et al.*, 2017; Muñoz-Abella *et al.*, 2015). The principal advantage of ML methodologies lies in their computational efficiency and expediency: once an ML model is adequately trained, SIF values for arbitrary loading conditions and structural configurations can be rapidly obtained.

The WFM represents a mainstream computational approach for determining SIFs, offering a balanced compromise between computational accuracy and efficiency (Chen & Wang, 2004; Evans *et al.*, 2014; Glinka & Shen, 1991; Shen & Glinka, 1991a; Vainshtok & Varfolomeyev, 1990; Zheng *et al.*, 1996). Its fundamental principle lies in decoupling the two primary factors influencing SIF calculations – geometry and loading. Specifically, the SIF is expressed as the integral of the product of the weight function and the applied loading distribution along the crack length (Yang *et al.*, 2013).

A complex nonlinear relationship exists between the key parameters within the weight function and the crack geometry dimensions. In the conventional derivation of universal weight functions, polynomial fitting methods are commonly employed to describe this nonlinear relationship. However, the resulting fitting coefficients, often exceeding one hundred terms, impose a significant computational burden and hinder the practical application of the WFM (Ghajar & Saeidi Googarchin, 2013; Shen & Glinka, 1991b; Shen *et al.*, 1991; Wang & Lambert, 1995a; 1995b; Yang *et al.*, 2013). Due to the inability to accurately characterize the nonlinear relationship between the key parameters and the geometric dimensions, the universal WFM exhibits inherent limitations in predictive accuracy. Consequently, the adoption of advanced fitting techniques is necessitated to precisely capture the nonlinear relationship between the key parameters and the crack body geometry, thereby enhancing the computational accuracy of the universal WFM.

This study proposes an innovative machine learning-augmented universal WFM designed to characterize the nonlinear mapping between cracked body geometry dimensions and weight function parameters, thereby enhancing the computational accuracy of SIFs. Initially, the fundamental principles and derivation process of the universal weight function are demonstrated using a corner crack at a hole as a representative case study. Subsequently, the proposed ML-augmented WFM is presented, whose core involves employing a Gaussian process regression (GPR) model to characterize the nonlinear mapping relationships between the geometric dimensions of the cracked body and the weight function parameters. Finally, the predictive accuracy of the proposed method is demonstrated through the calculation of the SIF for the corner crack at a hole under new loading conditions.

2. Derivation procedure of the universal WFM

In this section, a corner crack at a hole is employed as a case study to elucidate the physical significance of the crack body's geometric dimensions. Subsequently, this corner crack at a hole is used as an example to demonstrate the derivation procedure of the universal WFM.

2.1. A corner crack at a hole

Taking an aero-engine turbine disk as an example, it contains various functional holes – such as the central bore hole, dowel holes, and eccentric holes – which are prone to crack initiation and propagation. A simplified model of the corner crack at one such hole is illustrated in Fig. 1.

A plate of thickness t contains a central hole of radius r. A quarter-elliptical corner crack emanates from one side of the hole, with its depth direction aligned with the plate thickness direction. The crack surface experiences uniaxial stress variation; under non-uniformly distributed stress, the stress varies solely along the y-axis (i.e., the plate thickness direction). In the schematic, a denotes the crack depth, and c represents the surface crack length. Point A, the deepest vertex of the crack front located at the hole surface, is hereafter termed the "hole-surface point". Point B, the surface vertex on the plate face, is designated as the "plate-surface point".

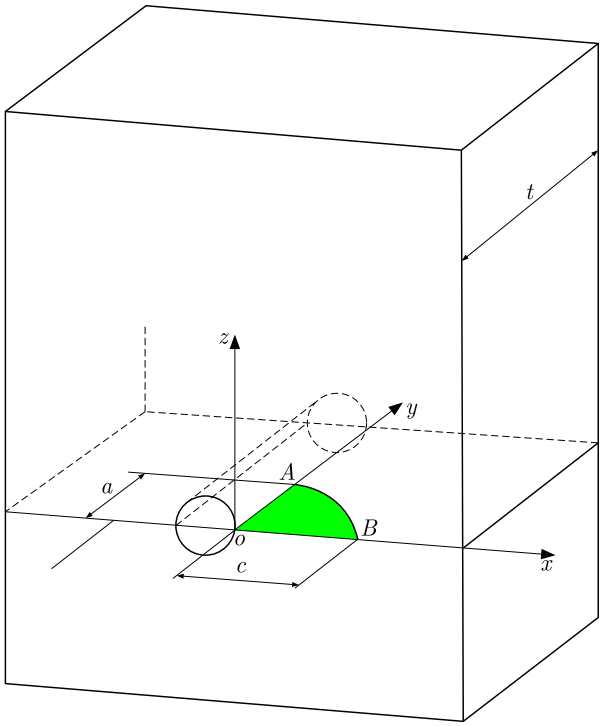

Fig. 1. Corner crack at a hole.

2.2. Stress intensity factor data acquisition

The principle of the universal WFM states that the SIF is calculated as the integral of the product of the weight function and the nominal stress along the crack length, as expressed in Eq. (2.1). Here, $m(y,a)$ denotes the weight function – a parameter independent of loading conditions and solely dependent on geometric configuration and crack morphology. The variable a represents crack length, while $\sigma(y)$ signifies the stress acting on the crack face, specifically defined as the nominal stress on the prospective crack plane in the imaginary uncracked structure. Within weight function theory, once the weight function $m(y,a)$ for a given crack type is determined, the SIF under any arbitrary loading can be computed using Eq. (2.1):

$$K = \int_0^a \sigma(y) m(y,a)\,\mathrm{d}y. \tag{2.1}$$

The derivation procedure for the universal weight function pertaining to corner cracks emanating from a hole entails several key steps. Firstly, a comprehensive dataset of SIFs for the corner crack, corresponding to various geometric configurations, is compiled utilizing numerical methods such as the FEM. This dataset serves as the foundational input. Subsequently, reference SIFs are derived through curve fitting techniques. Finally, these fitted reference SIFs are substituted into the governing weight function equation (Eq. (2.1)) to inversely solve it for the universal weight function itself. Each step is elaborated in Subsection 2.2 to 2.4.

In this study, the FEM is employed to compute the reference SIFs for corner cracks at a hole. The key geometric parameters characterizing the configuration, comprising a circular hole and associated corner cracks, include the crack dimensions a and c, the plate thickness t, and the hole radius r. The SIF data for corner cracks emanating from a hole, computed via FEA, serve as input data for subsequent fitting of reference SIFs.

To ensure the derived weight function provides comprehensive coverage over a broad range of crack sizes, the reference solutions encompass the following dimensional ranges: $0.2 \leq a/c \leq 1$, $0.2 \leq a/t \leq 0.8$ and $0.3 \leq r/t \leq 2$. To span this domain, 100 distinct configurations were

analyzed, combining the parameters $r/t = \{0.3, 0.5, 1, 1.5, 2\}$, $a/t = \{0.2, 0.4, 0.6, 0.8\}$ and $a/c = \{0.2, 0.4, 0.6, 0.8, 1\}$. Additionally, the plate dimensions were specified as thickness $t = 10\,\text{mm}$, width $W = 50\,\text{mm}$, and the semi-height of the cracked plate is 100 mm.

The universal weight function methodology requires that the two reference loading cases exhibit distinct polynomial orders along the same coordinate axis. Considering load distributions along the y-axis as an illustrative case, the functional forms of these reference loads must incorporate different exponents of y. Consistent with this selection principle, a uniformly distributed load and a linearly distributed load were selected as reference cases. Their mathematical expressions and schematic representations are provided in Eq. (2.2) and Fig. 2, respectively, where $\sigma_0 = 200\,\text{MPa}$:

$$\begin{aligned} \sigma_{r1}(y) &= \sigma_0, \\ \sigma_{r2}(y) &= \sigma_0 \left(1 - \frac{y}{a}\right). \end{aligned} \tag{2.2}$$

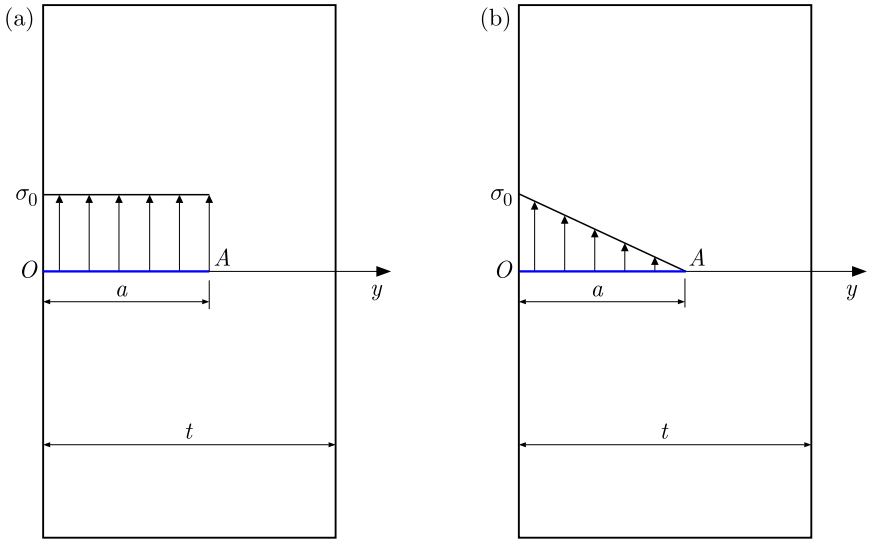

Fig. 2. Two reference loading cases: (a) a uniformly distributed load and (b) a linearly distributed load.

For a corner crack at a hole, 200 sets of SIF data were computed via the aforementioned FEM under uniformly distributed and linearly distributed loads. Selected partial computed SIF results are presented in Table 1.

Table 1. Partial computed SIF results for the corner crack at a hole (unit: $\text{MPa} \cdot \text{m}^{1/2}$).

Geometric dimensions [mm]				Uniformly distributed load		Linearly distributed load	
t	r	a	c	Point A	Point B	Point A	Point B
10	3	2	2	**9.87**	**10.47**	**2.69**	**8.98**
	5	4	10	**18.8**	**16.21**	**6.61**	**13.59**
	10	6	15	**26.64**	**23.84**	**10.26**	**19.41**
	15	8	40	**47.62**	**40.81**	**21.68**	**31.68**
	20	2	2.5	**11.73**	**11.11**	**3.61**	**9.4**

2.3. Weight functions for the hole-surface point (point *A*)

The fitted reference SIFs at point A are given by Eqs. (2.3) and (2.4), corresponding to the uniformly distributed load and linearly distributed load cases, respectively:

$$K_{r1}^{A} = \sigma_0 \sqrt{\frac{\pi a}{Q}} F_0^A, \tag{2.3}$$

$$K_{r2}^{A} = \sigma_0 \sqrt{\frac{\pi a}{Q}} F_1^A, \tag{2.4}$$

where Q denotes an elliptical integral of the second kind as follows:

$$\begin{aligned} Q &= 1 + 1.464 \left(\frac{a}{c}\right)^{1.65} && \text{for} \quad \frac{a}{c} \le 1, \\ Q &= \left[1 + 1.464 \left(\frac{c}{a}\right)^{1.65}\right] \left(\frac{a}{c}\right)^{2} && \text{for} \quad \frac{a}{c} > 1. \end{aligned} \tag{2.5}$$

The geometric correction factors F_0^A and F_1^A in Eqs. (2.3) and (2.4) are defined by Eqs. (2.6) and (2.7), respectively, with their fitting coefficients (F_{ijk}^{A0} and F_{ijk}^{A1}) provided in Table 2 and Table 3:

$$F_0^A = \sum_{i=0}^{4} \sum_{j=0}^{4} \sum_{k=0}^{4} F_{ijk}^{A0} \left(\frac{r}{t}\right)^i \left(\frac{a}{t}\right)^j \left(\frac{a}{c}\right)^k \qquad (i + j + k \le 4), \tag{2.6}$$

$$F_1^A = \sum_{i=0}^{4} \sum_{j=0}^{4} \sum_{k=0}^{4} F_{ijk}^{A1} \left(\frac{r}{t}\right)^i \left(\frac{a}{t}\right)^j \left(\frac{a}{c}\right)^k \qquad (i + j + k \le 4). \tag{2.7}$$

Table 2. Fitting coefficients F_{ijk}^{A0}.

ijk	**000**	**100**	**010**	**001**	**200**	**110**	**020**	**101**
F_{ijk}^{A0}	0.80987	0.43996	0.31255	−0.33554	−0.53319	0.89868	1.0763	−0.32291
ijk	**011**	**002**	**300**	**210**	**120**	**030**	**201**	**111**
F_{ijk}^{A0}	−3.8205	2.3282	0.28616	−0.39388	0.42119	0	0.099301	−1.0692
ijk	**021**	**102**	**012**	**003**	**400**	**310**	**220**	**130**
F_{ijk}^{A0}	−2.1016	0.67762	6.1776	−3.6767	−0.054743	0.050831	0.058895	0.067399
ijk	**040**	**301**	**211**	**121**	**031**	**202**	**112**	**022**
F_{ijk}^{A0}	−1.5952	−0.010479	0.082393	−0.68089	3.4542	−0.062899	0.93604	−1.2303
ijk	**103**	**013**	**004**					
F_{ijk}^{A0}	−0.43519	−2.5408	1.7877					

Table 3. Fitting coefficients F_{ijk}^{A1}.

ijk	**000**	**100**	**010**	**001**	**200**	**110**	**020**	**101**
F_{ijk}^{A1}	0.26186	0.20553	0.25101	−0.20993	−0.23079	0.39053	0.81609	−0.21552
ijk	**011**	**002**	**300**	**210**	**120**	**030**	**201**	**111**
F_{ijk}^{A1}	−2.2418	1.2155	0.12163	−0.19866	0.4733	0	0.077674	−0.76695
ijk	**021**	**102**	**012**	**003**	**400**	**310**	**220**	**130**
F_{ijk}^{A1}	−1.7481	0.45305	3.9868	−2.1541	−0.022975	0.026659	0.010877	−0.020452
ijk	**040**	**301**	**211**	**121**	**031**	**202**	**112**	**022**
F_{ijk}^{A1}	−1.2667	−0.011164	0.068314	−0.4424	2.4765	−0.042608	0.62347	−0.7467
ijk	**103**	**013**	**004**					
F_{ijk}^{A1}	−0.29034	−1.6712	1.0968					

The key parameters (M_{1A}, M_{2A}, and M_{3A}) of the weight function at point A were determined by substituting the fitted reference SIFs into the weight function integration procedure and solving the inverse problem.

In (Zheng *et al.*, 1996), the weight function of point A is calculated as Eq. (2.8), and the corresponding weight function is expressed as Eq. (2.9):

$$K^A = \int_0^a \sigma(y) m_A(y,a)\,\mathrm{d}y, \tag{2.8}$$

$$m_A(y,a) = \frac{2}{\sqrt{2\pi(a-y)}}\left[1 + M_{1A}\left(1-\frac{y}{a}\right)^{1/2} + M_{2A}\left(1-\frac{y}{a}\right) + M_{3A}\left(1-\frac{y}{a}\right)^{3/2}\right]. \tag{2.9}$$

Synthesis of the aforementioned procedures with the solution methodology described in (Zheng *et al.*, 1996) yields the three key parameters (M_{1A}, M_{2A}, and M_{3A}) of the weight function at point A, as expressed in Eq (2.10):

$$\begin{aligned} M_{1A} &= \frac{\pi}{\sqrt{2Q}}(4F_0^A - 6F_1^A) - \frac{24}{5}, \\ M_{2A} &= 3, \\ M_{3A} &= 2\left(\frac{\pi}{\sqrt{2Q}}F_0^A - M_{1A} - 4\right). \end{aligned} \tag{2.10}$$

2.4. Weight functions for the plate-surface point (point B)

Similarly, the fitted reference SIFs at point B are given by Eqs. (2.11) and (2.12), corresponding to the uniformly distributed load and linearly distributed load cases, respectively:

$$K_{r1}^B = \sigma_0\sqrt{\frac{\pi a}{Q}}F_0^B, \tag{2.11}$$

$$K_{r2}^B = \sigma_0\sqrt{\frac{\pi a}{Q}}F_1^B, \tag{2.12}$$

where Q likewise represents an elliptic integral of the second kind, as given in Eq. (2.5).

The geometric correction factors F_0^B and F_1^B in Eqs. (2.11) and (2.12) are defined by Eqs. (2.13) and (2.14), respectively, with their fitting coefficients (F_{ijk}^{B0} and F_{ijk}^{B1}) provided in Table 4 and Table 5:

$$F_0^B = \sum_{i=0}^{4}\sum_{j=0}^{4}\sum_{k=0}^{4} F_{ijk}^{B0}\left(\frac{r}{t}\right)^i\left(\frac{a}{t}\right)^j\left(\frac{a}{c}\right)^k \qquad (i+j+k\le 4), \tag{2.13}$$

$$F_1^B = \sum_{i=0}^{4}\sum_{j=0}^{4}\sum_{k=0}^{4} F_{ijk}^{B1}\left(\frac{r}{t}\right)^i\left(\frac{a}{t}\right)^j\left(\frac{a}{c}\right)^k \qquad (i+j+k\le 4). \tag{2.14}$$

In (Zheng *et al.*, 1996), the weight function of point B is calculated as Eq. (2.15), and the corresponding weight function is expressed as Eq. (2.16):

$$K^B = \int_0^a \sigma(y) m_B(y,a)\,\mathrm{d}y, \tag{2.15}$$

$$m_B(y,a) = \frac{2}{\sqrt{\pi y}}\left[1 + M_{1B}\left(\frac{y}{a}\right)^{1/2} + M_{2B}\left(\frac{y}{a}\right) + M_{3B}\left(\frac{y}{a}\right)^{3/2}\right]. \tag{2.16}$$

Table 4. Fitting coefficients F_{ijk}^{B0}.

ijk	**000**	**100**	**010**	**001**	**200**	**110**	**020**	**101**
F_{ijk}^{B0}	0.18934	0.001833	−0.21587	2.2489	−0.035908	0.05961	1.2912	0.14708
ijk	**011**	**002**	**300**	**210**	**120**	**030**	**201**	**111**
F_{ijk}^{B0}	0.22558	−2.9939	0.033293	−0.12234	0.40337	0	−0.077422	0.018976
ijk	**021**	**102**	**012**	**003**	**400**	**310**	**220**	**130**
F_{ijk}^{B0}	−3.0223	−0.017841	1.5578	1.7403	−0.0080764	0.026938	−0.029182	0.057118
ijk	**040**	**301**	**211**	**121**	**031**	**202**	**112**	**022**
F_{ijk}^{B0}	0.92792	0.016252	−0.00075897	−0.33759	−3.0408	0.0049268	0.15513	5.0755
ijk	**103**	**013**	**004**					
F_{ijk}^{B0}	−0.032284	−2.8907	−0.018604					

Table 5. Fitting coefficients F_{ijk}^{B1}.

ijk	**000**	**100**	**010**	**001**	**200**	**110**	**020**	**101**
F_{ijk}^{B1}	0.19763	−0.00029338	−0.13599	1.8091	−0.020001	0.033383	0.87295	0.099138
ijk	**011**	**002**	**300**	**210**	**120**	**030**	**201**	**111**
F_{ijk}^{B1}	0.096081	−2.4811	0.018856	−0.076752	0.26425	0	−0.054186	0.019809
ijk	**021**	**102**	**012**	**003**	**400**	**310**	**220**	**130**
F_{ijk}^{B1}	−2.0522	−0.010023	1.1515	1.6063	−0.0046192	0.017855	−0.023746	0.05524
ijk	**040**	**301**	**211**	**121**	**031**	**202**	**112**	**022**
F_{ijk}^{B1}	0.70579	0.012017	−0.0030259	−0.23092	−2.1742	0.0018728	0.10586	3.5405
ijk	**103**	**013**	**004**					
F_{ijk}^{B1}	−0.02068	−2.0474	−0.15014					

Synthesis of the aforementioned procedures with the solution methodology described in (Zheng *et al.*, 1996) yields the three key parameters (M_{1B}, M_{2B}, and M_{3B}) of the weight function at point B, as expressed in Eq. (2.17):

$$\begin{aligned} M_{1B} &= \frac{\pi}{\sqrt{4Q}}(30F_1^B - 18F_0^B) - 8, \\ M_{2B} &= \frac{\pi}{\sqrt{4Q}}(60F_0^B - 90F_1^B) + 15, \\ M_{3B} &= -(1 + M_{1B} + M_{2B}). \end{aligned} \tag{2.17}$$

3. ML-augmented WFM

From the derivation process of the aforementioned universal WFM, it can be concluded that establishing an accurate mapping relationship between the geometric correction factors of reference SIFs and the geometric dimensions of the cracked body is crucial for developing the universal WFM. For the aforementioned corner crack at a hole, the mapping relationship between the geometric correction factors of reference SIFs and the geometric dimensions of the cracked body is given by

$$F = f\left(\frac{r}{t}, \frac{a}{t}, \frac{a}{c}\right), \tag{3.1}$$

where F is the geometric correction factor, characterizing the influence of the cracked body's geometric dimensions on the SIF, and a/c, a/t, and r/t represent the geometric dimensions

of the corner crack at a hole. A complex nonlinear mapping relationship exists between the geometric correction factor (F) and these geometric dimensions (a/c, a/t, and r/t). In previous studies, polynomial fitting and similar means were typically utilized to establish this mapping relationship.

In this study, the nonlinear mapping relationship within the aforementioned universal WFM is developed using a GPR model.

3.1. Process for establishing mapping relationships using GPR

The GPR model, also known as the Kriging model, is an interpolation method based on Gaussian processes governed by a priori covariance (Rasmussen, 2004; Rasmussen & Williams, 2005). It provides both the mean and standard deviation as outputs during prediction, thereby offering a probabilistic prediction framework. As a non-parametric model, it falls under the umbrella of supervised learning.

The GPR algorithm can be mathematically formulated as Eq. (3.2), where $m(x)$ and $k(x,x')$ denote the mean function and covariance function, respectively. This formulation signifies that the function f follows a Gaussian distribution characterized by the mean function m and covariance kernel k:

$$f \sim \mathrm{GP}(m(x), k(x, x')). \tag{3.2}$$

The GPR model was employed to approximate the nonlinear relationships. This approximation procedure is also referred to as training the GPR model. During model training, an iterative optimization scheme was implemented with the objective of minimizing the mean squared error (MSE), as illustrated in Fig. 3. The minimum MSE was achieved after 25 iterations, indicating the completion of the model training process. On the workstation (Processor: i5-13600KF (3.50 GHz), RAM: 32.0 GB), the time required for the aforementioned training process is 9.3385 seconds. Once the model is trained, its prediction speed approaches 18 000 observations per second.

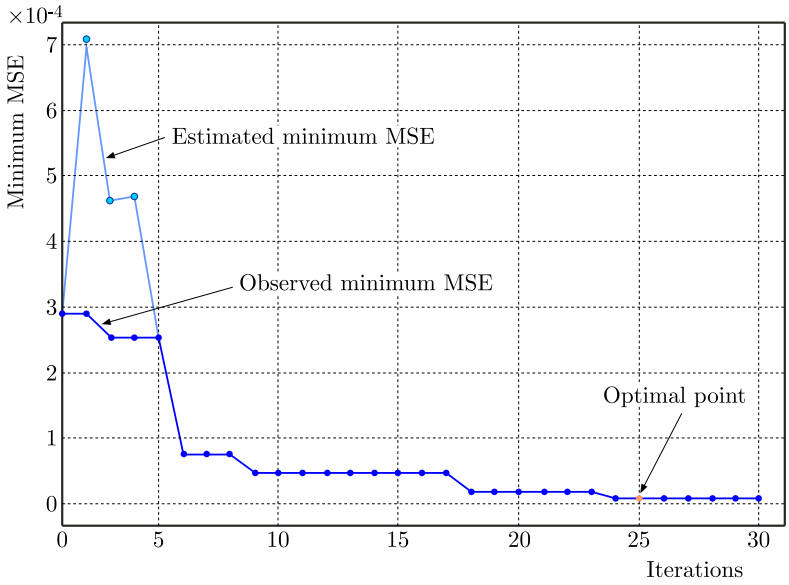

Fig. 3. Iterative training process for GPR model.

To demonstrate the effectiveness of the selected GPR model, a comparison of the prediction accuracy among various ML models was conducted. Specifically, different ML models, as shown in Table 6, were trained using the same training data, and their root mean square error (RMSE) values of the prediction results were compared, as illustrated in Fig. 4. It can be observed that the selected GPR model exhibits a smaller prediction RMSE and higher prediction accuracy.

Table 6. Details of the ML model.

ML model	Parameters of the ML model
Gaussian process regression (GPR)	Basis function: linear, $\sigma = 0.1019$
Support vector regression (SVR)	SVR with a cubic kernel
Artificial neural network (ANN)	Two-layer neural network, number of fully connected layers: 2, activation function: ReLU
Stepwise regression model (SRM)	Maximum number of steps: 1000
Regression tree (RT)	Coarse-grained tree, minimum leaf size: 36

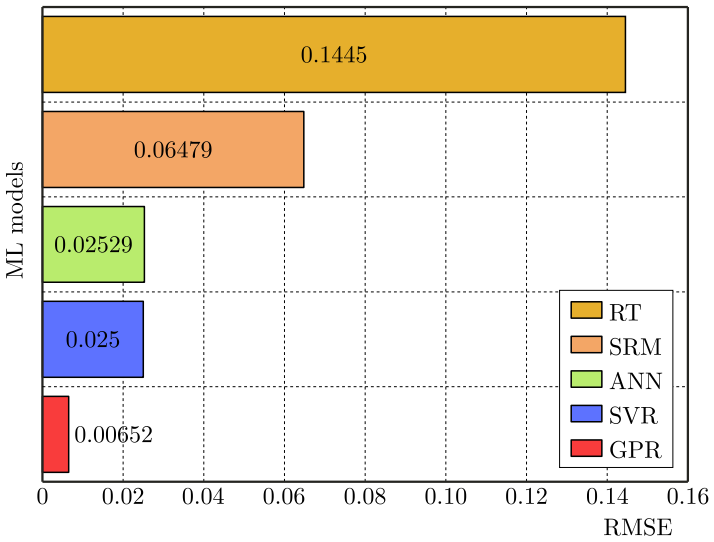

Fig. 4. Comparison of predictive accuracy among different ML models.

3.2. Nonlinear mapping relationship fitting results

The geometric correction factors at point A under the two types of reference loads are denoted as F_0^A and F_1^A. Nonlinear mapping relationships between these geometric correction factors and the geometric dimensions of the crack body were established using GPR models, as given in Eqs. (3.3) and (3.4). Since the fitted results of the GPR models cannot be represented by explicit analytical expressions, Eqs. (3.3) and (3.4) merely serve as representations of the relationships between the input variables and the output variables:

$$F_0^A = f_{0\,\mathrm{GPR}}^A\left(\frac{r}{t}, \frac{a}{t}, \frac{a}{c}\right), \tag{3.3}$$

$$F_1^A = f_{1\,\mathrm{GPR}}^A\left(\frac{r}{t}, \frac{a}{t}, \frac{a}{c}\right). \tag{3.4}$$

Concurrently, nonlinear mapping relationships between the geometric correction factors at point B (F_0^B and F_1^B) and the geometric dimensions of the crack body were established using GPR models, as represented by:

$$F_0^B = f_{0\,\mathrm{GPR}}^B\left(\frac{r}{t}, \frac{a}{t}, \frac{a}{c}\right), \tag{3.5}$$

$$F_1^B = f_{1\,\mathrm{GPR}}^B\left(\frac{r}{t}, \frac{a}{t}, \frac{a}{c}\right). \tag{3.6}$$

SHapley Additive exPlanations (SHAP) values quantify the contribution of each feature to the model output, and are thus widely employed in the field of ML to elucidate the relationship

between inputs and outputs. Figure 5 illustrates the SHAP values of different features (a/c, a/t, and r/t) with respect to the output of the GPR model. In the figure, a larger data width indicates a greater influence of the corresponding feature on the GPR model output. It can be observed that all three features exhibit a strong contribution to the output values.

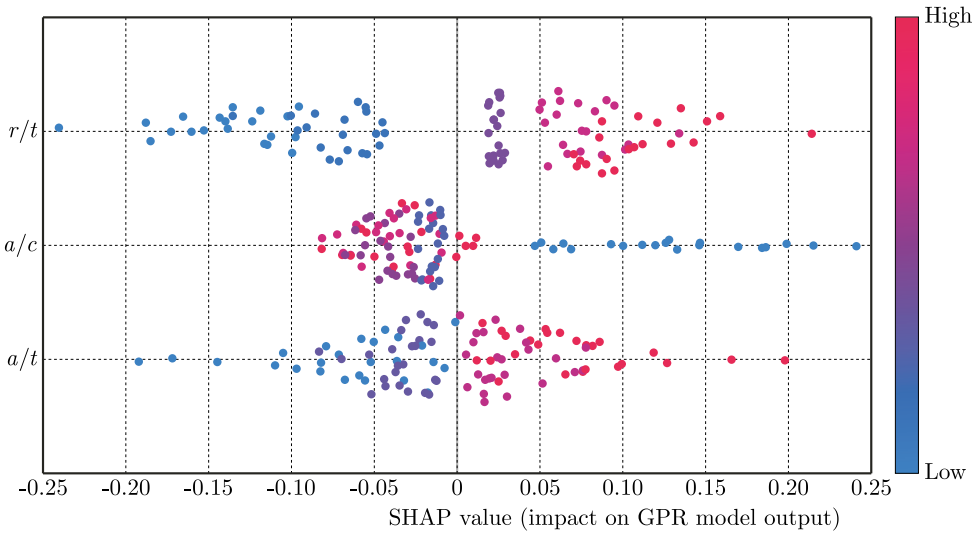

Fig. 5. SHAP values of different features to the GPR model output.

The GPR model predictions of the geometric correction factors at points A and B are presented in Fig. 6. The reference values shown in the figures correspond to the geometric correction

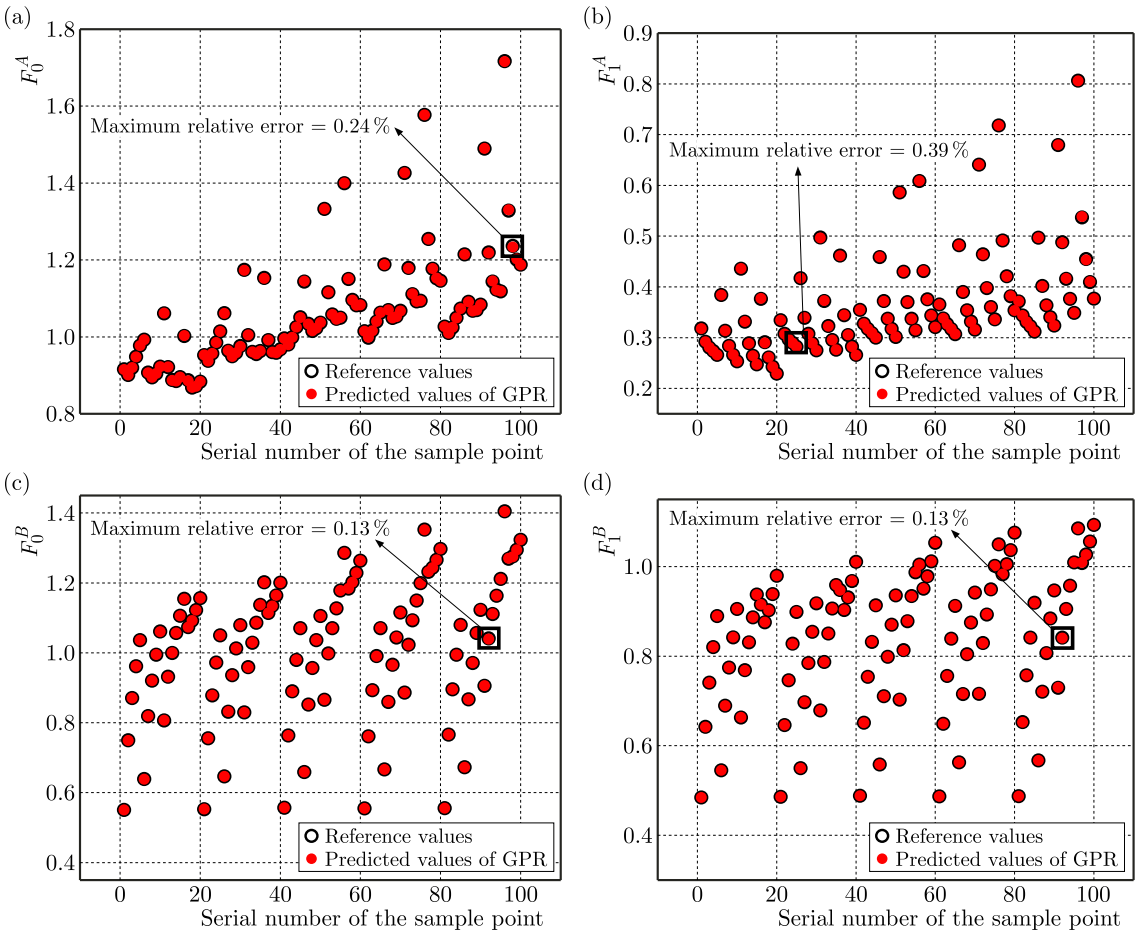

Fig. 6. GPR model prediction results for geometric correction factors: (a) F_0^A; (b) F_1^A; (c) F_0^B; (d) F_1^B.

factors calculated using finite element results for the SIFs. It can be observed that the GPR model, which fits the mapping relationship between the geometric correction factors and the crack body's geometric dimensions, achieves high prediction accuracy, with a maximum relative prediction error of 0.39 %. Upon completing the description of the nonlinear mapping relationships for the universal WFM, these mappings, combined with the universal weight function derived in Section 2, constitute the machine learning-augmented universal WFM.

4. Validation

This section assesses the computational accuracy of the proposed ML-augmented WFM. First, the SIFs for a corner crack at a hole under new stress distribution are computed using: (a) the FEM, (b) the conventional WFM detailed in Section 2, and (c) the proposed ML-augmented WFM. Subsequently, using the FEM results as the benchmark, the prediction accuracy of the other two methods (the conventional WFM and ML-augmented WFM) is compared. The stress distribution applied to the crack in this validation case is given by

$$\sigma(y) = \sigma_0 \left(1 - \frac{y}{a}\right)^n, \qquad n = 2, 3. \tag{4.1}$$

The computed SIFs are presented in Fig. 7 and Fig. 8. It can be observed that the proposed ML-augmented WFM demonstrates enhanced predictive accuracy over the conventional WFM.

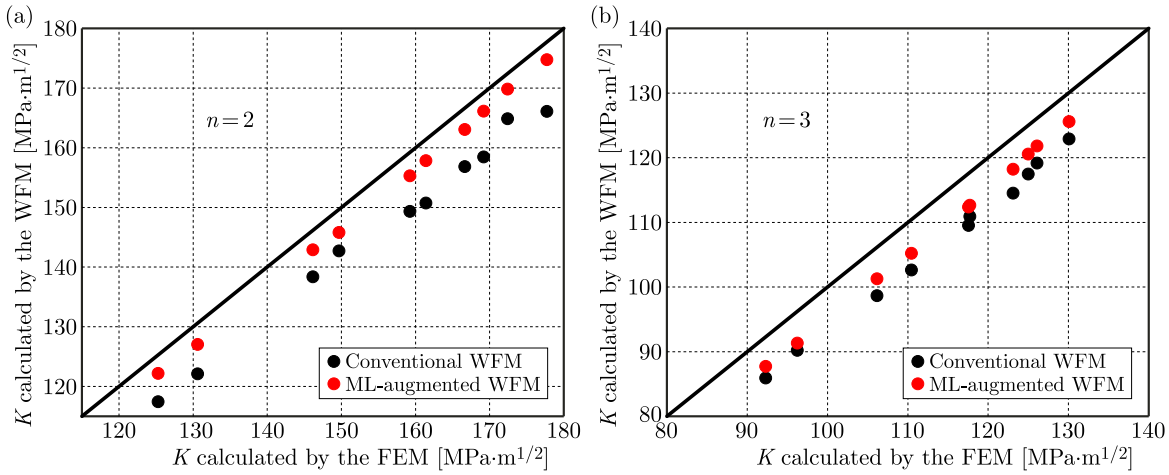

Fig. 7. Computed SIFs at point A: (a) $n = 2$; (b) $n = 3$.

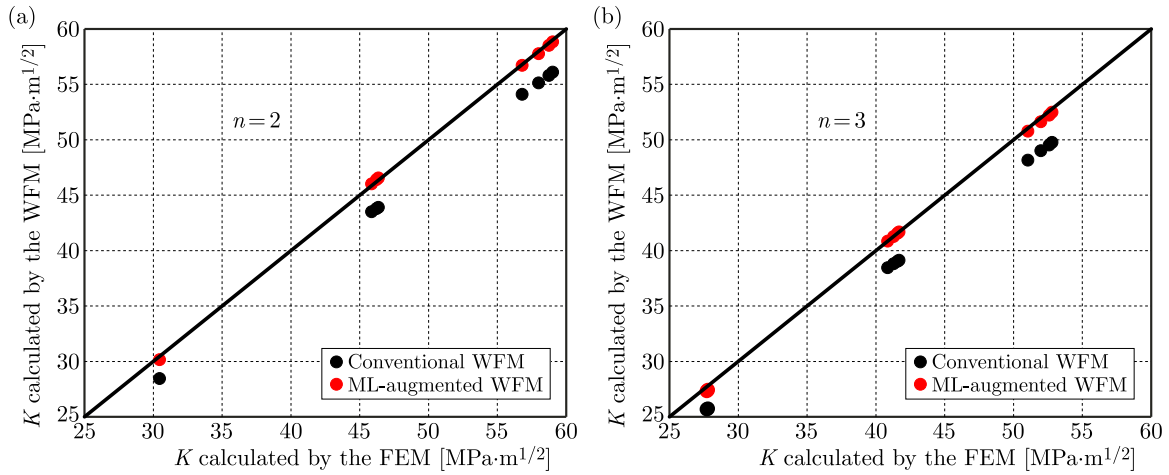

Fig. 8. Computed SIFs at point B: (a) $n = 2$; (b) $n = 3$.

Compared with the FEM results, the maximum relative error of the proposed method is merely 5.09 %.

5. Conclusion

Based on this study, three conclusions are drawn:

1) intricate nonlinear mapping relationships exist between the key parameters in the weight function and the crack geometric dimensions. The predictive accuracy of the universal WFM is limited by its inability to precisely characterize these nonlinear relationships. Therefore, advanced regression techniques are required to accurately describe the nonlinear relationships between the key parameters and the crack body's geometric dimensions, thereby enhancing the computational accuracy of the universal WFM;
2) an innovative machine learning-augmented WFM is proposed to improve the predictive accuracy of the universal WFM. This approach utilizes GPR models to fit the nonlinear mapping relationships between the key parameters in the weight function and the crack geometric dimensions;
3) validation cases demonstrate that the proposed machine learning-augmented WFM outperforms the conventional WFM in terms of predictive accuracy, with the maximum prediction error not exceeding 5.09 %.

Acknowledgments

This study was supported by the National Major Science and Technology Project (grant no. J2019-IV-0007-0075).

References

1. Chen, Q., & Wang, X. (2004). Weight functions and stress intensity factors for quarter-elliptical corner cracks in fastener holes. *Fatigue & Fracture of Engineering Materials and Structures*, *27*(8), 701–712. https://doi.org/10.1111/j.1460-2695.2004.00796.x

2. Evans, R., Clarke, A., Heller, M., & Stewart, R. (2014). Improved stress intensity factors for a single corner crack at a loaded fastener hole. *Engineering Fracture Mechanics*, *131*, 570–586. https://doi.org/10.1016/j.engfracmech.2014.09.012

3. Ghajar, R., & Saeidi Googarchin, H. (2013). General point load weight function for semi-elliptical crack in finite thickness plates. *Engineering Fracture Mechanics*, *109*, 33–44. https://doi.org/10.1016/j.engfracmech.2013.06.007

4. Glinka, G., & Shen, G. (1991). Universal features of weight functions for cracks in mode I. *Engineering Fracture Mechanics*, *40*(6), 1135–1146. https://doi.org/10.1016/0013-7944(91)90177-3

5. Guo, K., Liu, H., Yan, H., Song, Z., Zhang, S., Huang, D., & Yan, X. (2024). Estimation of stress intensity factor for surface cracks in the firtree groove structure of a turbine disk using pool-based active learning with Gaussian Process Regression. *Journal of Theoretical and Applied Mechanics*, *62*(1), 89–101. https://doi.org/10.15632/jtam-pl/174709

6. Keprate, A., Ratnayake, R.M.C., & Sankararaman, S. (2017). Comparison of various surrogate models to predict stress intensity factor of a crack propagating in offshore piping. *Journal of Offshore Mechanics and Arctic Engineering*, *139*(6), Article 061401. https://doi.org/10.1115/1.4037290

7. McClung, R.C., Lee, Y.-D., Cardinal, J.W., & Guo, Y. (2013). The pursuit of K: Reflections on the current state-of-the-art in stress intensity factor solutions for practical aerospace applications. In A. Brot (Ed.), *Proceedings of the 27th Symposium of the International Committee on Aeronautical Fatigue and Structural Integrity: Vol. 1* (pp. 361–375). Israel Society of Aeronautics and Astronautics.

8. Muñoz-Abella, B., Rubio, L., & Rubio, P. (2015). Stress intensity factor estimation for unbalanced rotating cracked shafts by artificial neural networks. *Fatigue & Fracture of Engineering Materials & Structures*, *38*(3), 352–367. https://doi.org/10.1111/ffe.12237

9. Newman Jr, J.C., & Raju, I.S. (1981). *Stress-intensity factor equations for cracks in three-dimensional finite bodies* (NASA Technical Memorandum 83200). National Aeronautics and Space Administration. https://ntrs.nasa.gov/api/citations/19810023035/downloads/19810023035.pdf

10. Newman Jr, J.C., & Raju, I.S. (1984). *Stress-intensity factor equations for cracks in three-dimensional finite bodies subjected to tension and bending loads* (NASA Technical Memorandum 85793). National Aeronautics and Space Administration. https://ntrs.nasa.gov/api/citations/19840015857/downloads/19840015857.pdf

11. Raju, I.S., & Newman Jr, J.C. (1979). Stress-intensity factors for a wide range of semi-elliptical surface cracks in finite-thickness plates. *Engineering Fracture Mechanics*, *11*(4), 817–829. https://doi.org/10.1016/0013-7944(79)90139-5

12. Rasmussen, C.E. (2004). Gaussian processes in machine learning. In O. Bousquet, U. von Luxburg, & G. Rätsch (Eds.), *Advanced Lectures on Machine Learning. ML 2003* (pp. 63–71). *Lecture Notes in Computer Science: Vol. 3176*. Springer. https://doi.org/10.1007/978-3-540-28650-9_4

13. Rasmussen, C.E., & Williams, C.K.I. (2005). *Gaussian Processes for Machine Learning*. The MIT Press.

14. Shen, G., & Glinka, G. (1991a). Determination of weight functions from reference stress intensity factors. *Theoretical and Applied Fracture Mechanics*, *15*(3), 237–245. https://doi.org/10.1016/0167-8442(91)90022-c

15. Shen, G., & Glinka, G. (1991b). Weight functions for a surface semi-elliptical crack in a finite thickness plate. *Theoretical and Applied Fracture Mechanics*, *15*(3), 247–255. https://doi.org/10.1016/0167-8442(91)90023-D

16. Shen, G., Plumtree, A., & Glinka, G. (1991). Weight function for the surface point of semi-elliptical surface crack in a finite thickness plate. *Engineering Fracture Mechanics*, *40*(1), 167–176. https://doi.org/10.1016/0013-7944(91)90136-O

17. Vainshtok, V.A., & Varfolomeyev, I.V. (1990). Stress intensity factor analysis for part-elliptical cracks in structures. *International Journal of Fracture*, *46*(1), 1–24. https://doi.org/10.1007/BF00034165

18. Wang, X., & Lambert, S.B. (1995a). Local weight functions for semi-elliptical surface cracks in finite thickness plates. *Theoretical & Applied Fracture Mechanics*, *23*(3), 199–208. https://doi.org/10.1016/0167-8442(95)00022-7

19. Wang, X., & Lambert, S.B. (1995b). Stress intensity factors for low aspect ratio semi-elliptical surface cracks in finite-thickness plates subjected to nonuniform stresses. *Engineering Fracture Mechanics*, *51*(4), 517–532. https://doi.org/10.1016/0013-7944(94)00311-5

20. Wawrzynek, P.A., Carter, B.J., Hwang, C.-Y., & Ingraffea, A.R. (2010). Advances in simulation of arbitrary 3D crack growth using FRANC3Dv5. *Journal of the Computational Structural Engineering Institute of Korea*, *23*(6), 607–613.

21. Xiao, X., & Yan, X. (2008). A numerical analysis for cracks emanating from a surface semi-spherical cavity in an infinite elastic body by FRANC3D. *Engineering Failure Analysis*, *15*(1–2), 188–192. https://doi.org/10.1016/j.engfailanal.2006.11.015

22. Yang, S.T., Ni, Y.L., & Li, C.Q. (2013). Weight function method to determine stress intensity factor for semi-elliptical crack with high aspect ratio in cylindrical vessels. *Engineering Fracture Mechanics*, *109*, 138–149. https://doi.org/10.1016/j.engfracmech.2013.05.014

23. Zheng, X.J., Glinka, G., & Dubey, R.N. (1996). Stress intensity factors and weight functions for a corner crack in a finite thickness plate. *Engineering Fracture Mechanics*, *54*(1), 49–61. https://doi.org/10.1016/0013-7944(95)00171-9

Manuscript received August 2, 2025; accepted for publication January 15, 2026; published online March 10, 2026.

Contents

Kita M., Kaczmarczyk J., Duda S., *Influence of air vent geometry in brake rotors on the performance of a car braking system* 3

Ma Y., Zou Z., Chen J., Shen R., *Vibration fatigue behaviour analysis of the cracked plate under a uniform temperature field* 15

Jiang S., Chen Q., *Research on adaptive fuzzy sliding mode control with switching strategy for trajectory tracking of digital hydraulic cylinder* 29

Eka Setyawan P., Purnowidodo A., As'ad Sonief A., Surya Irawan Y., *Evaluation of viscosity and rheological characteristics of corn oil combined with graphene nanoplatelets for machining lubrication* 45

Su H., Song F., Sun C., Zhang J., *Physics-informed neural networks for inhomogeneous swelling analysis of dual-layer gels with chain entanglement effects* 57

Yin J., Wu Y., Hao Y., Xue K., Zhang Y., Zhang H., *Study on roof fracture mechanism and mine pressure characteristics in pseudo-inclined working faces of steeply inclined coal seams* 71

Guo K., Tang W., Yang Z., Wang C., Sun T., *Machine learning-augmented universal weight function method for stress intensity factor determination* 85